Die approbierte Originalversion dieser Diplom-/Masterarbeit ist an der Hauptbibliothek der Technischen Universität Wien aufgestellt (http://www.ub.tuwien.ac.at).

The approved original version of this diploma or master thesis is available at the main library of the Vienna University of Technology (http://www.ub.tuwien.ac.at/englweb/).

TECHNISCHE UNIVERSITÄT WIEN
Vienna University of Technology

D I P L O M A R B E I T

Localization of Trace Elements in Bone Tissue using Synchrotron Radiation Induced Micro-XRF in Combination with Quantitative Backscattered Electron Imaging

ausgeführt am

Atominstitut
der Technischen Universität Wien

unter Anleitung von

Ao.Univ.Prof.Dipl.Ing.Dr. Christina Streli

durch

Andreas Roschger

Erlgasse 40
A-1120 Wien

Wien, 16. März 2011

Kurzfassung

Die Verwendung von Synchrotronstrahlung induzierter mikro-Röntgenfluoreszenanalyse (SR-micro-XRF) stellte sich als eine Methode heraus, die hervorragend zur ortsaufgelösten, zerstörungsfreien Multielement-Untersuchung von Knochen und Gelenksknorpel geeignet ist. Ergänzend kann quantitative Rückstreuelektronenmikroskopie (qBEI) genaue Informationen über den Grad der Mineralisierung liefern und ermöglicht es zwischen verschiedenen histologischen Regionen zu unterscheiden.

In Rahmen dieser Arbeit wurden mikro-XRF und qBEI kombiniert, um die Verteilung der Spurenelemente Blei (Pb), Zink (Zn) und Strontium (Sr) in Knochen und Gelenkknorpel zu charakterisieren. Diese Kombination erlaubt es die verschiedenen histologischen Regionen (ausgewählt anhand des qBEI Bildes) den Fluoreszenzmaps zuzuordnen. So können zum ersten Mal die 2-dimensionale Verteilung von Spurenelementen sowie die relativen Konzentrationen in Knochen und Knorpel untersucht werden. Die FLUO Beamline des ANKA-Synchrotrons (KIT, Karlsruhe, Deutschland) sowie die Beamline L des DORIS III Synchrotrons (HASYLAB, Hamburg, Deutschland) wurden hierfür verwendet. Ein konfokaler Versuchsaufbau erlaubte eine räumliche Auflösung von ca. $10 \times 15 \times 20\ \mu m$. Die Primärstrahlenergie von etwa 17 keV sorgte für optimale Pb Anregung. Für die qBEI Messungen wurde ein Rasterelektronenmikroskop (Zeiss DSM 962, Oberkochen, Deutschland) mit 20 kV Beschleunigungsspannung und 110 Pa Sondenstrom verwendet. Die Auflösung betrug hier 1 μm.

Es ist bekannt, dass langzeitige Pb-Exposition mit chronischen Erkrankungen des zentralen Nervensystems sowie mit einer Schädigung des Nieren- Hormon- und hämatopoetischen Systems in Verbindung steht. Darüber hinaus ist eine erhöhte Bleiaufnahme ein bekannter Risikofaktor für Osteoporose. Etwa 95% der gesamten Bleimenge des menschlichen Körper sind im Skelett gespeichert und haben dort eine biologische Halbwertszeit von rund 20 Jahren.
Zn ist ein essentielles Spurenelement, weit verbreitet in den reaktiven Zentren von Enzymen. Weiters ist bekannt, dass Zn die Zellproliferation von knochenbildenden Zellen (Osteoblasten) fördert.
Die Bedeutung von Sr wuchs in den letzten Jahren, aufgrund der Verwendung von Strontiumranelat in Osteoporose-Behandlung.

In 6 Hüftköpfen und 3 Kniescheiben wurden die Tidemarks untersucht (die TM ist die Grenzfläche zwischen mineralisiertem und nicht mineralisiertem Gelenksknorpel). Eine

Verdoppelung der TM steht vermutlich in Zusammenhang mit äußeren mechanischen Reizen. Sowohl doppelte als auch einzelne TMs wurden auf die Spurenelementverteilung hin untersucht. Um weiters die Verteilung im Knochen zu erforschen wurden 5 frakturierte Oberschenkelhälse von osteoporotischen postmenopausalen Frauen, sowie 5 unfrakturierte Oberschenkelhälse von einer Kontrollgruppe gemessen. Zusätzlich wurde die Spurenelementverteilung in einem mit Cisplatin behandelten, sklerosierenden Osteosarcom (Knochentumor) ermittelt.

Die Hauptergebnisse dieser Untersuchungen sind:

1. In Regionen mit doppelten TMs sind die Zn-Konzentrationen beiden TMs annähernd gleich.

2. Die Analyse der relativen Pb-konzentrationen in doppelten TMs zeigt durchschnittlich eine 2.6-fache Erhöhung des Pb Gehaltes in der inneren TM verglichen mit der äußeren, während das Pb Verhältnis zwischen den TMs stark schwankt (von dem 1.4-fachen bis zu dem 3.9-fachen).

3. Relativ zu den Elementkonzentrationen im darunterliegendem Knochengewebe ist der Zn und der Pb Gehalt in den TMs drastisch erhöht (bis zu 58-fach für Pb und bis zu 7-fach für Zn). Einfache TMs zeigen Konzentrationen vergleichbar mit der inneren TM von doppel-TM Regionen.

4. In den Oberschenkelhalsproben konnte kein Unterschied in der Elementverteilung zwischen osteoporotischem Knochen und den nichtfrakturierten Proben der Kontrollgruppe festgestellt werden.

5. In nahezu allen Proben zeigen die Zementlinien (Grenzflächen zwischen 2 Knochenpaketen) signifikant erhöhte Zn und Pb Werte, verglichen mit den Knochenpaketen. Weiters ist auffällig, dass Knochenränder und Ränder von Osteonen oft hohe Zn Konzentrationen aufweisen.

6. Ein überproportional starker Anstieg der Pb-Konzentration bezüglich des Ca-Gehaltes wurde in den Knochenpaketen beobachtet.

7. Das sklerosierende Osteosarcom zeigte eine 13-fach erhöhte Zn Konzentration bezogen auf das umliegende gesunde Knochengewebe. Es wurde kein Platin in dieser Probe gefunden.

Abstract

Synchrotron radiation induced micro X-ray fluorescence analysis (SR-micro-XRF) is a suitable method for spatial resolved, non-destructive, multi-element examination of bone and articular cartilage. Quantitative backscatter electron imaging (qBEI) accounts for information of the degree of mineralization and allows distinguishing between histological regions. In this thesis micro-XRF and qBEI were used for a combined data evaluation of the trace elements lead (Pb), zinc (Zn) and strontium (Sr) in bone and articular cartilage. This combination allows allocating the histological regions (labeled in the qBEI image) to elemental fluorescence maps. Hence, for the first time, the spatial distribution and the relative concentrations of trace elements in bone and cartilage were evaluated. The FLUO beamline of the ANKA synchrotron (KIT, Karlsruhe, Germany) as well as the beamline L of the DORIS III synchrotron (HASYLAB, Hamburg) were used for trace element analysis of bone tissue and mineralized articular cartilage. A confocal setup provides a spatial resolution of approximately $10 \times 15 \times 20 \mu m$. The primary beam energy of about 17 keV account for optimal Pb excitation.
An scanning electron microscope (Zeiss DSM 962, Oberkochen, Germany) with 20 kV acceleration voltage and 110 pA probe current was used to perform qBEI, providing a resolution of about 1 μm

Long-term exposure of Pb is associated with chronic diseases of the central nervous, the skeletal-hematopoietic, the renal and the endocrine systems. Furthermore, lead incorporation is a risk factor for osteoporosis. Approximately 95% of the total burden of Pb is stored in the skeleton with a typical half-life of 20 years.
Zn is an essential trace element, widespread in the reactive center of various enzymes and is also known to facilitate proliferation of human bone forming cells (osteoblasts).
The importance of Sr in humans rose during the last years, due to the use of Sr-ranelate in osteoporosis treatment.

In 3 patellae and 6 hip heads the tidemarks (the TM is the interface between mineralized and non-mineralized articular cartilage) were analyzed. Double TMs (TM duplication is assumed to be a response to micro damage) as well as single TMs were measured. From 5 femoral necks of osteoporotic postmenopausal women with hip fractures, as well as from 5 age-matched controls without a history of bone disease, information of the elemental distribution was gained. Furthermore, the evaluation of the elemental distribution of a cisplatin treated, sclerosing osteosarcoma was performed.

The main results of these studies are:

1. The analysis of the double TMs showed that the Zn concentration is nearly equal in both TMs.

2. The evaluation of Pb intensities in double TMs revealed in average a 2.6 fold higher level in the inner TM compared to the outer TM, whereby the Pb in the outer TM showed a high variation with respect to the inner TM (1.4 to 3.9 fold).

3. Compared to the bone level, the Pb and Zn content is drastically increased (up to the 58 fold for Pb and 7 fold for Zn). Single TMs show an elemental distribution comparable to the inner tidemark of double tidemark samples.

4. In the femoral neck samples no alterations in the distributions of Sr, Pb and Zn were found for osteoporotic bone compared to non-fractured controls.

5. The cementlines (interfaces between two bone packets) show a significantly raised content of Zn and Pb in nearly all samples. The bone borders and osteons borders are also often enhanced in Zn.

6. A disproportionate increase of Pb and Sr with respect to the bone packet concentration is observed.

7. The sclerosing osteosarcoma showed a 13 fold raised Zn concentration compared to the adjacent healthy bone tissue. No Platinum was found in this sample.

Acknowledgements

This thesis would not have been possible some without the help of certain persons. I would like to thank everyone who supported me during the last year:

Ao.Univ.Prof.Dipl.Ing.Dr. Christina Streli for great supervision and pleasing working atmosphere in the XRF team.

Univ.Prof.Dipl.Ing.Dr. Paul Roschger for advices in physical and biological question as well as for support and discussion of the data.

Dipl.Ing. Bernhard Pemmer for the assistance in physical and technical questions and for his helpfulness.

Dr. Jochen Hofstätter for his medical and biological input and for providing us samples.

Gerda Dinst, Daniela Gabriel, Sonja Lueger,
Phaedra Messmer (MSc) and Sabrina Thon for sample preparation and qBEI measurements.

Dr. Rolf Simon for beamline support at the ANKA synchrotron.

the whole team of the ***Ludwig Boltzmann Institute of Osteologie*** for intense cooperation, and for a convenient and productive working atmosphere.

the ***proofreaders*** of this thesis.

My special thanks are addressed to my ***family*** for facilliating the study and for support and encouragement in the last years.

Contents

1 Introduction **1**

2 X-Rays **2**
2.1 The Bohr model of atoms . . . 3
2.2 Properties of the X-ray spectrum . . . 5
2.2.1 Origin of the bremsstrahlung . . . 6
2.2.2 Origin of the characteristic radiation . . . 7
2.3 Interaction of photons with matter . . . 8
2.3.1 Photo effect . . . 9
2.3.2 Coherent scattering . . . 11
2.3.3 Incoherent scattering . . . 12
2.3.4 Pair production . . . 12
2.4 Attenuation coefficient and information depth . . . 13
2.5 Characteristics of X-ray-fluorescence analysis . . . 18
2.5.1 Fundamental parameters and quantitative analysis . . . 18
2.6 X-ray techniques . . . 21
2.6.1 X-ray sources . . . 22
2.6.2 Semiconductor detectors . . . 29
2.6.3 X-ray optics . . . 32

3 Physical Background of qBEI **38**
3.1 Principle of a scanning electron microscope (SEM) . . . 38
3.2 Interaction of electrons with matter . . . 39
3.2.1 Elastic scattering (backscattered electrons) . . . 41
3.2.2 Inelastic scattering (secondary electrons) . . . 45
3.2.3 Occurrence of X-rays . . . 50
3.3 Electrons in electrostatic and magnetostatic fields . . . 52
3.4 Electron guns . . . 53
3.5 Electron lenses . . . 55
3.6 Electron detectors . . . 56
3.6.1 Everhart - Thornley (E-T) detectors . . . 57
3.6.2 Scintillator backscatter electron detectors . . . 57
3.6.3 BE-to-SE conversion detectors . . . 58
3.6.4 Solid state diode detectors . . . 59

4 Characteristics of Bone and Cartilage **60**
4.1 Hierarchical structure and architecture 60
4.2 Mechanism of bone turnover 62
4.3 Characteristics of articular cartilage 65
4.4 Trace elements in bone and cartilage 66

5 Samples and Sample Preparation **68**
5.1 Measured samples 68
5.1.1 Samples for examination of the tidemark 69
5.1.2 Femoral neck samples for trace element analysis in bone 70
5.1.3 Osteosarcoma 71
5.2 Sample preparation 72

6 Experimental Setup and Analysis **73**
6.1 Synchrotron setup 73
6.2 Scanning electron microscope conditions 75
6.3 Data analysis 76
6.3.1 Spectrum processing 76
6.3.2 Data analysis with ImageJ 77

7 Results **81**
7.1 Trace elements in cartilage and subchrondral bone 81
7.1.1 Evaluation of regions with double tidemarks 81
7.1.2 Evaluation of regions with single tidemarks 86
7.2 Localization of trace elements in femoral necks 88
7.3 Zn distribution in an ostesarcoma 102

8 Discussion & Conclusion **104**

Bibliography **107**

Chapter 1

Introduction

Synchrotron radiation induced micro X-ray fluorescence analysis (SR-micro-XRF) is a well established and powerful method for multi-element analysis of a broad bandwidth of materials, especially for biological tissue. The microfocus setup at a synchrotron beamline allows scanning the sample point after point to get elemental maps with a sufficient spatial resolution to distinguish between various regions of interest in the tissue. This method was used to determine the localization of the trace elements lead (Pb), zinc (Zn) and strontium (Sr) in human bone and cartilage. It is combined with a scanning backscattered electron microscope, featuring a resolution more than 10 times higher than the fluorescence maps. This offers the possibility to differentiate between the histological structures in bone and cartilage and to link these regions with the micro-XRF elemental maps.

Nowadays much is known about the concentrations of above mentioned trace elements and Calcium (Ca) (which contributes for about 20% of the bone matrix). But the exact localization of Pb, Zn and Sr is still widely unknown and thus also their role in bone metabolism.
The aim of this thesis is to determine in which regions of bone and cartilage these elements are present and to use these findings for a better understanding of bone turnover. Especially mechanisms in the tidemark - the region between calcified and non calcified cartilage - as well as in bone forming sites are still widely unknown. We assume that the mechanisms of trace element deposition and accumulation helps to understand the dynamics in these regions of basic interest.
But there is also clinical relevance, especially for lead concentration and its localization in bone. Due to its high toxicity lead has the ability to cause damage in the central nervous system, the renal system, the cardiovascular system, the reproductive system and last but not least in the calcified tissue. Previous studies identified lead exposure as a risk factor for osteoporosis [1] [2]. The biological half life time of lead in the human body is about 20 years and about 95% of this element are deposited in mineralized tissue. It is assumed that a raised bone turnover leads to a release of the bone-stored lead and thus to an increased lead level in more sensitive organs [3].

In detail, we examined bone samples from the femoral neck, samples with chondral and subchondral bone from the patella and from hip heads, and one osteosarcom (bone tumor).

Chapter 2

X-Rays

X-rays were discovered at the end of the 19th century by Wilhelm Conrad Röntgen. During experimentation with a discharge tube, he observed luminescent barium-platinocyanide crystals while the tube was running. Due to the fact that the tube was enclosed with black paper and separated from the crystals, he proposed a new kind of radiation causing the glow of the crystals, called X-rays. For this finding Röntgen received the first Nobel Prize in physics in 1901.
Further research caused a dispute whether X-rays are waves or corpuscular because scatter- and ionization experiments lead to controversial results. Today we know that X-rays are part of the electromagnetic spectrum, such as visible light or radio waves. The energy E of X-rays reaches from 0.1 keV up to more than 100 keV. According to

$$E = h\nu = \frac{h \cdot c_0}{\lambda} \qquad and \qquad c_0 = \nu \cdot \lambda \tag{2.1}$$

the energy E of an electromagnetic wave is linked with its wavelength λ and the frequency ν. h stands for the Planck constant and c_0 vor the velocity of light in the vacuum. With common units Formula 2.1 can be written as

$$\text{E [keV]} = \frac{1.239}{\lambda \text{ [nm]}} \quad . \tag{2.2}$$

Roughly the X-ray spectrum can be dissected into three regions. [4]

- Soft X-rays: $E \approx 0.1$ - 1 keV [$\lambda = 10$ nm - 1 nm]
- Classical X-rays: $E \approx 1$ - 60 keV [$\lambda = 1$ nm - 0.002 nm]
- Hard X-rays: energy $>$ 60 keV [$\lambda < 0.002$ nm]

2.1 The Bohr model of atoms

The Bohr model describes electrons as particles moving around a positively charged atom nucleus on well defined shells. The radius r of the electron path is determined by the quantification condition of the angular momentum L. L is a function of the electron mass m_e and the angular velocity v.

$$L = r \times p = m_e \cdot r \cdot v \cdot n = n \cdot \hbar \qquad with \qquad \hbar = \frac{h}{2\pi} \tag{2.3}$$

Such an orbit is a possible electron path with well-defined energy determined by the main quantum number n. For hydrogen-like elements the wavelength λ of the emitted photon can be derived from the Rydberg formula with the atomic number Z and the Rydberg constant R.

$$\frac{1}{\lambda_{vac}} = RZ^2(\frac{1}{n_1^2} - \frac{1}{n_2^2}) \tag{2.4}$$

The transition from an orbit to another one with a lower n leads to the emission of a photon with the energy difference of the two orbits. Depending on the involved energy levels (more exactly the two main quantum numbers of the involved orbits) and the atomic number of the element, the released photon energy reaches from 50 eV up to 120 keV.

$$\Delta E = |E_{(i)} - E_{(f)}| = h\nu \tag{2.5}$$

ΔE describes the energy release caused of the transition from the initial state (i) to the final state (f). Induced by inner shell ionization these equations lead to an energy pattern, which is unique for every element. Later it will be shown that the well-defined energies of the emitted radiation can be used to identify elements und further to determine relative element variations in an unknown specimen.

As shown in Table 2.1 the inner shell (energy-richest-state) is called K-shell. The energy levels are successively named L, M, N, ... shells. If an electron transition occurs, it is named after the shell of the final state. So all transitions ending on the K-shell are summarized as the K-series. Depending on the initial state the transition is called K_α, K_β, ... and so on with decreasing transition intensity. The L, M, N, ... series are denoted similarly.
Due to quantum mechanic effects an energy level with the main quantum number n dissects into $2n-1$ subshells with slightly different energies. This complicates the nomenclature. Corresponding to the final state, the shells and the subshells, are named $K_{\alpha 1}$, $K_{\alpha 2}$, $K_{\beta 1}$, $K_{\beta 2}$, ...

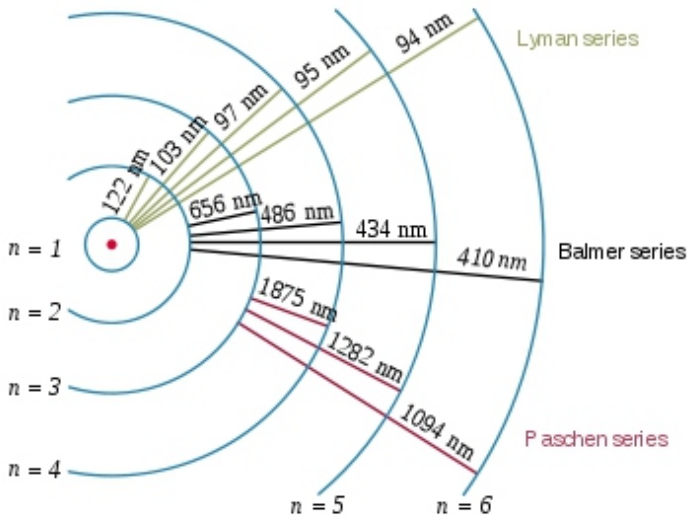

Figure 2.1: Electron transitions and their resulting wavelengths for hydrogen. Energy levels are not true to scale. [5]

The $2n+1$ splitting of the main energy levels is clarified in the following table which gives an overview of the quantum numbers. The Pauli law does not allow the simultanously presence of two electrons with equal quantum numbers in the same shell. A shell with the main quantum number n can be occupied with electrons carrying the orbital angular momentum l which goes from 0 to $n-1$; m_l, the magnetic quantum number varies from $-l$ to $+l$. Another quantum number is the electron spin s with the values $\pm\frac{1}{2}$.The total angular momentum j merges the spin s and the angular momentum l. It is characterized by the triangle inequality:

$$\left||\vec{l}| - |\vec{s}|\right| \leq |\vec{j}| \leq |\vec{l}| + |\vec{s}| \tag{2.6}$$

Table 2.1 gives a summary of the first four energy shells and the associated quantum numbers of a single electron system. Note the total number of $2n^2$ electrons per shell and the separation of $2n-1$ subshells with slightly differing energy.
In our experimental setup, the energy resolution of the X-ray detectors is below the energy gaps among the subshells. So it is sufficient to concentrate on the energy levels determined by the main quantum number.

energy shell		K	L			M				
subshell			L_I	L_{II}	L_{III}	M_I	M_{II}	M_{III}	M_{IV}	M_V
main quantum number	n	1	2	2	2	3	3	3	3	3
anguar momentum	l	0	0	1	1	0	1	1	2	2
total angular momentum	j	$\frac{1}{2}$	$\frac{1}{2}$	$\frac{1}{2}$	$\frac{3}{2}$	$\frac{1}{2}$	$\frac{1}{2}$	$\frac{3}{2}$	$\frac{3}{2}$	$\frac{5}{2}$
number of elecrons		2	2	2	4	2	2	4	4	4
total number of electrons		2	8			18				

energy shell		N						
subshell		N_I	N_{II}	N_{III}	N_{IV}	N_V	N_{VI}	N_{VII}
main quantum number	n	4	4	4	4	4	4	4
angular momentum	l	0	1	1	2	2	3	3
total angular momentum	j	$\frac{1}{2}$	$\frac{1}{2}$	$\frac{3}{2}$	$\frac{3}{2}$	$\frac{5}{2}$	$\frac{5}{2}$	$\frac{7}{2}$
number of electrons		2	2	4	4	6	6	8
total number of electrons		32						

Table 2.1: Energy shells of a hydrogen atom [6]

2.2 Properties of the X-ray spectrum

The sum of the photon-energies normalized by the illuminated area and the observation time gives the beam-intensity.

$$\mathrm{I}\left[\frac{\mathrm{W}}{\mathrm{cm}^2}\right] = \frac{\text{radiation energy [J]}}{\text{area [cm}^2\text{]} \cdot \text{time [s]}} \tag{2.7}$$

A plot with the intensity I on the y-axis and energy E, frequency ν or wavelength λ on the x-axis is called spectrum. E, ν and λ are linked by the Formulas 2.1 and thus the different spectrum types provide for similar information.

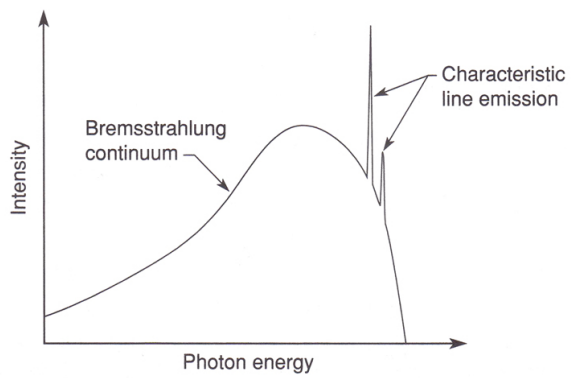

Figure 2.2: Typical X-ray spectrum consisting of the continuous bremsstrahlung superposed by sharp characteristic lines. [7]

Figure 2.2 shows an X-ray spectrum. It consists of a continuous component with relatively low intensity and a broad maximum (called bremsstrahlung) and of sharp particularly high

intense peaks resulting from characteristic radiation.
The origins of these two components are fundamentally different and will be discussed in the following chapters.

2.2.1 Origin of the bremsstrahlung

A consequence of the fundamental Maxwell equations is the energy loss of accelerated charged particles by emitting electromagnetic radiation. In Chapter 2.3.1 we will see that X-rays lead to a release of bonded electrons and thus to free charged particles with high energy in the specimen. As a matter of fact these electrons are scattered inelastically when passing a nucleus with the charge $+Z$ resulting in acceleration and further in emission of radiation with the energy E_{Ph} (Figure 2.3).$E_{kin}^{(i)}$ and $E_{kin}^{(f)}$ are the electron energies before and after scattering.

$$E_{ph} = h\nu = E_{kin}^{(i)} - E_{kin}^{(f)} \tag{2.8}$$

E_{ph} is determined by the charge of the nucleus Z, the initial energy of the electron and the approach parameter b. The last one describes the smallest distance between electron and nucleus.

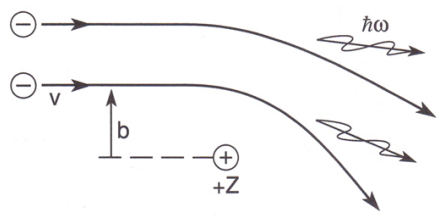

Figure 2.3: Bremsstrahlung occurs when electrons pass a nucleus. The energy $\hbar\omega$ of the emitted radiation is linked to the change in velocity and thus to the approach parameter b. [7]

As long as the scattered electron is described as a free state its energy is not quantized. Due to the large number of free electrons produced by the X-ray photons and the wide-ranging continuous variation of the approach parameter, the bremsstrahlung continuum is produced. As shown in Figure 2.2 its intensity depends on the energy and thus on the frequency ν. The spectral distribution of the intensity can be described by Formula 2.9. In the Formulas 2.9 and 2.10 ν_{max} stands for ν with maximum energy and equals the frequency of the unscattered electrons.

$$I(\nu) = Const \cdot (Z \cdot (\nu_{max} - \nu) + bZ^2) \tag{2.9}$$

The total intensity can be calculated by integration over the whole spectal distribution.

$$I_{ges} = \int_0^{\nu_{max}} I(\nu) \cdot d\nu \tag{2.10}$$

2.2.2 Origin of the characteristic radiation

As a result of the Bohr model of atoms (Chapter 2.1) the possible electron paths are limited to well defined shells around the nucleus. Electron transitions within the shells lead to energy absorption $E_{(i)} < E_{(f)}$ or to the release of a photon if $E_{(i)} > E_{(f)}$. A photon with adequate energy is able to ionize the atom by punching an inner-shell-electron out of the region of the attractive electrical force of the nucleus. This effect is called the photoelectric effect. Consequently a transition from an energy level with higher quantum number down to the shell with the electron leak occurs. Electrons successively change their shells to reach states with minimal potential energies. According to Formula 2.8 every transition to a lower energy level corresponds to a well defined energy release. This can cause the emission of fluorescence photons carrying released energy, defined by its frequency $E = h\nu$. If these fluorescence photons escape the specimen, they are measured as sharp peaks with a certain spectral distribution. In our case the characteristic radiation (sharp peaks in Figure 2.2) is used to examine the elemental composition of the specimen and to derive the relative concentrations according to the intensity of the fluorescence signal. A scheme of the copper energy levels is shown in Figure 2.4.

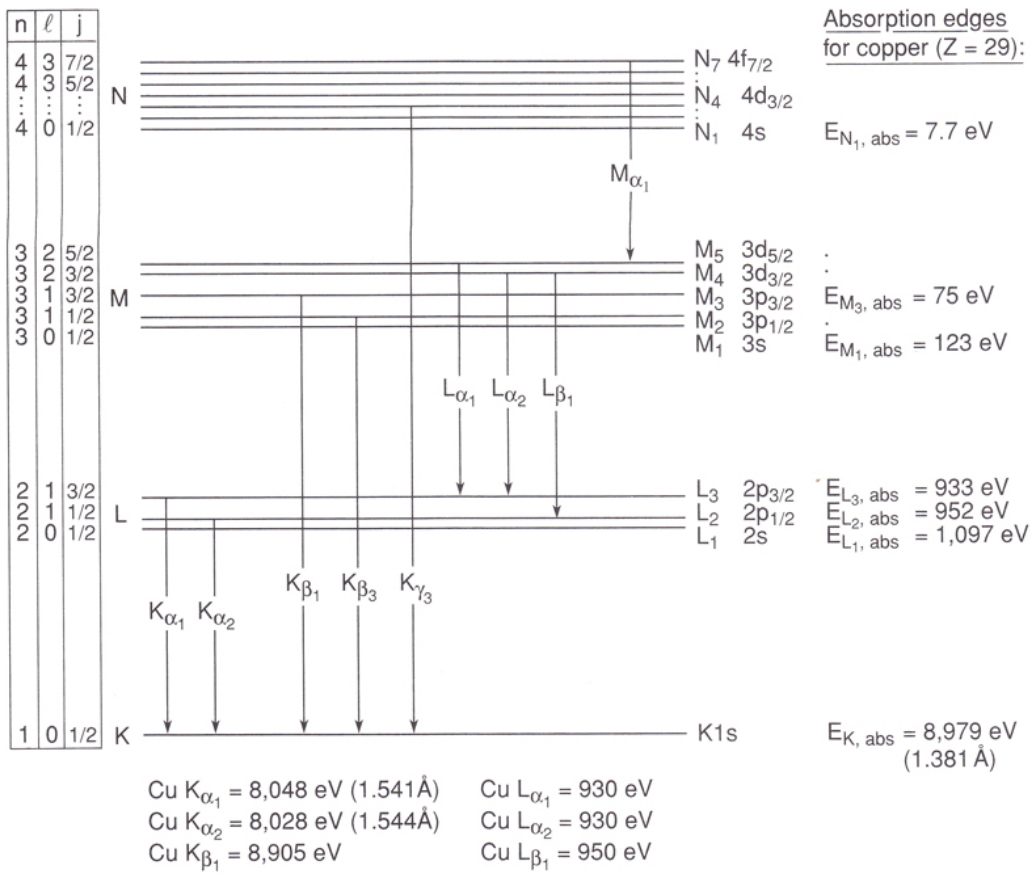

Figure 2.4: Scheme of possible electron transitions in a copper atom, illustrating the $2n + 1$ splitting of the energy shells and the consequences of the selection rules for dipole transitions. [7]

The origin of the $2n+1$ splitting is described in Chapter 2.1. As already mentioned, with conventional methods the small energy gaps within a shell cannot be resolved. To understand the origin of various fluorescent peak intensities, the number of possible transitions, and the transition probabilities have to be taken into account. So it is worth to take a closer look at the rules of transition. Dipole transitions are the dominant processes when an electron interacts with the electric field of a nucleus. Therefore two selection rules limit the possible transitions.

1. $\Delta j = 0, +1, -1$
2. $\Delta l = \pm 1$

$\Delta l \neq 0$ is a direct consequence of the photons' parity, which is a conservative quantity in the electron photon system.
These selection rules are already considered in Figure 2.4 and give the explanation for the missing transitions for example for the change from the L_1 to the K_1 level. This transition is forbidden because of $\Delta l = 0$.

Competitively to the emission of fluorescence photons after inner shell ionization there are further processes induced by the photo effect, limiting the fluorescence yield (see Chapter 2.3.1).

2.3 Interaction of photons with matter

The impinge of a photon beam on the surface of a sample leads to various processes of photon absorption and thus to energy loss inside the specimen. Its probabilities depend on the specimen composition and the energy of the primary photons (Figure 2.5).

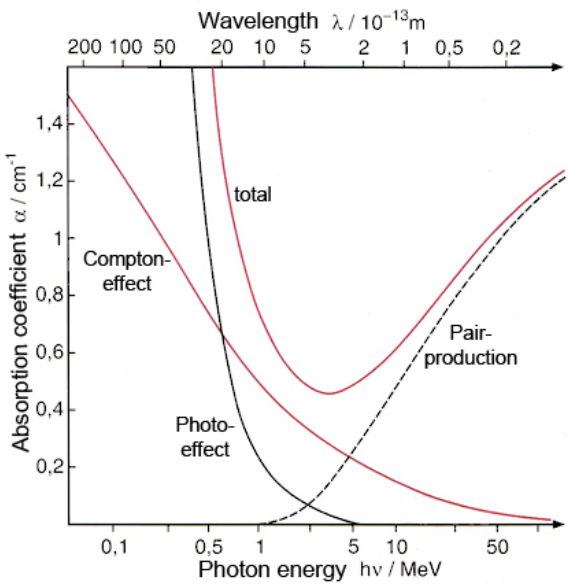

Figure 2.5: Various interactions of photons with matter influence the absorption coefficient. The figure shows the dependency on the photons energy[8](modified)

At low photon energies the photoelectric effect dominates but the yield decreases with increasing energy. hence incoherent scattering (compton effect) becomes the leading effect. Pair production occurs above 1.024 MeV and dominates at high energies depending on the elemental composition.

Coherent scattering causes broadening of the beam and thus reduced intensity, but in this case the energy is conserved. An overview of these processes is given in the next chapters, which include the explanation of bremsstrahlung as well as the characteristic radiation caused by the photoelectric effect.

2.3.1 Photo effect

The explanation of the photoelectric effect (photo effect) by Albert Einstein was a powerful proof of the corpuscular character of photons. Einstein earned the Nobel Prize in physics for these findings in 1921.
A photon with an energy $E = \hbar\omega$ higher than the ionization energy of an inner-shell electron, has the ability to transfer enough energy to allow the electron to overcome the potential barrier of the nucleus. Therefore energies at the magnitude of keV (X-ray-region of the electromagnetic spectra) are necessary. This process leads to the release of the photoelectron with an energy $E_{el} = \hbar\omega - E_B$ where E_B is the binding energy of the electron (Figure 2.6a). The created hole in one of the K or L shells corresponds to an instable excited state of the atom. In general, there are two competitive possibilities to de-energize the system.

1.) **The emission of fluorescent photons (Figure 2.6b)**
The hole in the inner shell (in Figure 2.6 the K shell) can be filled by a transition of an electron from the L shell or a higher one, following the transition rules for dipole radiation (Chapter 2.2.2). The electrons change successively their energy levels to minimize the total energy of the atom. As described in Chapter 2.2.2, fluorescent photons with a well defined energy are emitted and can be used for elemental analysis of a specimen. For high Z materials, emission of photoelectrons is the most common process after inner shell ionization.

2.) **The emission of an Auger electron(Figure 2.6c)**
After inner shell photoionization an electron transition to the K-shell occurs again. This time the energy is not used to produce a fluorescent photon but to emit an electron with characteristic energy, called Auger electron. In case of Figure 2.6c the Auger electron is called KLL electron, because it results from an electron transition from the K to the L shell and is emitted from the L shell. KLM electron emissions and other processes are also possible.
In the Auger process no photon is involved. Therefore Auger emission does not obey the rules of dipole radiation. Compared to the emission of fluorescence radiation the emission of Auger electrons is common in low Z materials.

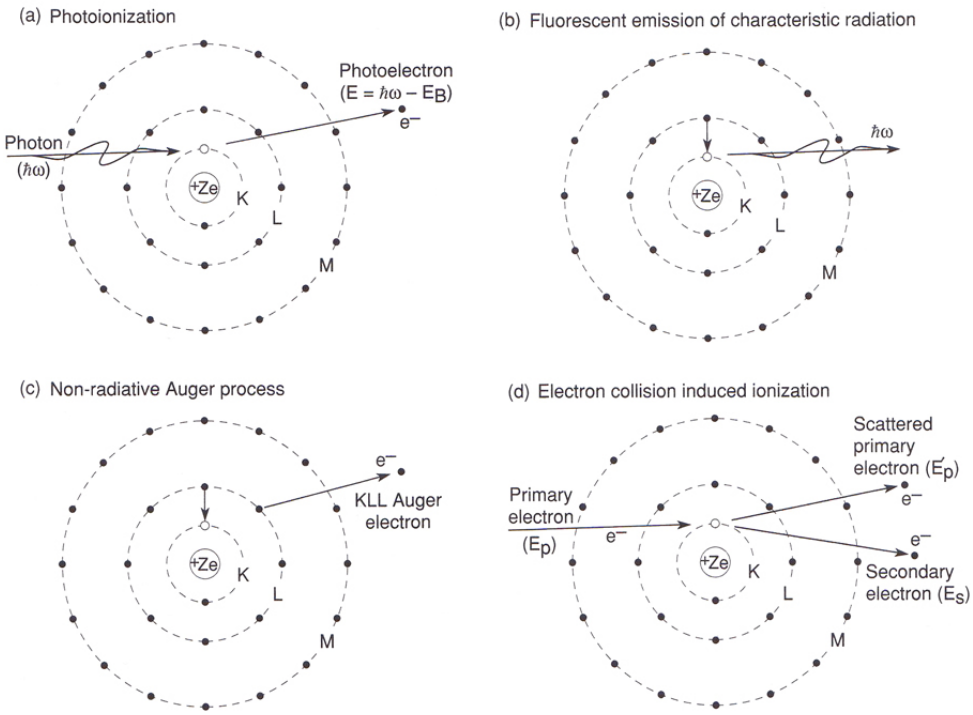

Figure 2.6: (a) Photoionization, (b) + (c) Potential subsequent processes after inner-shell ionization, (d) Electron induced inner-shell ionization [8](modified)

The Z dependency of the fluorescence yield and the auger yield are important factors for signal interpretation in X-ray-fluorescence and Auger electron spectrometry. As shown in Figure 2.7 for light elements ($Z < 10$) fluorescence analysis is difficult (but not impossible) because of the low probability of photon emission. For materials with $Z < 34$ the Auger process still dominates while for $Z > 34$ photoemission is more common.

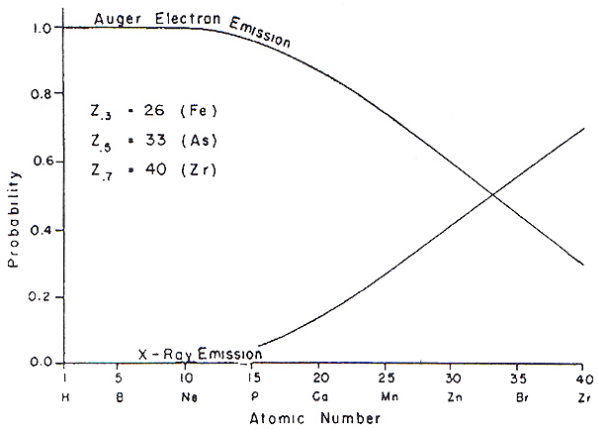

Figure 2.7: Dependency of the fluorescent yield and Auger yield on the atomic number. The controversial behavior leads to a domination of photoemission in high Z regions and low fluorescent-photon-flux at low Z targets. [9]

For the sake of completeness Figure 2.6d shows inner shell ionization induced by an impinging electron resulting in a scattered primary electron E'_p and a secondary electron E_s. This inelastic punch has a fundamentally different character compared to the photo effect, but also results in an ion with a hole in an inner electron shell. Due to these facts again either fluorescent radiation or Auger electron emission takes place. In our studies electron induced ionization plays an important role in the interaction between electrons and matter and thus in the signal interpretation of the electron microscope.

2.3.2 Coherent scattering

The content of this chapter is simplified from [10].
Coherent scattering or Rayleigh scattering explains the loss of intensity of the primary photon beam while interacting with matter, but leavs the photon energy unchanged. Rayleigh scattering of bound electrons is described by classical scatter theory where photons are treated as electromagnetic waves. It appears preferably in high Z materials at relatively low energies compared to the binding energy of the electrons.
The oscillating electromagnetic field interacts with the system of charged electrons in the atomic shells. They start oscillating with the same frequency perpendicular to the direction of propagation of the wave. The emission of radiation of moving charged particles is described by classical electrodynamics. Such an oscillating electron can be described by a Hertzian dipole, which is a source of electromagnetic radiation. So the primary electromagnetic wave superposes with the scattered one. As long as the phase shift within the atom is less than one-half of the wavelength, constructive interference happens according to the equal frequency of initial and scattered wave, but the direction of propagation is changed. The differential cross section for Rayleigh scattering (Formula 2.11) describes the angle dependency of the scattered wave.

$$\frac{d\sigma_R}{d\Omega} = \frac{1}{2} r_0^2 (1 + cos^2(\vartheta) \cdot |F(x, Z)|^2) \tag{2.11}$$

$F(x, Z)$ is the atomic form factor which depends on the type of primary radiation and the characteristics of the atom. $(1 + cos^2(\vartheta))$ describes the polarization. If ϑ equals $\pi/2$ the scattered radiation is completetly linearly polarized. With an adequate experimental setup this can be used in X-ray fluorescent analysis to minimize the signal background in the detector caused by the primary beam.

2.3.3 Incoherent scattering

While experimenting with X-rays in matter Arthur Holly Compton noticed that the scattered radiation did not only consist of a coherently scattered ($\lambda_S = \lambda_0$) fraction, but also of radiation with reduced energy ($\lambda_S > \lambda_0$). He observed an angle (φ) dependency of the wavelength distribution after scattering. In contrast to coherent scattering the interaction between a photon and a weakly bound (approximately free) electron is described. Such weakly bound electrons are located in the conduction band of metals or in the outer shells of atoms (valence electrons). Due to the low binding energy compared to the photon's energy ($E_B << h \cdot \nu_0$) the electron can be treated as a free stationary particle. In this case the corpuscular character of photons is used to describe an elastic collision between the photon with the momentum $p = \hbar \cdot k_0$ and the energy $E = h \cdot \nu_0$. Figure 2.8 illustrates the elastic process.

$$h\nu_0 + e^- \Rightarrow h\nu_s + e^-(E_{kin}) \tag{2.12}$$

The angular distribution of the photons' wavelength after scattering can be derived from the laws of the conservation of energy and momentum. Relativistic expressions are used due to the potential high velocities of the electron after the collision. A detailed calculation in [8] with $\lambda = c/\nu$ results in Formula 2.13.

$$\Rightarrow \Delta\lambda = \lambda_s - \lambda_0 = \lambda_c \cdot (1 - cos(\phi)) \quad \text{and} \quad \lambda_s = \lambda_0 + 2 \cdot \frac{h}{m_0 \cdot c} \cdot sin^2(\phi/2) \tag{2.13}$$

with the Compton wavelength $\lambda_c = \frac{h}{m_0 \cdot c}$ that stands for change in the wavelength after perpendicular scattering ($\lambda_c = \lambda_s(\pi/2) - \lambda_0$).

The expression $(1 - cos(\phi))$ provides a maximum increase of the wavelength perpendicular

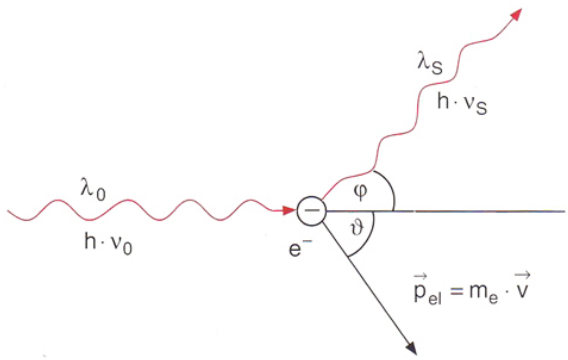

Figure 2.8: Illustration of the Compton effect [8]

to the direction of incidence ($\Delta\lambda = \lambda_c$) and unchanged wavelength in forward direction ($\Delta\lambda = 0$). According to that the phase-shift between initial and scattered wave leads to an incoherent superposition.

2.3.4 Pair production

Photons with energies larger than 1 MeV are allowed to produce an electron-positron pair in the electrostatic field of an atom. This process is known as pair production.

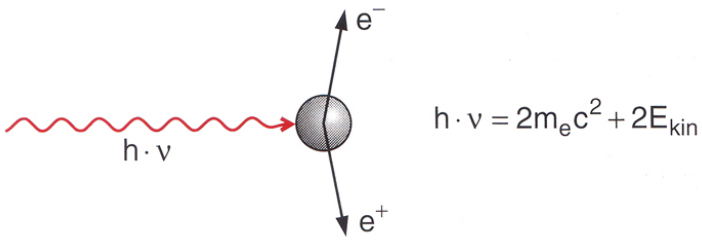

Figure 2.9: Pair production induced by a high energy photon [8]

$$h\nu \Rightarrow e^- + e^+ + 2E_{kin} \tag{2.14}$$

In coherence with the special theory of relativity, the impinging photon must carry at least the energy of $2m_ec^2$ (1.024 MeV) to produce the e^+ - e^- pairs. The remaining energy is transferred to the electron and the positron in equal parts as kinetic energy.

2.4 Attenuation coefficient and information depth

Photo effect, incoherent (Compton) scattering and coherent (Rayleigh) scattering as well as pair production cause attenuation of the X-ray beam inside a sample. Figure 2.10 shows the contribution of these processes to the total attenuation (solid line) for Pb.

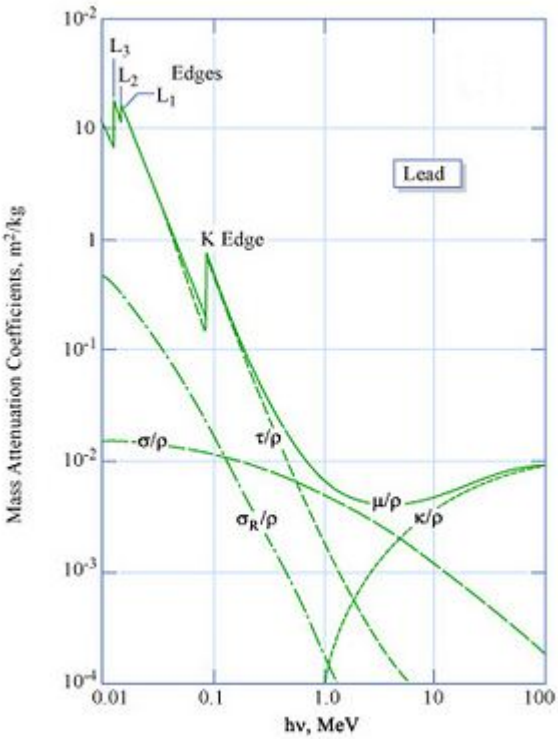

Figure 2.10: Contribution of photo effect (τ/ρ), incoh. (Compton) scattering (σ/ρ) and coh. (Rayleigh) scattering (σ_R/ρ) to the total attenuation (μ/ρ) [11]

The photoelectric attenuation τ/ρ reflects the characteristic behavior of the cross section. The displayed jumps correspond to the Pb-absorption edges. τ/ρ dominates at low energies.
The constant attenuation results in an exponential decrease of the beam intensity. This leads to a limited information depth, which is influenced by the attenuation of the primary beam on the one hand and by the absorption of the fluorescence radiation on the way through the matrix out of the sample on the other hand. According to the low energy of the secondary radiation compared to the beam energy, the decrease of the fluorescence photon intensity dominates.
For quantitative analysis as well as for the qualitative interpretation of the measured signal it is essential to know the region of origin of the fluorescence radiation. Depending on the energy (and therefore on the atomic number Z of the element) of the fluorescence radiation the information depth varies over a wide range. It can be defined using two different approaches.

1. **Definition of the information depth by the exponential attenuation coefficient [12]**
   The intensity $I(x)$ of a monochromatic beam after covering a distance x in the sample is:

   $$I(x) = I(0) \cdot e^{-\mu_L \cdot x} \tag{2.15}$$

   with the initial intensity $I(0)$ and the linear attenuation coefficient μ_L, which depends on the energy of the radiation, the composition, and the density (ρ) of the sample. So μ_L can be separated into $\mu_L = \mu_M \cdot \rho$ with the mass attenuation coefficient mu_M.

   Following Formula 2.15 the information depth d_{inf} is defined as the depth where the beam intensity decreases to the $1/e$ fold of the initial beam intensity. According to the 45° geometry in our experimental setup (Chapter 6.1) we also take into account that the depth is $d = x \cdot cos(\pi/4)$ while x is the covered distance in the sample. For this definition of the information depth the attenuation of the primary beam is neglected. In Table 2.2 one can see that this is an appropriate simplification for bone and bone-like materials if excitement occurs with MoK_α radiation (17.4 keV) or higher due to its high penetration depth compared to the Ca information depth. Figure 2.11 shows the associated exponential decrease of the intensity with increasing depth and the drastic dependency on the energy.

Element	K_α Energy $[keV]$	μ_M $[cm^2/g]$**	$\mu_L = \mu_M \cdot \rho$ $[1/cm]$	d_{inf} $[\mu m]$
Ca	3.69	230,0	437.0	16.17
P	2.02	649.0	1233.1	5.73
Zn	8.64	71.1	135.1	52.33
Sr	14.16	17.6	33.4	211.42
Mo*	17.48	9.7	18.3	386.39

Table 2.2: Calculated information depths of a bone-like material after excitation with $Mo - K_\alpha$ radiation
The bone matrix is approximated by hydroxyapatite ($Ca_{10}(PO_4)_6(OH)_2$) with a density of $1.9g/cm^3$ while the organic matrix is neglected according to its low atomic numbers.
* d_{inf} for Mo stands for the penetration depth of the primary radiation
** values of μ_M are derived from http://physics.nist.gov/cgi-bin/Xcom/xcom2

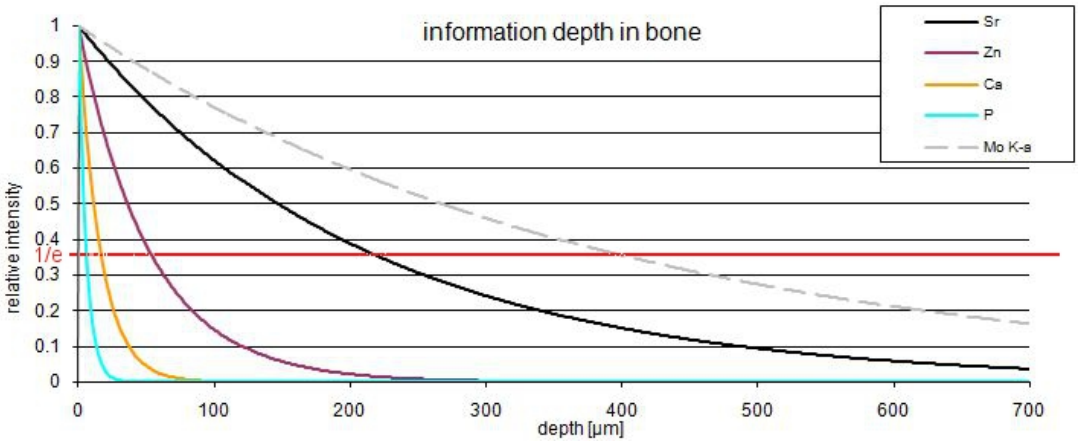

Figure 2.11: Calculated exponential decrease of the intensity for K_α radiation of Sr, Zn, Ca and P compared to the primary Mo radiation in a bone-like material.

2. **Characterization of the information depth using the $d_{99\%}$ value[10]**
If the measured fluorescence intensity of an irradiated infinitely thick specimen is set to 100%, the $d_{99\%}$ value stands for the thickness of a similar sample where the signal dropped to 99%. In contrast to the explanation using the exponential attenuation coefficient, the loss of the primary beam intensity is now included.
Mathematically this is described in equation:

$$\int_0^{d_{99\%,i}} e^{-\chi\rho z} \cdot dz = 0,99 \int_0^{\infty} e^{-\chi\rho z} \cdot dz \quad \text{leading to} \quad \rho \cdot d_{99\%,i} = \frac{-ln(1-0,99)}{\chi(E_0, E_i)} \tag{2.16}$$

with

$\chi = \mu(E_0) \cdot cos(\alpha) + \mu(E_i) \cdot cos(\beta)$
$\alpha = \beta = \frac{\pi}{4}$ in our experimental setup
$\mu(E_0)$ ... attenuation coefficient of the primary radiation
$\mu(E_i)$ ... attenuation coefficient of the fluorecence radiation of the element i
ρ ... material density

Table 2.3 summarizes the $d_{99\%}$-attenuation coefficients for Ca, P, Zn, Sr

	$d_{99\%}[\mu m]$
Ca	71.52
P	26.02
Zn	212.24
Sr	628.94

Table 2.3: Information depth of various elements characterized by the $d_{99\%}$ value assuming MoK_α energy (17.47 keV) for primary radiation in a bone-like material.

The energy dependency of the attenuation coefficient leads to a principal problem in $\mu - XRF$ illustrated in Figure 2.12. Due to absorption of the secondary radiation, the origin of a signal of low Z elements is located in the upper region of the sample. Contrarily, radiation emitted by excited high Z elements is able to escape from much deeper inside the of sample. Homogeneous (Figure 2.12a) samples with a particularly known matrix can be included in mathematical models. When an inhomogeneous sample is analyzed where the observed volume depends on the measured element, like in Figure 2.12b, quantification becomes impossible, and even the qualitative signal interpretation is problematic.

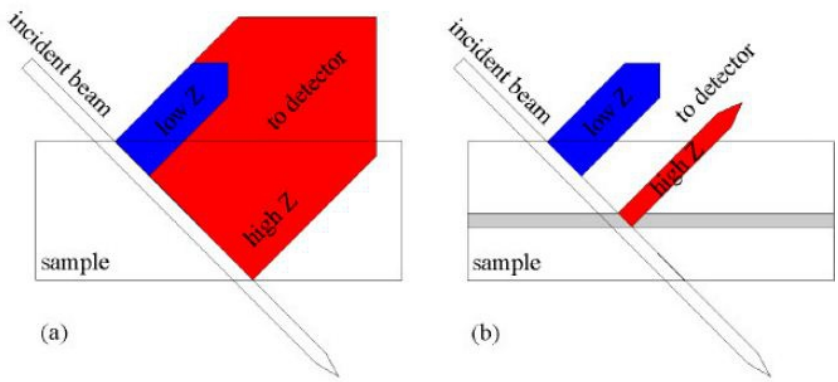

Figure 2.12: Information depths for high Z and for low Z composites in a homogeneous (a) and an inhomogeneous (b) sample [13]

The easiest way to avoid the problem of energy depending information depth is to measure thin slices of the specimen. If the sample-thickness is below the information depth of the lightest element only small errors occur.

Another elegant way to measure a well-defined volume is to choose a confocal experimental setup as described in chapter 6.1. In conventional micro-XRF the beam is focused (usually with a capillary, see Chapter 2.6.3) to a small spot on the sample while the aperture angle of the detector is large to collect as many photons as possible. For confocal measurements a second capillary is mounted between sample and detector so that the focal spot overlaps with the source side capillary as shown in Figure 2.13.
This setup ensures that only fluorescent photons emitted in the overlap of the two focal spots are counted. Therefore the problem of variations in the information depth is reduced, but another effect complicates attempts of quantification: Photons at the wall of the capillary are total-reflected to be guided to the detector. Unfortunately, the critical angle of total reflection depends on the energy of the photon, which causes variations in the size of the focal spot of the capillary (Chapter 2.6.3) and thus in the observed volume. If quantification of the sample is desired this effect must be corrected using the transmission function of the detector sided capillary.

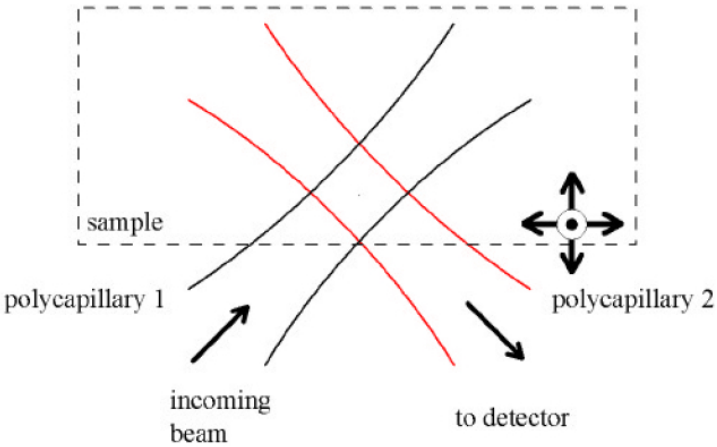

Figure 2.13: Illustration of a confocal setup with overlapping spots [13]

2.5 Characteristics of X-ray-fluorescence analysis

The idea of X-ray fluorescence analysis the use of characteristic radiation (described in Chapter 2.2.2) to get information of the elemental composition of an unknown sample. For this purpose various projectiles can be used to induce the emission of characteristic photons (2.3.1) beside photons. Photons, electrons or in some cases protons are used. Proton bombardment (PIXE) offers high sensitivity to low concentrations and a lateral distribution at the micron range, but leads to destruction of biological samples. In scanning electron microscopes beside primary and secondary electrons, the produced fluorescence radiation can be used for sample analysis. Despite of the small focal spot of the electron beam the fluorescence resolution is limited to about one micron according to the spread of the electrons below the surface (also see Chapter 3). Furthermore, the intense background radiation, resulting from secondary electrons and inelastic scattering, complicates signal interpretation, which makes a quantitative analysis extremely hard. Photons have the ability to create characteristic radiation with low background compared to other projectiles. Photons seem to be the best choice for projectiles as long as a high photon flux is available and a small focal spot is achieved, if non-destructive analysis is desired. If information about the light elements (elements below Carbon) is not required, the measurements can be performed in air. The brilliance of an X-ray tube is restricted due to the low efficiency. Hence micro-XRF (XRF with a small focal spot) becomes problematic when analyzing trace elements in low concentrations.

The situation improves if a homogeneous big bulk sample (with a diameter at the range of 1 cm) is analyzed with conventional XRF. In this case discharge tubes (sometimes in combination with secondary targets) are adequate photon sources and provide short measurement times and in many cases, depending on the sample, the ability to quantify its elemental composition.

When analyzing biological material like bone, which is highly inhomogeneous, micro-XRF is the method of choice, especially when the interest lies in the spatial distribution of the elements. Only a synchrotron radiation source provides an appropriate photon flux for a spatial resolution of about 10 microns (the exact experimental setup is described in Chapter 6.1). So a specimen can be scanned point after point with typical irradiation time ranging from 1 to 60 seconds, depending on the concentration of the element of interest. With an appropriate experimental setup a pixel with 10×10 μm represents the averaged information of a $10\times10\times10$ microns voxel just below the surface. The process leading to this signal is described in the following chapter.

2.5.1 Fundamental parameters and quantitative analysis

Figure 2.14 shows a typical geometry for a micro-XRF analysis. The angle between sample and X-ray source and the angle between sample and detector is 45°. As a consequence there is an angle of 90° between the incoming and the emitted photon flux. For the interpretation of the measured signal and especially if quantification is desired, several effects and processes have to be taken into account.

To derive the measured fluorescence intensity of a certain electron transition, following factors have to be considered:

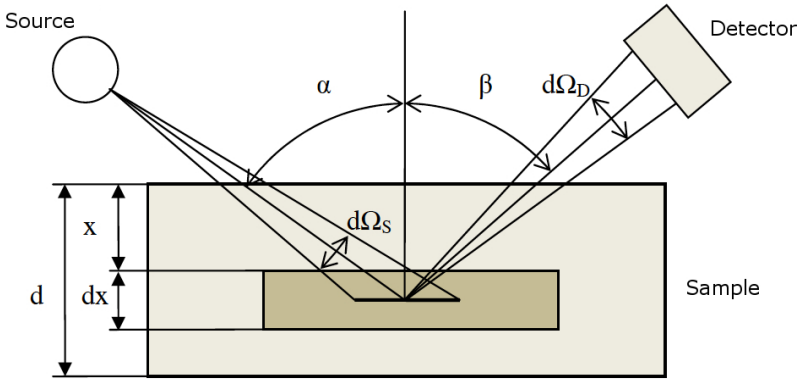

Figure 2.14: Typical XRF-Setup with the characteristic parameters[14](modified)

In the nomenclature i is the index of the element of interest. k stands for the initial and j for the final shell of the transition. The formulas are taken from [14].

- $I_0 \Rightarrow$ intensity of the primary beam
- $\Omega_D \Rightarrow$ spatial angle of beam spread of the primary photon beam
- $\Omega_S \Rightarrow$ aperture angle of the detector
- $S_{ij} \Rightarrow$ ionization possibility of the jth shell of the element i
- $p_{ijk} \Rightarrow$ possibility for a $k \rightarrow j$ transition of the element i
- $\omega_{ij} \Rightarrow$ fluorescent yield of the jth shell of the element i
- $\epsilon_{Eijk} \Rightarrow$ detector efficiency at the energy E, depending on the involved shells j and k and the element i
- $c_i \Rightarrow$ concentration of the element i
- $\rho_c \Rightarrow$ density of the sample calculated from $\frac{1}{\rho_c} = \sum_i \frac{c_i}{\rho_i}$
- $\tau_{K,i}(E)/\rho_i \Rightarrow$ photoelectric mass attenuation coefficient of the element i at the K-edge, depending on the primary energy E (see Chapter 2.4 for further explanation). Since τ is the total photoelectric attenuation, τ_K derives to $\tau_K = \tau(1 - 1/S_K)$ with the absorption edge jump of the K-edge S_K.
- $\mu_c(E) \Rightarrow$ linear attenuation coefficient
- α and β are the angles of impinging and emitted beam and equal 45°in our experimental setup

The photon beam penetrates the sample with an angle of spread of Ω_S to a depth x. There the primary photons cause inner shell ionization in regions symbolized by dx. Fluorescent photons are produced and emitted over a wide range of angles, but only those within the spatial aperture angle of the detector Ω_D are measured. To get the total number of counted photons we have to integrate over $d\Omega_S$, $d\Omega_D$, the depth x and the energy E.

With this definitions a general formula for measured intensity can be derived.

$$I_{ijk}^{prim} = \frac{d\Omega_d d\Omega_S}{4\pi \cdot cos(\alpha)} \cdot p_{ijk} \cdot \Omega ij \cdot \epsilon(E_{ijk}) \cdot c_i \cdot \tag{2.17}$$

$$\int_{E_{ijk}}^{E_{max}} dE \cdot I_0(E) \cdot \frac{1 - e^{-[(\frac{\mu_c(E)}{\rho_c})\frac{1}{cos(\alpha)} + \frac{\mu_c(E_{ijk})}{\rho_c}\frac{1}{cos\beta}]\cdot\rho_c\cdot d}}{[(\frac{\mu_c(E)}{\rho_c})\frac{1}{cos(\alpha)} + \frac{\mu_c(E_{ijk})}{\rho_c}\frac{1}{cos\beta}] \cdot \rho_c} \left(\frac{\tau(E)}{\rho_i}\right) \cdot S_{ij}(E) \tag{2.18}$$

The probability of the occurrence of a certain line is characterized by the product $p_{ijk} \cdot \omega_{ij}$. Attenuation of the primary photon beam is described by the factor

$$e^{-\frac{\mu_c(E)}{\rho} \cdot \frac{x}{cos(\alpha)}}. \tag{2.19}$$

But also the fluorescent beam becomes weaker on its way through the sample. This is described similarly.

$$e^{-\frac{\mu_c(E_{ijk})}{\rho} \cdot \frac{x}{cos(\alpha)}} \tag{2.20}$$

Formula 2.17 can be simplyfied by executing the dx integration, the definition of the absorption factor $A(E)$, and the fluorescent-cross section $\sigma_{ijk}(E)$.

$$I_{ijk}^{prim} = \frac{d\Omega_d d\Omega_S}{4\pi \cdot cos(\alpha)} \cdot \epsilon(E_{ijk}) \cdot c_i \cdot d \cdot \rho_c \int_{E_{ij}}^{E_{max}} dE \cdot I_0(E) \cdot A(E) \cdot \sigma_{ijk}(E) \cdot S_{ij}(E) \tag{2.21}$$

with

$$A(E) = \frac{1 - e^{-[(\frac{\mu_c(E)}{\rho_c})\frac{1}{cos(\alpha)} + \frac{\mu_c(E_{ijk})}{\rho_c}\frac{1}{cos\beta}]\cdot\rho_c\cdot d}}{[(\frac{\mu_c(E)}{\rho_c})\frac{1}{cos(\alpha)} + \frac{\mu_c(E_{ijk})}{\rho_c}\frac{1}{cos\beta}] \cdot \rho_c \cdot d} \tag{2.22}$$

$$\sigma_{ijk}(E) = p_{ijk} \cdot \omega_{ij} \cdot (\frac{\tau_{K,i}(E)}{\rho_i}) \tag{2.23}$$

where p_{ijk}, ω_{ij} and $\tau_{K,i}(E)/\rho_i$ are called fundamental parameters.

Since the linear absorption coefficient itself depends on the matrix composition ($\mu_c = \Sigma_i(\mu_i c_i)$), the quantification of an unknown sample without standards is problematic.
An approximation of Formula 2.22 can be made for monochromatic excitement. Whereby the energy integral is redundant because of the trivial spectral distribution. In the case of infinite thick or thin samples the absorption factor $A(E)$ can be drastically simplified. As see before, it is in principal possible to calculate the intensity of the fluorescent photons as long as the matrix composition is perfectly known. In a more precise model matrix effects must be included, considering that the fluorescence radiation of one element might have the ability to excite another element. This is called secondary excitement. Again, as long as the matrix composition is known calculations lead to consistent results. The situation becomes more complicated if it is required to determine the percentage of an element in the sample by means of the measured fluorescent intensity.

2.6 X-ray techniques

Figure 2.15 shows the principle experimental of an setup for fluorescence analysis. X-ray tubes, SR-sources or radioactive sources provide a photon flux which is used for elemental excitement inside the sample. The semiconductor crystal detects the fluorescence radiation resulting in a low electron flux which is further processed by the preamplifier, the amplifier and the multi channel analyzer (MCA).

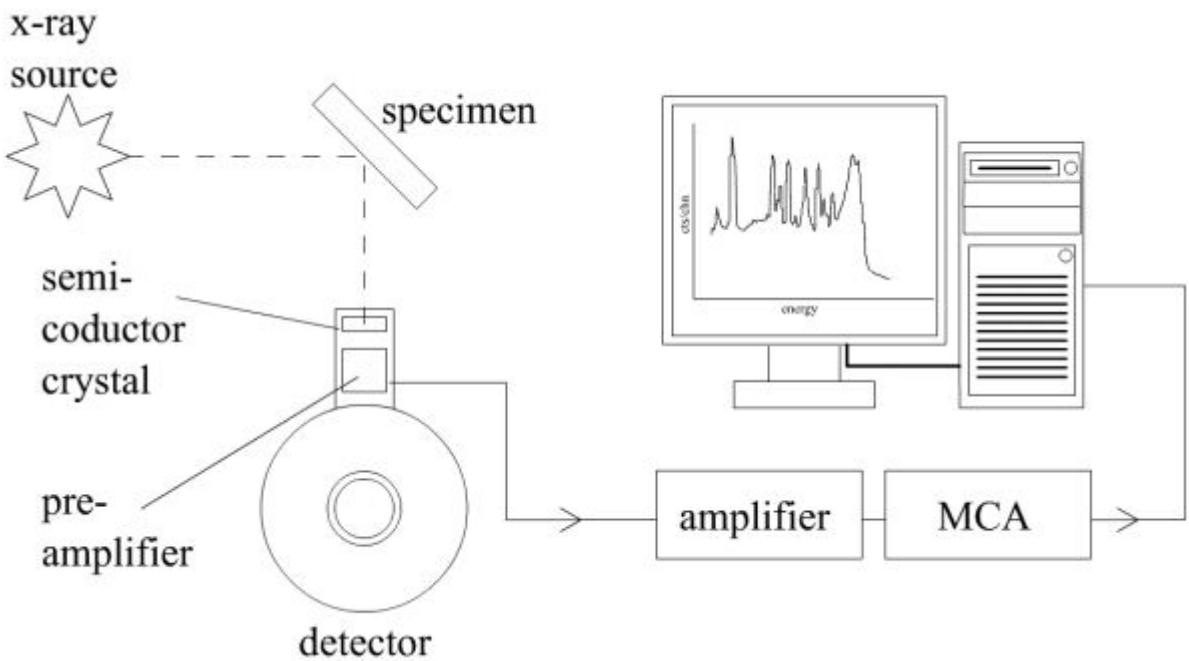

Figure 2.15: Typical setup of an X-ray spectrometer and the signal prosessing devices [13]

2.6.1 X-ray sources

In general, there are several processes leading to the emission of characteristic X-rays and bremsstrahlung. In laboratories X-ray tubes (discharge tubes) provide an adequate photon flux for a wide range of applications. According to long durability and low operating expenses, discharge tubes are used for qualitative and quantitative conventional X-ray fluorescent analysis, grazing incidence and total reflection analysis (TXRF), XRF of low Z elements, micro-XRF analysis, micro-computer tomography (μCT) as well as for a broad bandwidth of medical applications.
If portability and compactness is needed, radioactive sources are often used. In this case a γ emitter is mounted near a secondary target and causes photoionization equivalent to the X-ray induced photo effect in Chapter 2.3.1. Compactness and simplicity of this kind of X-ray source are opposed by a low photon flux, a limited life period of the radioactive source (depending on the elemental half life), and last but not least by the strict security restrictions of radioactive materials.
Nowadays synchrotron radiation (SR) sources provide the most intense and most brilliant sources of electromagnetic radiation. The high photon flux combined with the wide ranging continuous spectrum and a small aperture angle allows a large number of examinations. The requirements for infrared spectroscopy on low energy side as well as excitement of heavy elements for XRF with hard X-rays are fulfilled. Because of their importance for the analysis of biological samples the functionality of X-ray tubes and synchrotrons will be discussed in the following chapters.

2.6.1.1 X-ray tubes

The main parts of an X-ray tube (or discharge tube) are a cathode (in most cases made of tungsten) and an anode consisting of a heavy element with a Z, depending on the desired X-ray energy. Typical anode materials are tungsten, molybdenum, copper, or rubidium. For focusing reasons a wehnelt-cylinder, which is held on slightly negative voltage, is mounted around the cathode. Figure 2.16 shows a typical design of a discharge tube. The cathode current ranges from μA up to some mA and heats the tungsten coil to reduce the electron's work of escape. The applied high voltage ($\approx 10 - 60\ kV$) relative to the anode effects electron release, acceleration of the electrons on their way to the anode, and consequently the impinge on the anode material. For cooling reasons in most cases the anode is on ground potential.
As suggested in Chapter 2.3.1 electron-electron interaction leads to inner shell ionization of the anode material followed by a series of electron transitions (causing the emission of characteristic X-rays) as well as the emission of Auger radiation. Both, deceleration of the primary cathode-electrons as well as deceleration of the secondary electrons from the anode lead to a superposition of characteristic X-ray peaks and continuous bremsstrahlung. In Figure 2.17 the bremsstrahlung-spectrum is superposed by sharp and intense characteristic X-ray peaks of the Mo-anode. The K_α, K_β and the indistinguishable L - lines can be identified clearly. The alignment of the anode and the position of the exit window allow modulations of the beam profile. An anode surface not perpendicular to the electron beam with the take-off angle α and a side window lead either to a small point-focal spot

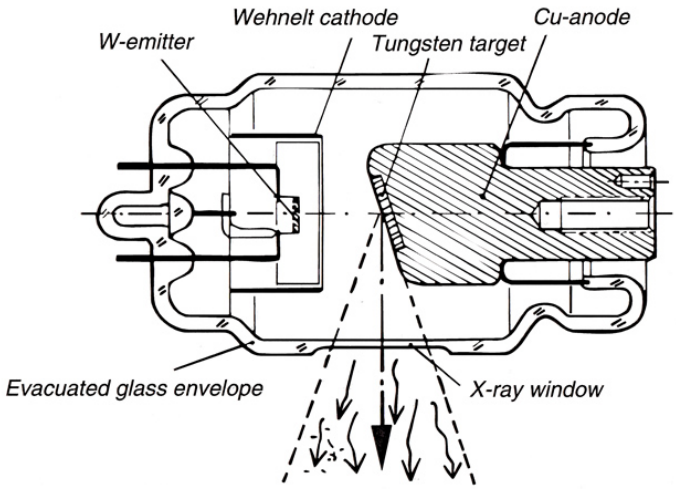

Figure 2.16: Basic design of a X-ray Tube with a side window. [15]

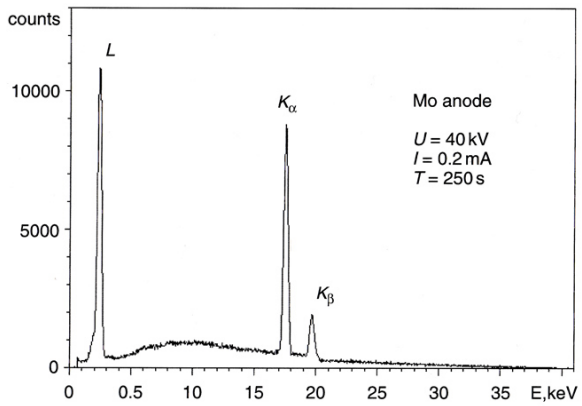

Figure 2.17: Spectrum of a discharge tube with Mo anode after 250 seconds exposure time. The cathode current is set to 0.2 mA while a high voltage of 40 kV relative to the anode is applied. [15]

if the setup is similar to Figure 2.18 or a focal spot in a bar-style if the window is placed in other directions. To reduce scattering of electrons on their way through the tube it

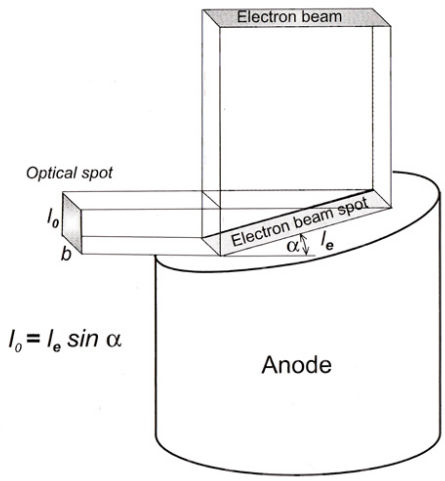

Figure 2.18: Electronic and optical focal spot, depending on the take off angle α [15]

is essential to operate in high vacuum. Therefore cathode and anode are placed in an evacuated glass cylinder with a typical pressure of 10^{-4} Pa. As a matter of fact the exit window is a weak spot where interpenetrability for air as well as low X-ray absorption must be assured. For this purpose a thin Be window with a thickness of $100 - 200$ μm is typically used.
Since the efficency of an X-ray tube is about only 1%, the electron impinge on the anode leads to a drastic raise in temperature. Consequent cooling becomes important to avoid damage to the anode. A watercooling or - as installed in most of the tubes for medical examinations - a rotating anode (up to 20000 min^{-1}) helps to solve this problem.

2.6.1.2 Synchrotron radiation

In the last years the importance of synchrotrons for elemental and molecular research raised drastically. During the first synchrotron-boom at the end of the fifties, collision experiments were performed to study the interaction of various particles. Electromagnetic radiation of charged accelerated particles, called synchrotron radiation (SR) was observed. Nowadays a lot of synchrotrons are built to use SR for analysis using a broad bandwidth of methods. In coherence to our experiments in the following explanations electron-synchrotrons are assumed to be used.
Compared to X-ray tubes synchrotrons provide a high photon flux combined with a natural collimation and a "white" radiation containing frequencies reaching from the low infrared side of the spectrum up to hard X-rays on the high energy side. Natural collimation, polarization and the intensity of the beam provide excellent measurement conditions.

Figure 2.19 shows a common synchrotron design with a linear accelerator combined with a small booster-ring for pre-acceleration. After injection into the main storage ring the

particles are focused by the inhomogenous fields of multiple magnets (green device in the figure). Ring currents are typically are at the range of 100 to 1000 mA whereby the electrons have a lifetime of several hours. The electron energy is in the magnitude of GeV. Bending magnets (red devices) are used to change the flight direction and to produce synchrotron radiation for experimental use. With undulators and wigglers (orange modules) magnets with alternating orientations provide brilliant radiation with a small aperture angle.
The so produced beam is collimated by a slit system before a monochromator selects the desired wavelength of the beam spectrum.

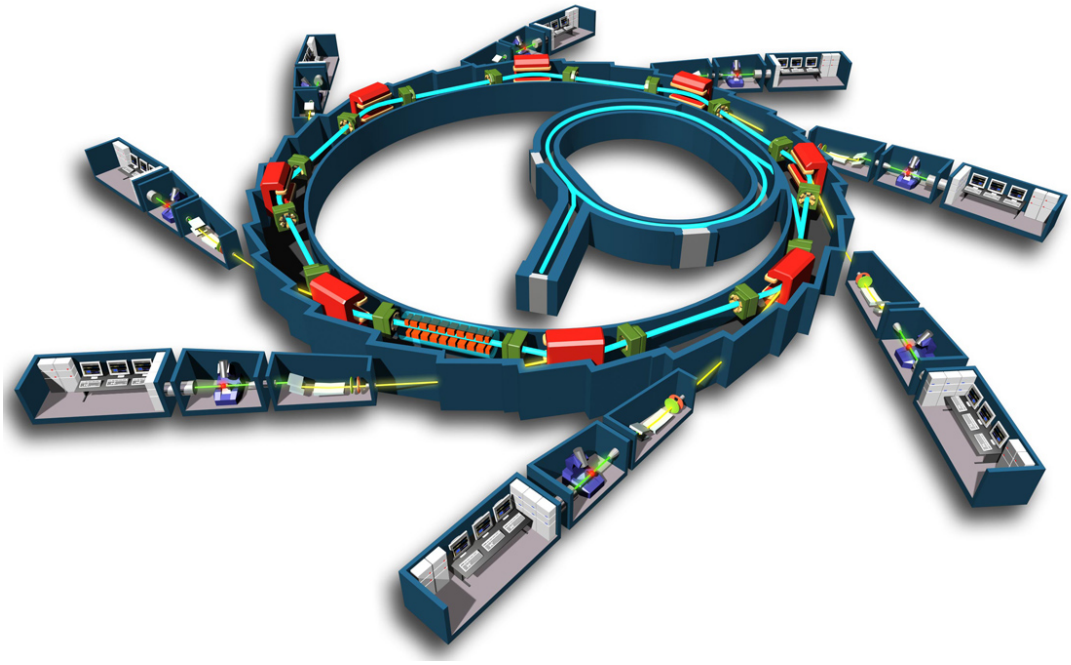

Figure 2.19: Synchrotron with a linear accelerator and a smaller booster ring inside. Multiple beamlines for various experimental setups are shown. [16]

As a consequence of the fundamental Maxwell equations accelerated charged particles emit electromagnetic radiation. In case of magnetic deflection a detailed relativistic consideration predicts collimation of the emitted radiation tangential to the particles' path with an opening angle depending on the speed of the particle (Figure 2.20). The emission

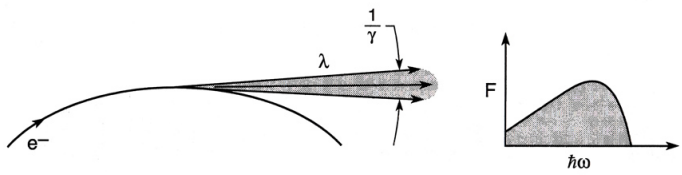

Figure 2.20: Tangential emission of electromagnetic waves caused by a bended path of an electron. [7]

angle $\frac{1}{\gamma}$ defines the collimation of the photon beam and decreases with the raise of the

particles' speed v.
γ is the Lorentz contraction factor:

$$\gamma(v) = \frac{1}{\sqrt{1 - \frac{v^2}{c^2}}} \tag{2.24}$$

Current, brightness, total photon emission, and brilliance are important parameters to characterize the quality of synchrotron radiation and are linked with the photon flux.

- **Brightness**
  Assuming a negligible angular divergence of the electron beam, the photon brightness is defined as

  $$\frac{d^2 I}{d\Theta \cdot d\varphi} = 1.327 \cdot 10^{13} \cdot E^2[GeV] \cdot i[A] \cdot H_2\left(\frac{\omega}{\omega_c}\right) \tag{2.25}$$

  Θ and φ are emission-angles in the orbit plane and are perpendicular to this plane. The electron energy in GeV and the ringcurrent in ampere are multiplied with the tabulated Bessel-function $H_2(\frac{\omega}{\omega_c})$ considering that photons have the angular frequency [17].

- **Total photon emission** The φ integration of Formula 2.25 leads to

  $$\frac{dI}{d\Theta} = 2.457 \cdot 10^{13} \cdot E[GeV] \cdot i[A] \cdot G_1\left(\frac{\omega}{\omega_c}\right) \tag{2.26}$$

- **Brilliance**
  Usually angular divergence and size of the electron beam must be taken into account. Thus the brilliance is normalized by the electron beam cross section. Figure 2.21 shows the brillance of the National Synchrotron Light Source NSLS (New York) as a function of the energy. Note the wide energy range of the continuous spectral distribution.

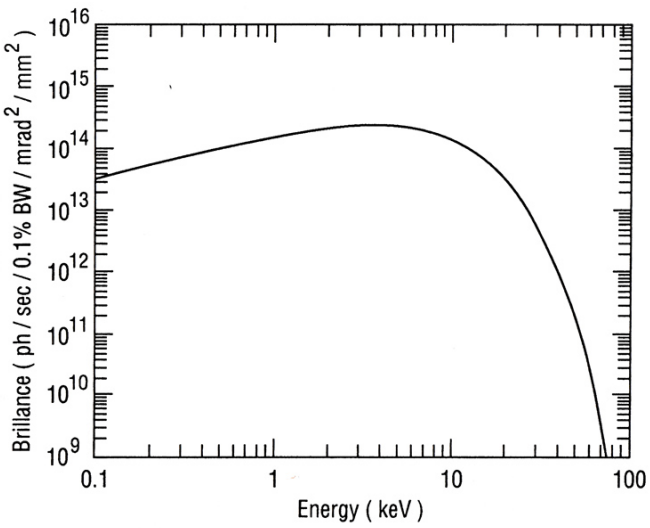

Figure 2.21: Brilliance as a function of the photon energy, characterizing the beam quality of the NSLS synchrotron. [18]

In contrast to the brightness, now collimation of the electrons and the spectral bandwidth are taken into account. Thus the unit of the brilliance is

$$\frac{Photons/s}{mrad^2 \cdot mm^2 \cdot 0.1\% spec.Bandwidth} \tag{2.27}$$

Beside simple bending magnets, wigglers, and undulators are used to produce synchrotron radiation for experiments. They afford higher photon fluxes and thus better brilliance. During the last years such devices have become more and more important.

- **Undulators**
  Periodical, alternating adjustment of a large number of magnets with moderate field strength along the electron path causes oscillations due to the alternating changes in direction of the Lorentz force and hence also the tangential emission of synchrotron radiation. For example in 2007 an undulator was installed at the Petra III storage ring, consisting of 688 small dipoles. The distance of two magnets with similar polarization (λ_u) and the field strength are chosen adequately to provide coherent interference of the emitted radiation. Consequently, depending on the number of oscillation periods, the opening angle of the photon-emission cone (θ) and the spectral bandwidth (λ) are reduced resulting in a raised brilliance.

$$\lambda \approx \frac{\lambda_u}{2 \cdot \gamma^2} \qquad \text{and} \qquad \Theta \approx \frac{1}{\gamma\sqrt{N}} \tag{2.28}$$

As shown in Figure 2.22, the beam can be used for experimental purposes, after passing a pinhole filter. The deflection parameter K describes the electrons' deflection

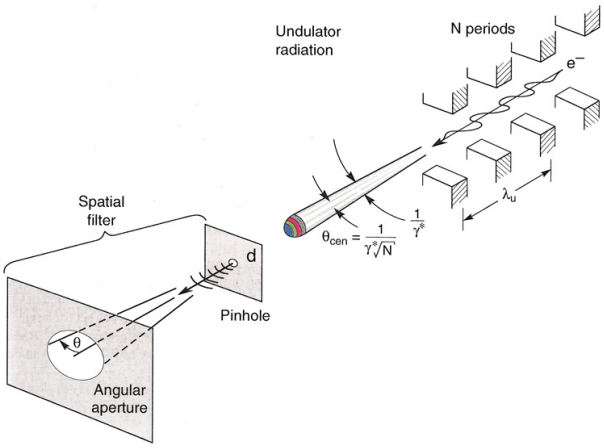

Figure 2.22: Scheme of synchrotron-radiation production in an undulator[7](modified)

when passing a magnetic field B_0.

$$K = \frac{eB_0\lambda_0}{2\pi mc^2} \tag{2.29}$$

In case of an undulator the magnet period length λ_0 equals λ_u in Figure 2.22. To allow coherent superposition $K < 1$ must be fulfilled.

- **Wigglers**

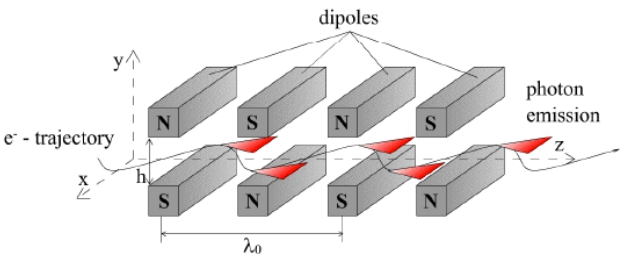

Figure 2.23: Magnet alignment and beam deflection in a wiggler. [13]

Contrarily to undulators, K is much larger than 1 for wigglers. The magnetic fields are stronger and hence, the deflection of the electrons. Therefore, the conditions for coherent superposition are not fulfilled. This results in a larger opening angle and a broader spectrum compared one of an undulator. Since N is the number of oscillation periodes, the brightness in the emission cone center of a wiggler is $2N$ times higher compared to a bending magnet.

Another beneficial property of synchrotron radiation is its linear polarization which is parallel to the orbital synchrotron plane. Especially for fluorescence analysis, the use of polarized radiation can help to reduce the signal background.

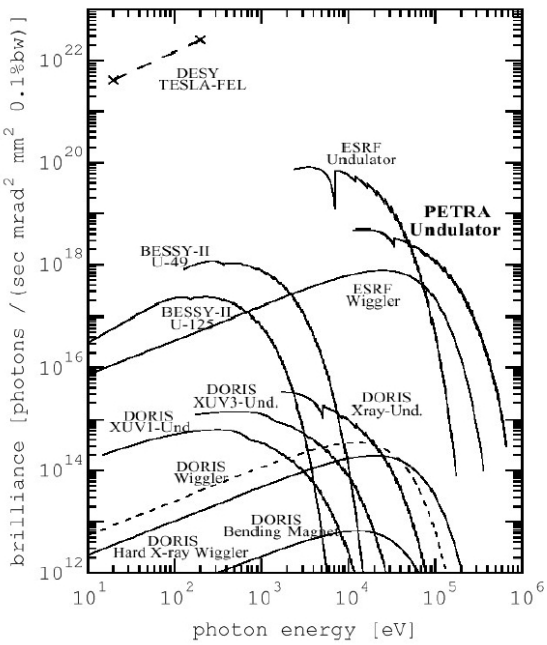

Figure 2.24: Brilliance comparison of bending magnets, wigglers, and undulators installed in various synchrotrons[13]

Summarizing, the main advantages of synchrotron radiation are [10]:

- broad continuous spectra reaching from hard X-rays down to low energy infrared radiation,
- great intensity compared to other sources of radiation (except lasers),
- high collimation of the emitted radiation,
- linear polarization in the synchrotron plane,
- the spectral distribution of synchrotron radiation can be derived theoretically, and hence facilitates the calibration of detectors.

2.6.2 Semiconductor detectors

A semiconductor is a material acting like an insulator at low temperatures but becomes conducting above a critical temperature or during exposure to radiation. This behaviour is a result of weakly bound valenc electrons, which can be transferred to the conducting band easily by absorbing low amounts of energy. Doping with atoms carrying one electron more (n-type) or one electron less (p-type) than the original semiconductor leads to extremely weak bound valencelectrons resulting in a high sensitivity to external influences. If a photon interacts with the semiconductor material, electron-hole pairs are produced. An applied voltage accelerates them to the poles, resulting in in a current, proportional to the number of the electron-hole pairs and thus proportional to the energy of the photon. In practice a combination of a p-type and a n-type semiconductor crystal (diode) is used for the detection of X-rays. At the interface of two differently doped crystal, electrons drift from the n-type to the p-type region. When equilibrium is reached, the interface can be seen as a barrier layer, which expands when a positive voltage is applied on the n-doped side and a negative one at the p-doped side. An invert voltage leads to reduction of the barrier zone and therefore to current. A reverse-biased diode can be used as radiation detector, because the barrier zone acts as a radiation-sensitive volume. In such a device, current is observed beeing proportional to intensity and energy of the incident radiation. PIN diodes are based on these principles.

2.6.2.1 PIN diodes

Figure 2.25 shows the structure of a PIN diode with a narrow p-type region on the left side and an n-type layer on the right side, separated by a large zone without doping (intrinsic zone). Applying a high negative voltage on the side of p-type doping (reverse-biased) extends the barrier zone over the intrinsic zone, which consequently becomes sensitive to incident radiation. Figure 2.25 illustrates the impinge of a photon, producing electrons and electron-holes. The high voltage accelerates them to the cathode and the anode, which are coated with gold to establish the contact to the preamplifier.

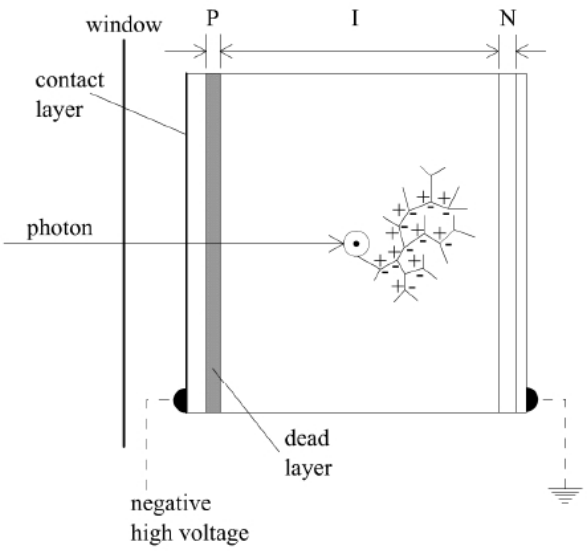

Figure 2.25: Scheme of a Si(Li) detector as example for a PIN - type device. [13]

2.6.2.2 Si(Li) Detector

The silicon-lithium drift design is a common solution for X-ray detection. Basically, it is a PIN diode as shown in Figure 2.25 with the intrinsic zone I as X-ray sensitive area. The production of the p-type and n-type zones are realized by a weakly doped p-type Si-crystal that is brought into thermal contact with Li on one side while the other side is in high vacuum. When the crystal is heated (typically 300°C - 600°C) diffusion processes make the Li diffuse into the crystal.This results in a decreasing Li concentration linked with the distance to the surface. Subsequently, at lower temperatures (100°C - 200°C) a reversly-biased voltage is applied forcing the Li atoms to drift in the p-type region. Consequently the intrinsic zone between the n-type side and the p-type side grows. When the crystal is cooled down the Li atoms lose their movability.

Figure 2.26 compares Si and Ge detectors, with either Si or Be windows. The detector efficiency is restricted according to the window material and thickness at the low energy side.

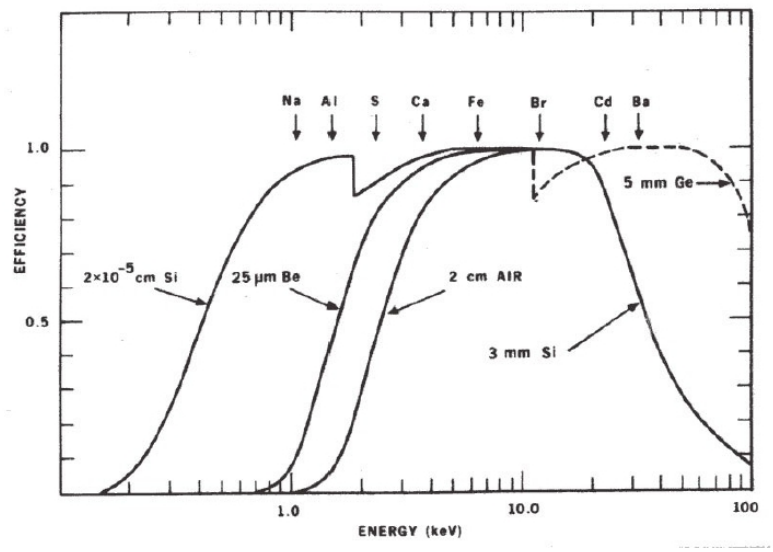

Figure 2.26: Efficiency of Ge and Si detector designs with either Si or Be window. [19]

The choice of the detector window material is important, especially when the observation of low Z elements is desired. Mostly $10 - 100$ μm Be folis (which unfortunately absorbs low energy X-rays) are used. Therefore, for the detection of low energy fluorescent lines, ultrathin polymer windows must be installed. As shown in Figure 2.27 modern detector windows still have good transitions below 1 keV.

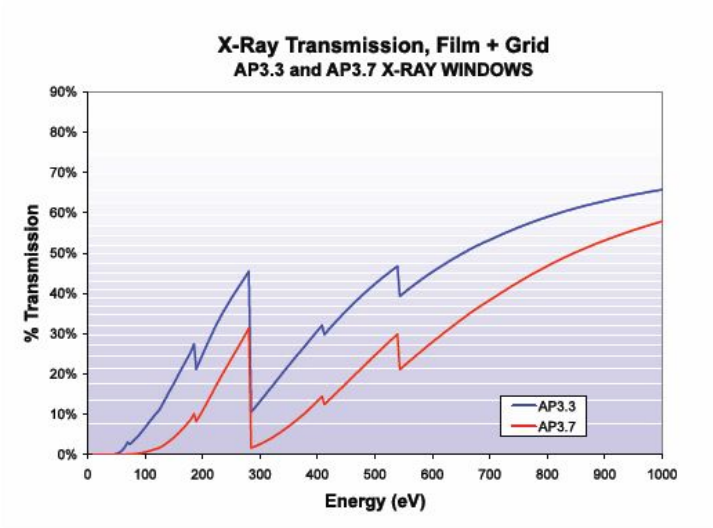

Figure 2.27: Transmission of two ultrathin polymer windows [20]

2.6.2.3 Signal processing and detector artifacts

The current pulse produced by the detector gets immediately preamplified. Then it is guided to a secondary amplifier before the pile-up rejector prohibits energy summation of overlapping pulses by closing the gate for a certain time after each pulse. Afterwards the

Analog-Digital-Converter (ADC) produces a digital signal. The Multi Channel Analyzer (MCA) counts the events for each energy interval $E + \Delta E$ using typically 1024 channels. Therefore, after an energy calibration every channel can be linked with an energy interval.

In principal a higher countrate leads to better statistics and hence to shorter measurement times. But for processing a signal the electronics needs some time to be ready for the next count. Hence, in this time new events are neglected (dead time). So depending on the quality of the electronics at a high countrate, the results have to be corrected for dead time. Likewise if the countrate is too high, the photon flux must be reduced using either a lower flux for excitement or a detectorfilter ($\approx 30 \mu m$ Al foil is often used). With a modern digital pulse processor, it is possible to handle high countrates in the order of 100 000 counts per second.

Detector artifacts are peaks in the spectrum caused by processes in the detector, which cannot be related directly to the energy of the incident radiation. Hence they do not carry additional information but have to be considered in the interpretation of the spectra.

- **Escape-peaks**
  Since incidence radiation interacts with the detector material (for example Si) there is a certain probability for inner shell ionization and thus for the emission of characteristic Si-photons. As long as they are absorbed in the sensitive volume of the detector crystal the whole energy of the primary photon is measured. But of course the Si-photon can escape the crystal carrying a well defined energy (1.74 keV in case of SiK_α radiation). As a result the spectrum shows an additional line with a shifted energy of 1.74 keV to the low energy side.

- **Sum peaks**
  If two current pulses occur simultaneously, the pile-up rejector, which acts as pulse discriminator, is not able to distinguish them. Consequently they are treated as one pulse with double energy. This artifact becomes evident when working with high countrates. In the case of Ca in bone, which accounts for about 20% of the mineralized matrix, even triple sums were observed.

- **Compton edge**
  The Compton edge is located at the low energy side of the spectrum and is caused by photons, backscattered at the front of the detector. See Chapter 2.3.3 for a detailed explanation of Compton scattering. 180° scattering of the photons leads to a scattered electron straight into the sensitive region of the detector. Other energies of the Compton spectrum are related with scatter angles around 180°.

2.6.3 X-ray optics

X-ray optics are needed for focusing reasons, for collimation, as waveguides, and for monochromation. Therefore, the optical devices can be dissected into three groups. Capillary optics are based on total refection and are often used for collimation or focusing. The latter can also be realized by electron lenses or mirror optics (often realized as two

curved single mirrors in the Kirkpatrick-Baez design). Another very important application for X-ray mirrors are monochromation optics using Bragg reflection for wavelength selection. For the sake of completeness also Fresnel-zone plates should be mentioned as alternative focusing devices, based on the principle of X-ray diffraction.

2.6.3.1 Capillaries

X-ray capillaries are based on total reflection inside a narrow glass tube. Generally total reflection occurs at grazing beam incidences on interfaces with differing refraction indices; exactly, inside a medium with high optical density at the interface to a medium with lower optical density. For example in case of visible light, total reflection is observed inside water at the interface to air. The critical angle for total reflection Θ_c is linked with the ratio of the refraction indices. In Formula 2.30 n_1 is the medium of propagation of the primary beam. As long as $\Theta > \Theta_c$ total reflection occurs.

$$sin(\Theta_c) = \frac{n_2}{n_1} \tag{2.30}$$

The refraction index n for vacuum equals 1 and for visible light in matter $n > 1$ holds. The situation changes when experimenting with X-rays, facing a refraction index between 1 and 0 as some solids like glass have. In this case vacuum or air are the materials with higher optical density. Consequently total reflection is supposed to occur in air or in vacuum at the interface to glass at grazing incidence. Unfortunately the refraction index and thus the critical angle of X-rays in matter depend on the photon's energy. So especially for quantitative analysis, the change of the photon-beams' spectral distribution (transmission-function) must be taken into account.
Monocapillaries and polycapillaries can be distinguished.

1. **Monocapillaries**
   The simplest capillary type is a cylindrical monocapillary illustrated in Figure 2.29a. A photon from the source with an emission angle Θ_0 enters the capillary and (as long as Θ_0 is bellow the critical angle for total reflection) the photon is total-reflected on the walls of the capillary, and thus it is guided to the other end without loss of intensity. Since the capillary is cylindrical, no focusing occurs but compared to a pinhole collimator a gain factor (I_g) is defined. Figure 2.28 illustrates this definition with the solid angles at positions of the critical angle $\Delta\Omega_{eff}$ and $\Delta\Omega$ at the end of the capillary.

   $$I_g = \frac{\Delta\Omega_{eff}}{\Delta\Omega} \tag{2.31}$$

   As a consequence of the energy dependency of Θ_c, the gain factor also depends on the photon's energy and thus decreases with increasing energy ($I_g \propto \frac{1}{E^2}$).

   If a focusing effect is required, conically (Figure 2.29b) or elliptically shaped capillaries (Figure 2.29b) can be used. As illustrated conical capillaries have the disadvantage of a increased incidence angle.

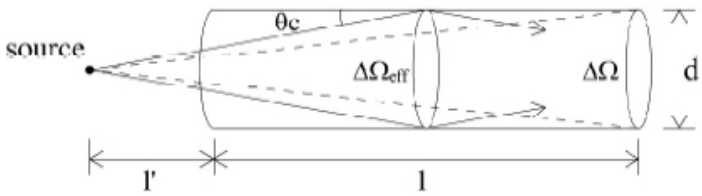

Figure 2.28: Derivation of the gainfactor by comparison with a pinhole collimator [10]

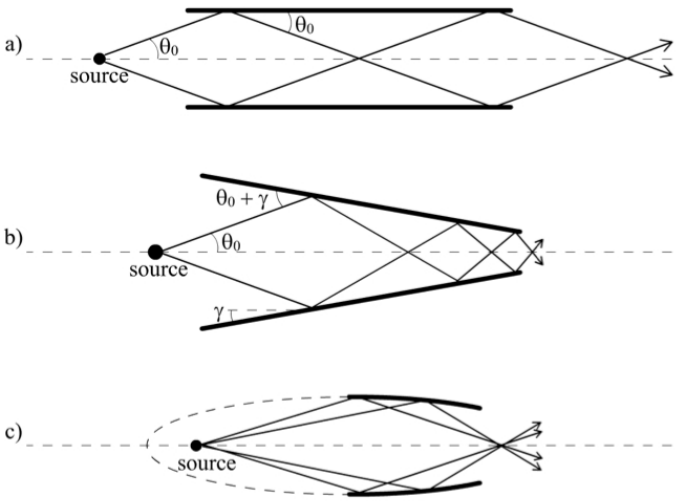

Figure 2.29: Various types of monocapillaries[19]

2. **Polycapillaries**
   Polycapillaries are clusters of a large number of monocapillaries (depending on the purpose 10 000 up to several millions) with diameters in the range of some μm (Figure 2.30). A bended shape allows various applications. Figure 2.31 shows the focusing and the collimating character of polycapillaries with an effectiveness far better than monocapillaries.

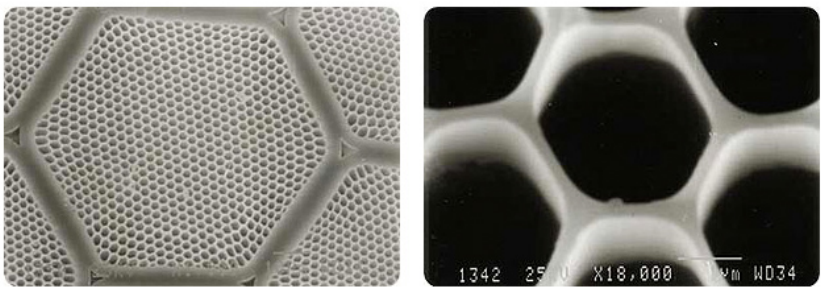

Figure 2.30: Electron microscope image of a polycapillaries' cross-section. The bar in the right picture corresponds to 1 μm. [21]

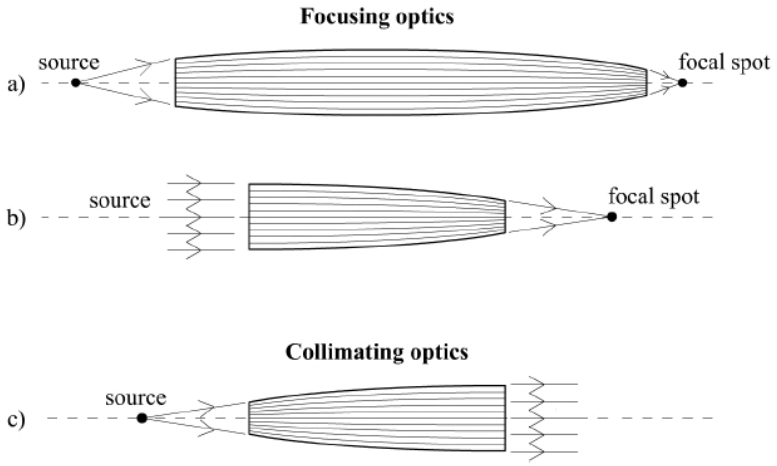

Figure 2.31: Point to point optics (a), simple focusing (b) and collimating optics (c) of a polycapillary [13]

2.6.3.2 X-ray lenses

Similar to optical lenses, collecting lenses for X-rays can be designed. According to the small refraction index $n < 1$ they show concave instead of convex character (Figure 2.32a). Beside the lens radius R, the focal length depends on the photon energy and the lens material (included in δ). This derives to 54 m for an Al lens assuming 14 keV radiation.
To reduce the focal length, more lenses are arranged sequently (compound refractive lense (CRL)). In the example above, with a sequence of 30 lenses, the focal length is reduced to an acceptable distance of 1.8 m following the formula in Figure 2.32b.

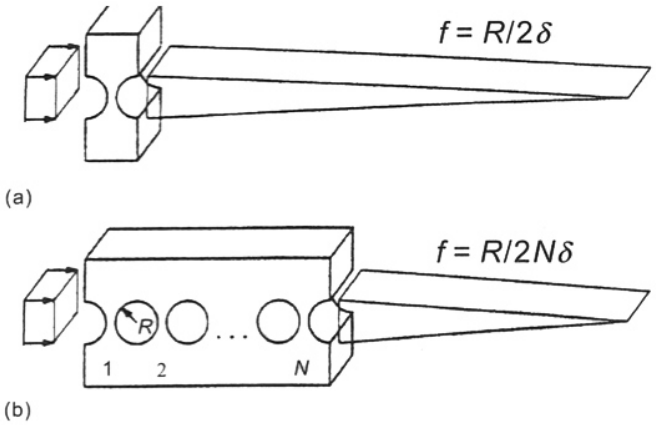

Figure 2.32: a: single lense, b: compound refractive lense used for X-ray focusing [19]

2.6.3.3 Monochromators

1. **Single crystal monochromator**
   A single crystal with a cubic structure is the simplest monochromator type. Figure 2.33 illustrates the principle of Bragg reflection. Constructive interference of the reflected beam is provided if the distance $\overline{AC} + \overline{CB}$ equals an integer factor of the wavelength λ. Therefore coherent superposition occurs. The result is an extremely sharp peak with a well-defined wavelength. Since α is the incidence angle in the figure, $\overline{AB} = \overline{AC} = sin(\alpha)$ describes half of the additional path. This leads to the basic Bragg-relation for constructive interference.

$$n \cdot \lambda = 2d \cdot sin(\alpha) \tag{2.32}$$

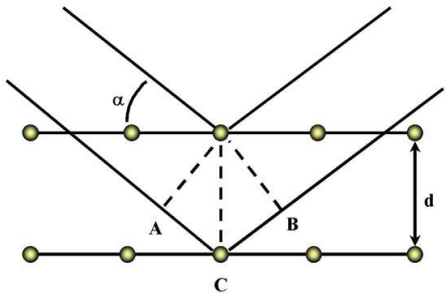

Figure 2.33: Derivation of the Bragg-equation[22]

Based on this principle, by tilting the crystal, α can be varied, and thus the reflected wavelength and the energy ($E = \frac{h \cdot c_0}{\lambda}$) can be changed. For small wavelengths such monocrystals face a comfortable method to select a desired wavelength of a "white" X-ray spectrum. On the other hand, the measurement of the α-dependency of the Bragg peaks with known primary radiation offers the ability to determine the type of the crystal lattice of an unknown sample.

2. **Multilayer monochromator**
   If a single crystal monochromation is used, a more and more grazing incidence is required with decreasing X-ray energy. If the wavelength of the desired radiation is much larger than the lattice constant, single crystals are not appropriate any longer. In this case multilayer monochromators offer new possibilities. Again the Bragg-relation is used to select a well-defined wavelength out of a spectrum, using a crystal consisting of multiple layers.
   Alternating thin (in the submicron range) layers of two materials with highly differing refraction indices are applied on a substrate material. Some often-used reflector-spacer pairs are Mo/Si, Rh/C or Ni/C. In the Bragg-equation 2.32 now d describes

the thickness of such a reflector-spacer layer. As illustrated in Figure 2.34 interference of all the reflected beam packets takes place, and thus constructive interference happens if the Bragg-equation is fulfilled.

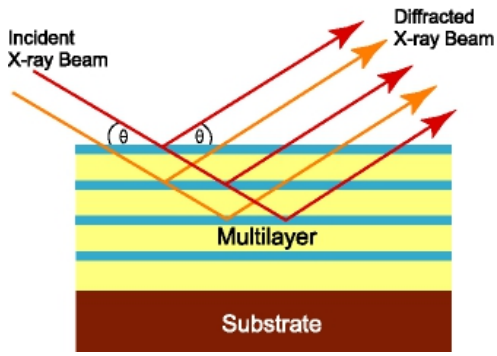

Figure 2.34: Illustration of a multilayer crystal [23]

The choice of the monochromator type depends on the required measurement conditions. A single crystal monochromator provides a sharp peak with low spectral bandwidth but with low photon flux, while a multilayer device in general assures higher photon flux combined with a broader spectral distribution.
In praxis a fixed-exit setup consisting of two monochromator crystals is often used to provide a constant beam position when the crystals are tilted.

Chapter 3

Physical Background of qBEI

3.1 Principle of a scanning electron microscope (SEM)

Contrary to the setup of a conventional light microscope where the whole sample is illuminated, a scanning electron microscope uses a focused electron beam to examine the sample step by step and line after line. Since electrons are charged particles, focusing techniques with electrostatic and magnetostatic fields are comfortable. In modern apertures the spot size can be reduced to a few nanometers. A moving sample stage combined with a precise x-y-z motor system allows the point after point analysis of the region of interest. Figure 3.1 shows a simplified illustration of a SEM. Various types of electron guns will be discussed in Chapter 3.4. Magnetic lenses (Chapter 3.5) and aperture plates are used to focus the beam. The interaction of the electrons with the specimen leads

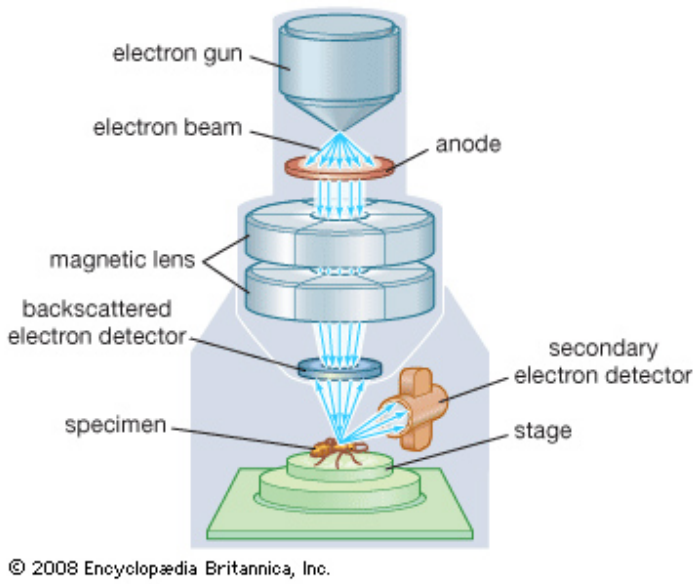

Figure 3.1: Schematic picture of a typical SEM, illustrating the path of the beam and a typical detector arrangement. [24]

to the emission of backscattered electrons and secondary electrons. As a consequence of the different emission energies, either a combined detector or two seperated detectors are used.
In principal the resolution of a SEM is determined by several parameters[25]:

- the beam diameter
- the size of the interaction volume of the beam with the specimen
- the stepsize between two adjacent pixels
- the counting statistics of the detected signal
- the beam damage on the sample
- the instrumental stability

Usually the sample chamber is evacuated to get rid of interactions between electrons and air molecules. Environmental scanning electron microscopes (ESEM) also allow measurements of wet samples.
According to the low penetration depth of electrons in matter, and thus to the raised surface sensitivity of the outgoing signals, sample preparation is an important factor. The dry samples must be coated with a thin layer of a conducting material, usually carbon or gold, to prohibit charging during the measurement procedure.

3.2 Interaction of electrons with matter

The interaction of an electrons with matter can be divided into two classes:

1. **Elastic scattering of the impacting electrons**
   The electron energy remains unchanged, but the trajectory is affected. Thus, depending on the depth and direction of the scattering, some of the beam electrons are able to escape the target. The flux of these electrons carries information about the average atomic weight of the target, they are called backscattered electrons (BE).

2. **Inelastic scattering of the impacting electrons**
   Several effects can lead to an alteration of the beam electrons' energy; namely the generation of secondary electrons (SEs) and Auger electrons, the emission of characteristic X-rays as well as the bremsstrahlung and a low energy cathodoluminescence radiation. Lattice vibrations and electron oscillations also lead to an energy transfer from the primary beam electron to the material of the specimen.

Figure 3.2 illustrates all common outgoing signals caused by electron bombardment.
The region below the surface of the specimen, where the deposition of the PE-energy

happens, is called interaction volume. It depends on the average atomic weight of the specimen and the energy of the PE (a homogenous structure is assumed). The understanding of the interaction volume is necessary for the experimental setup and for image interpretation.

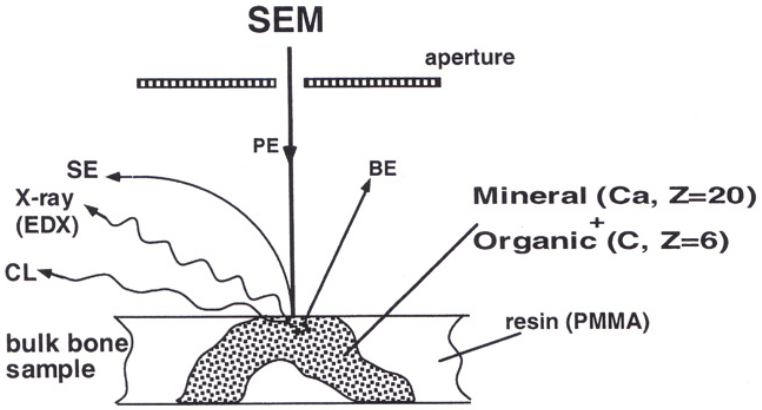

Figure 3.2: Overview of the fundamental interactions between the primary electrons (PE) with a typical energy from 10 to 30 keV and the bulk sample. In our case the bulk is bone (black dotted) embedded in polymethylmetacrylate resin (PMMA). Backscattered electrons (BE), secondary electrons (SE), X-rays measured with an energy dispersive X-ray detector (EDX) and the cathodluminiscece radiation are illustrated as arrows. [25]

A Monte Carlo simulation of an electron trajectory illustrates the electrons' trajectory through the bulk and visualizes the concept of the interaction volume (Figure 3.3)

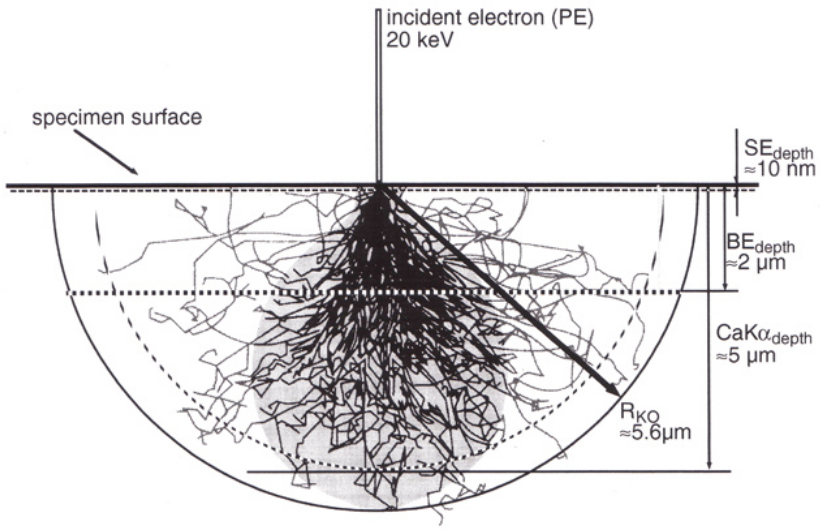

Figure 3.3: Monte Carlo simulation of the electron spread below the surface [25]

The simulation was done for a bone like material (low Z), assuming 20 keV PEs. Because of collisions with single atoms the trajectories become zigzag lines, especially deeper below the surface. Depending on the bulk material and the energy of the incident electrons the simulation leads to a spherical (high Z bulk) or to a pear like (low Z bulk) interaction volume in the specimen.

In Figure 3.3 various regions are labeled [25]:
gray area: interaction volume
R_{KO}: radius of the semi-spherical Kanaya-Okyama electron range
SE_{depth}: emission depth of secondary electrons
BE_{depth}: emission depth of backscattered electrons
$CaK\alpha_{depth}$: emission depth of the characteristic X-rays of the $Ca - K\alpha$ line textcolorred

The emission depth (similar to the information depth in Chapter 2.4) describes the depth of the sources of the emitted radiation and particles. It does not only depend on the penetration depth of the primary electrons, but due to absorption, the emission depth is also influenced by the type and the energy of the generated radiation.
According to the low energy of the SEs, their emission depth is extremely small, at the range of 10 nm. The elastically scattered BEs with 20 keV have the ability to escape from much deeper below the surface (typically 2 μm).
In Chapter 2.4 the information depth for $CaK\alpha$ radiation in hydroxyapatite was derived as $d_{99\%} = 71.5$ nm. In this case the $CaK\alpha$ depth mainly depends on the penetration depth of the primary electrons in the specimen with about 5.6 μm.

In the following chapters the elastic and the inelastic scattering will be discussed in a more detailed way. Data and principals in these chapters are taken from [12].

3.2.1 Elastic scattering (backscattered electrons)

If an electron beam impinges a specimen perpendicularly to the surface, a significant part of the primary electrons are not able to penetrate the sample deeper than a few nanometres. These electrons suffer elastic collisions and subsequently escape the target as BEs.
For example: 30% of beam electrons impinging a flat copper target perpendicularly suffer elastic scattering at the surface and thus get backscattered. 70% of the primary electrons penetrate the specimen and get scattered inelastically.
As with Monte Carlo simulations shown, BEs are mostly a result of multiple elastic scattering events involving angles less than 90°. So the cumulative effect of these events often results in an escape from the specimen. Only a few percentages of the impinging electrons suffer high-angle scattering events leading to an escape after a single collision.

The backscatter coefficient η describes the relation between primary beam electrons n_B and the backscattered electrons n_{BE}, which is equivalent to the current-relation $\frac{i_B}{i_{BE}}$.

$$\eta = \frac{n_{BS}}{n_B} = \frac{i_{BS}}{i_B} \tag{3.1}$$

η depends on sample probabilities such as composition (average atomic number), crystallography, internal magnetic fields, and surface topography as well as on experiment setup parameters like beam energy and tilt of the sample.

3.2.1.1 BE dependency on the atomic number

For our research the influence of the average atomic number on the BE signal can be used to determine the Ca concentration in bone tissue. To link the BE signal to the specimen composition in Figure 3.4, η is plotted as a function of the specimen's atomic number for various elements at a beam energy of 20 keV (Figure 3.4). It shows a positive correlation between atomic number and the backscatter coefficient. It should be noted that in the

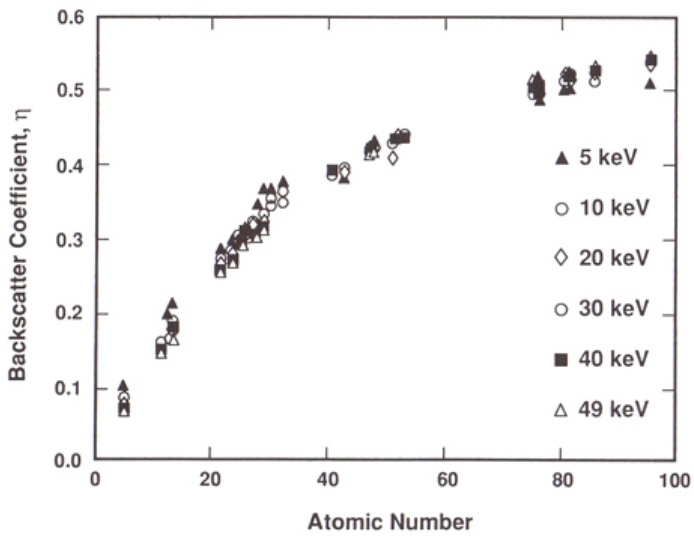

Figure 3.4: η as a function of the atomic number at various energies ranging from 5 keV to 49 keV [12]

low Z region (below $Z = 20$) the $Z - \eta$ relation can approximated by a linear function. Furthermore, in this part of the plot η is very sensitive to variations in Z. This allows a simple but appropriate calibration for materials with an average atomic number below $Z = 20$. Since bone and mineralized cartilage consist of organic matrix ($Z \approx 6$) and hydroxyapatite crystals ($Z = 13.86$), the adequacy of the linearization is guaranteed, and the atomic number contrast is at its best in this region. A target consisting of a mixture of elements can be described by the sum over the single element backscatter coefficients η_i weighted with its concentration c_i.

3.2.1.2 BE dependency on the beam energy

The result of the Monte Carlo simulation in Chapter 3.2 lets us assume an energy dependency of the backscatter coefficient η. Surprisingly the beam energy is hardly linked with η at usual energies. Despite of the change in the interaction volume at different energies the electron flux corresponding to elastic scattering normalized to the primary electron flux seems to remain nearly constant.

As shown in Figure 3.4 the range of the variations in η at different energies is less than 10% of the beam energy for a given Z. Furthermore, there is no trend to an increased or decreased η with rising primary electron energy from 5 keV to 49 keV
This behaviour can be qualitatively described as the result of two contrary effects. On the one hand the average penetration depth of the beam electrons inside the specimen increases at higher energies so that elastic scattering still takes place deeper inside the sample. But on the other hand the stopping power decreases with the higher energies and thus electrons with high energies are able to escape the specimen from deeper below the surface compared to low energy electrons. As a result of this inverse behaviour of range and stopping power the backscatter coefficient η becomes insensitive to variations in the primary electron energy.
At beam energies below 5 keV the situation becomes more complicated. As the beam energy is further reduced, η of the lighter elements apparently increases while the backscatter coefficient of the heavy elements seems to decrease.

3.2.1.3 BE dependency on tilt of the sample

Remembering the Monte Carlo simulation in Figure 3.3 it is obvious that changes in the tilt angle θ affect the BE yield. Experiments as well as simulations show a smooth monotonic increase in η while tilting the specimen from 0% to 90%. Arnal et al. [26] describe the backscatter coefficient as a function of Z and θ.

$$\eta(\theta) = \frac{1}{1 + \cos(\theta)^p} \quad \text{with} \quad p = \frac{9}{\sqrt{Z}} \tag{3.2}$$

At a perpendicular impinge of the beam most of the electrons penetrate the specimen deeply so that many low angle scatter events have to occur to the electrons to escape from the specimen. This situation changes when tilting the sample. With higher θ the electrons travel on trajectories near the surface and thus the probability of escaping the sample increases.

The monotonic dependency of the backscatter coefficient on the angle between beam and surface deliver topologic contrast and thus the ability to recognize the shape of the measured objects. Neverless, to display sharp edges and precise topological information the secondary electron signal is the first choice. Figure 3.6 compares BE and SE images of one source.

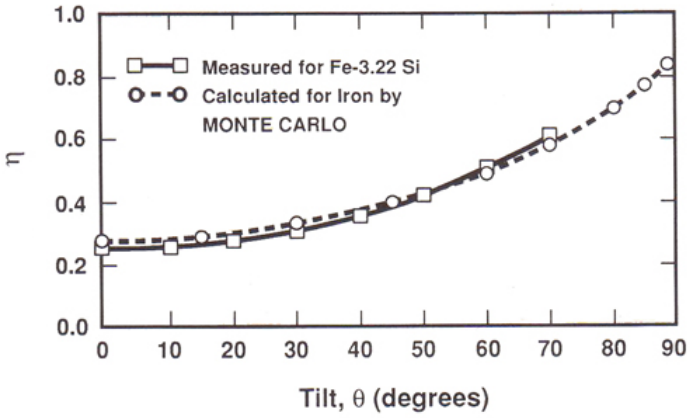

Figure 3.5: η as a function of θ comparing the results of experiments and Monte Carlo simulations for iron. [12]

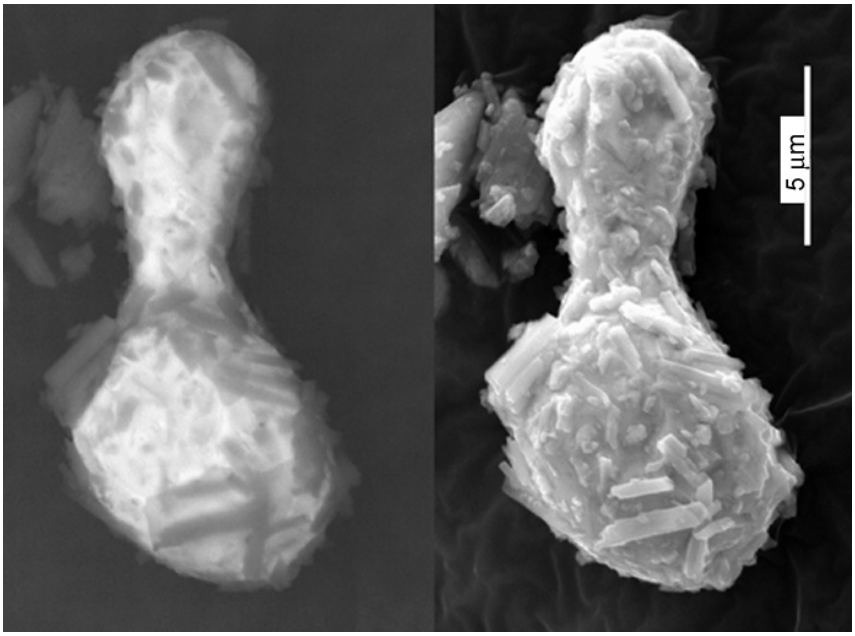

Figure 3.6: Comparison of BE image (left) and SE image (right) of a dust particle [27]

3.2.2 Inelastic scattering (secondary electrons)

The energy distribution (Figure 3.7) of electrons escaping the specimen is characterized by three regions. Region I (peak of BEs) and region II (low energy tail of BEs) depict the energy distribution of BE. Broadening of the backscatter-peak is caused by energy loss of the primary electrons in the sample according to inelastic scattering.

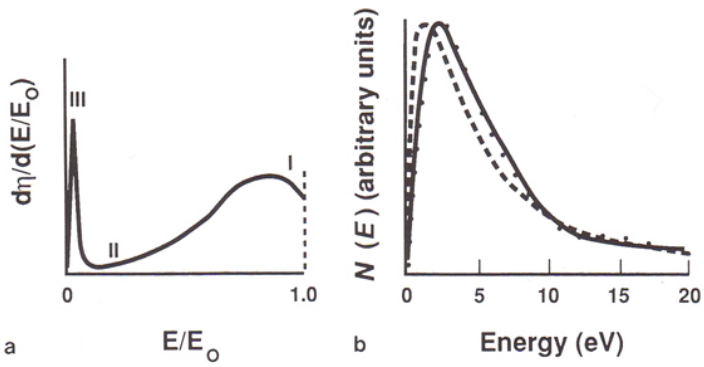

Figure 3.7: Energy distribution of electrons emmited by a target. (a) complete spectrum, (b) region of secundary electrons (regionII) expanded [12]

On the low energy side of the graph there is another, extremely sharp peak superimposing, the (in this region already marginal) BE signal (Region III).
This sharp and intense peak is caused by inelastically scattered electrons. Typical energies of SEs are $2-5\ eV$. They are a result of interactions between the primary electrons and weakly bound conductive-band electrons or outer shell valence electrons. The energy transfer of such an interaction is quite ineffective because of the high energy difference. Production of high energy SEs is improbable and thus most of the scattering occurs in the narrow low energy peak. By convention escaping electrons with energies less than 50 eV are counted as SEs corresponding to the fact that BEs with such low energies are rare. On the other side usually 90% of the SEs have energies less then 10 eV, so that SEs with more than 50 eV can be neglected in the BE statistics.

Similarly to the backscatter coefficient a secondary electron coefficient δ can be defined.

$$\delta = \frac{n_{SE}}{n_B} = \frac{i_{SE}}{i_B} \tag{3.3}$$

n_{SE} is the number of secondary electrons normalized by the number of impinging beam electrons n_B. This relation is similar to the secondary electron flux i_{SE} devided by the beam flux i_B.

3.2.2.1 SE dependency on atomic number and sample composition

In Chapter 3.2.1.1 the strong dependency of the backscatter coefficient on the atomic number was discussed. In Figure 3.8 this effect is compared with the secondary electron coefficient δ, the different characters of these two signals are obvious.
Except for some fluctuations δ stays constant for variations in atomic weight measured on pure element targets. Furthermore, the secondary electron yield is reduced compared with BE.

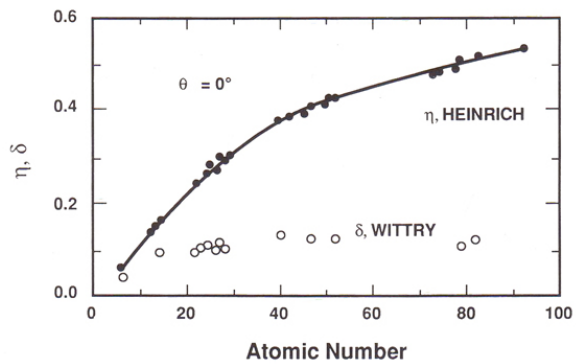

Figure 3.8: Comparison of measured η and δ values depending on the atomic number at perpendicular impinge [12]

Despite of these results there are atomic weight specific variations in the secondary electron yield, which cannot be observed in conventional SEMs. Because of their low energy SEs are extremely sensitive to surface contamination. In common electron microscopes with operating pressures ranging from 10^{-3} to 10^{-6} Pa. A deposition of sputtered matter or oil from the pump is unavoidable. These thin film contaminations prohibit undisturbed measurement of SEs because of their low energy. In 1983 Seiler showed a much more significant compositional δ dependence, using an ultra high vacuum chamber in combination with in situ surface cleaning. [28]

3.2.2.2 SE dependency on the beam energy

SEs have a low energy ranging from 2 eV to a maximum of 50 eV. Consequently the emission depth is reduced to a shallow region in the nanometer range below the surface. So it is plausible that increased beam energy, and thus increased penetration depth of primary electrons, leads to a dropping SE rate. SEs produced inside the sample are absorbed on their way through the specimen.
Figure 3.9 shows the behaviour of the total electron yield $\eta + \delta$ depending on the beam energy. $\eta + \delta$ is mainly influenced by changes in δ because of the low probability of BEs at these energies.
Reduction of the primary electron energy (below about 5 keV) leads to an increase of the total electron yield according to the raise of the number of inelastic scatter events near the surface. E_2 and E_1 denote the upper and the lower crossover point. Beam energies

between E_1 and E_2 lead to an outgoing electron flux higher than the flux of impinging electrons. The maximum is between the crossover points and depends on the analyzed material. On the low energy side of the maximum $\eta+\delta$ decreases with a decreasing beam energy. For most elements E_2 is below 5 keV, while E_1 is generally below 1 keV.

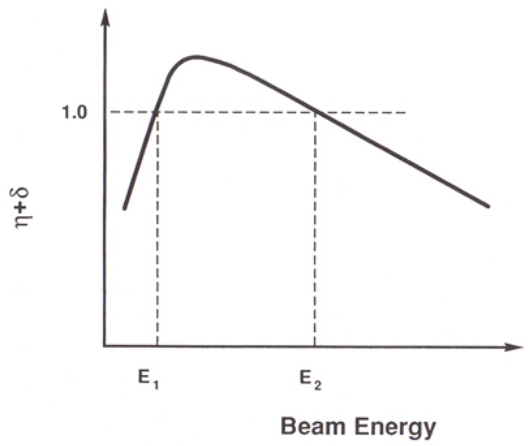

Figure 3.9: Energy dependency of the total electron yield $\eta + \delta$ [12]

3.2.2.3 Escape depth of SE

As discussed above, a consequence of the strong attenuation of low energy electrons in matter is, that the escape depth of the SEs is reduced to a shallow region below the surface. Formula 3.4 describes the probability p of SE-escaping from a depth z below the surface, suffering attenuation described by the mean free path λ.

$$p \propto e^{\frac{-z}{\lambda}} \tag{3.4}$$

The maximum escape depth for SEs is about 5λ and reaches from 5 nm in metals up to 50 nm in insulators. The increased attenuation in metals can be explained by scattering with conducting band electrons. Calculations confirm the abrupt drop off of escaping probability on the surface of the sample[29]. In general the SE escape depth can be estimated to 1/100 of the BE escape depth. Figure 3.10 shows a SE image of a human vertebra. Because of the surface sensitivity of the SE signal, edges are sharp and show a good contrast.

Surprisingly there is a non negligible cumulative effect of BEs and SEs. As a result there are SEs carrying information from deep below the surface. Figure 3.11 illustrates this effect and separates the SE yield in two contributions, SE_I and SE_{II}.

The SE_I signal is produced by the 5λ thick layer below the surface, immediately after impinging of the beam. Obviously these electrons, linked with the secondary electron coefficient δ_I in, are only influenced by the specimen matrix in this shallow region just below the surface and thus result in a signal with high lateral resolution.

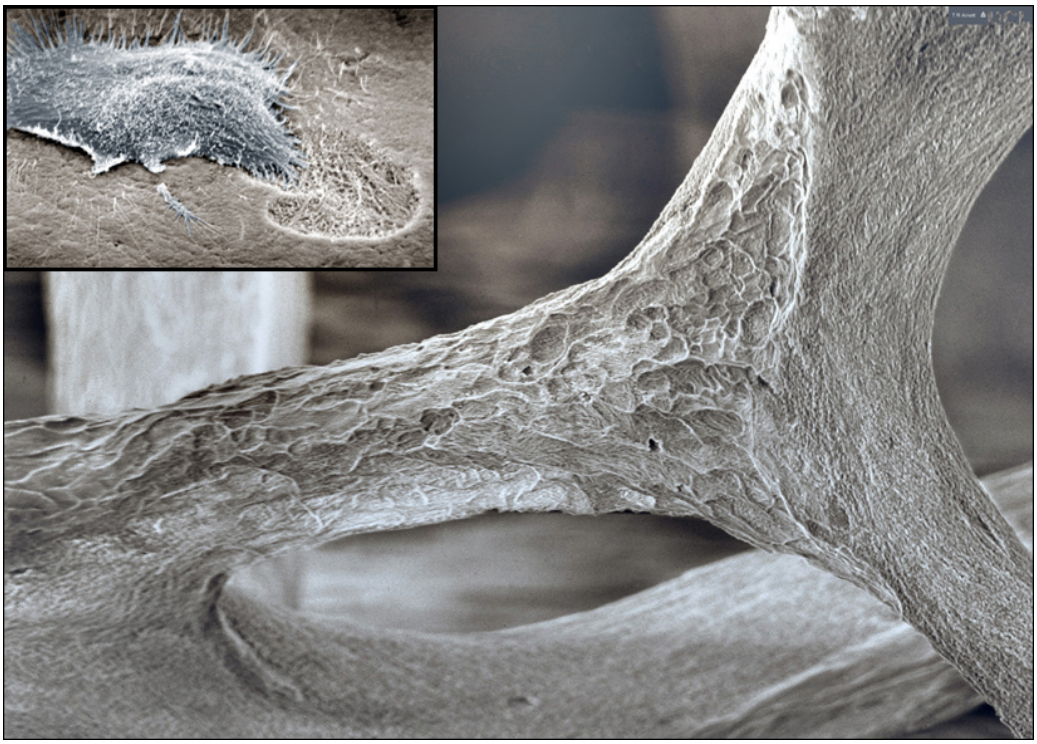

Figure 3.10: Secondary electron image of the 3rd lumbar vertebra of a 71 year old woman. The insert shows a osteoclast, resorbing bone tissue. [30](modified)

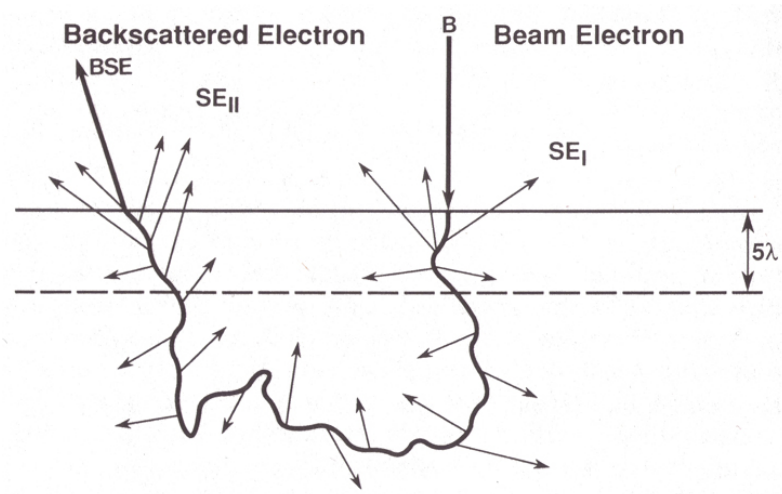

Figure 3.11: Illustration of the separation of the outgoing eletctrion signal into SE_I,SE_{II},BSE [25]

The situation changes for the SE_{II} electrons with the secondary electron coefficient δ_{II}. Again the source of the SEs is in the 5λ layer below the surface, but this time the SE emission is induced by primary electrons backscattered deeper below the surface. There are two reasons why BEs are more effective in the SE production. First the perpendicular impinge of the beam allows to overcome the near surface region for SE emission quickly and thus there is a minimum of SE production. Contrarily BEs enter the 5λ region in a random angle. Shallower angles result in a longer path in the region of probable SE escaping and thus in a raised SE signal.
The second reason for the higher BE efficiency in SE production is caused by the energy loss of the primary electron while travelling through the specimen. In Chapter 3.2.2 we concluded that at usual beam energy the SE yield increases with a decreasing primary electron energy. This effect in combination with the shallower angles of BEs when escaping the sample leads to $\delta_I < \delta_{II}$. The ratio $\frac{\delta_{II}}{\delta_I}$ is in the order 3-4.

The cumulative effect of SE_I and SE_{II} electrons can be summarized in δ_T, the total secondary electron coefficient. Of course δ_{II} has to be weighted with η, the backscatter coefficient.

$$\delta_T = \delta_1 + \delta_{II}\eta \tag{3.5}$$

Since δ_I and δ_{II} and η strongly depend on the material, also the contribution of SE_I and SE_{II} on the total electron yield changes for different specimens.
Table 3.1 shows δ_T ,η and $\frac{SE_II}{SE_I}$ for different elements. Generally it can be said, that the contribution of SE_{II} increases with the increase of Z because of a raised backscatter coefficient η.

	δ_T	η	$\frac{SE_{II}}{SE_I}$
Carbon	0.05	0.06	0.18
Aluminium	0.1	0.16	0.48
Copper	0.1	0.30	0.9
Gold	0.2	0.50	1.5

Table 3.1: Comparison of total SE yield δ_T, the BE yield η and $\frac{SE_{II}}{SE_I}$ of C, Al, Cu and Au

As discussed above, based on the raised SE yield at shallower angles, the change in δ when tilting the sample is understandable. Again the path through the 5λ thick region just below the surface raises with the tilt angle θ. Geometrical considerations lead to Formula 3.6.

$$\delta(\theta) = \delta_0 \frac{1}{cos(\theta)} \tag{3.6}$$

3.2.3 Occurrence of X-rays

There are two fundamentally different processes leading to the emission of X-rays while the sample is irradiated with electrons.

1. **Emission of bremsstrahlung - continuous X-ray spectrum**
   As discussed in Chapter 2.2.1, decelerated electrons emit non quantized radiation. The process is the same, no matter if fast electrons are produced inside the sample caused by interaction with primary X-rays, or by (like in this case) extern electron bombardment. Like in X-ray induced bremsstrahlung the random character of the deceleration process leads to a continuous radiation.

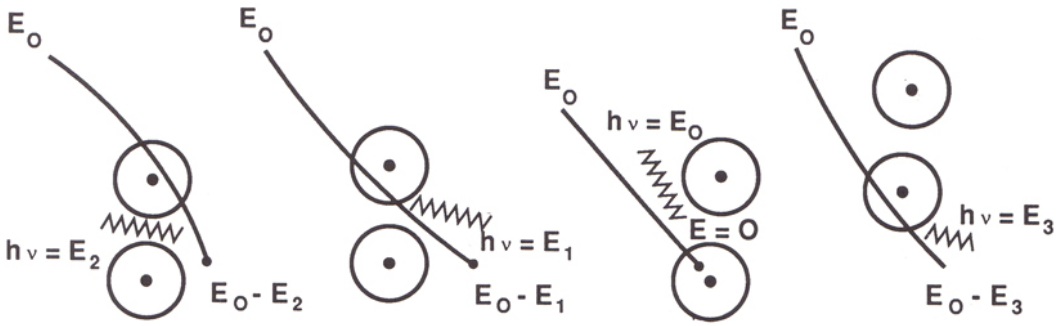

Figure 3.12: Deceleration and deflection of electrons resulting in the bremsstrahlung-continuum. [12]

   Figure 3.13d shows a typical copper X-ray spectrum. The diverse characters of the continuous contribution (thick line) and the characteristic radiation (arrows) are obvious.

   In 1923 Kramers suggested an approximation for the intensity distribution [31]:

$$I_{cm} \approx \frac{i\bar{Z}(E_0 - E_\nu)}{E_\nu} \tag{3.7}$$

   with the beam current I, the average atomic number of the target $\bar{Z}$, the electron energy E_0 and the photon energy $E_\nu = h \cdot \nu$. $E_\nu = E_0$ corresponds to a single deceleration process were all the kinetic energy of an electron is transferred to the photon.
   In contrast to the X-ray induced bremsstrahlung in Chapter 2.2.1 the origin of the secondary radiation is now in the range of one μm below the surface.

2. **Emission of characteristic X-rays and Auger electrons**
   Chapter 2.2.2 described the occurrence of characteristic radiation after X-ray induced inner shell ionization of the target atoms. As mentioned before this effect also can be induced by impinging electrons. Further processes are similar to those in

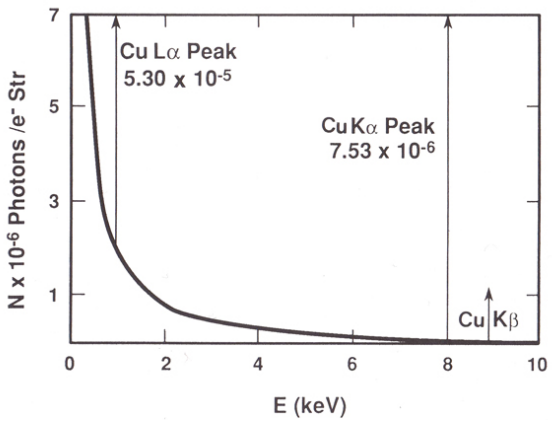

Figure 3.13: X-ray spectrum of a copper target generated by a 20 keV electron beam [12]

Chapter 2.3.1: the excited ion relaxes to the ground-state within about 1 ps causing either the emission of a series of characteristic fluorescence photons or Auger electrons. Figure 3.14 illustrates these processes, the competing character of fluorescent photon emission, and the Auger effect. For further explanation of the characteristic line intensities see Chapter 2.2.2; the transition nomenclature is described in Chapter 2.1. In Chapter 2.3.1 the Auger process is explained in more detail.

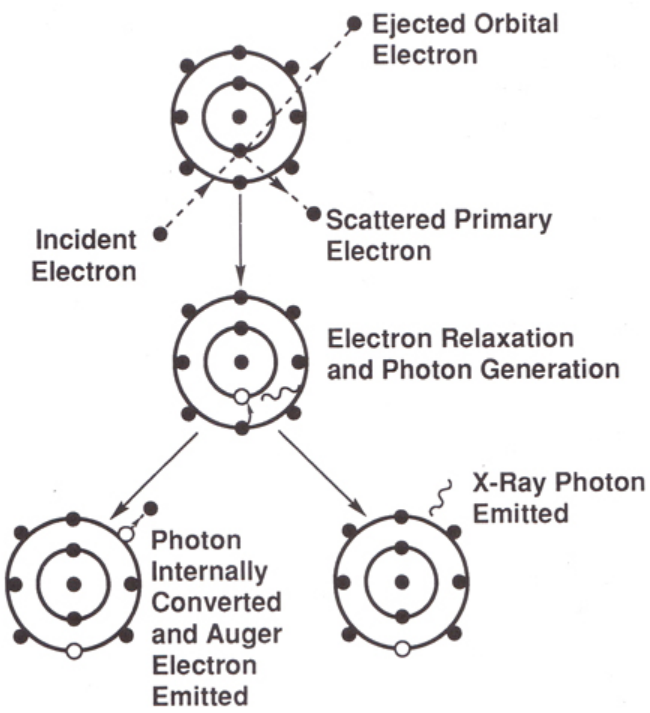

Figure 3.14: An incidence electron causes inner-shell ionization followed by X-ray emission or emission of an Auger electron. [12]

3.3 Electrons in electrostatic and magnetostatic fields

Charged particles like electrons interact with electrostatic and magnetostatic fields, resulting in a change of velocity. This can be used to focus or to collimate electron beams, to channel them and for energy dispersive analyses. The Lorentz force $\vec{F}$ describes the fundamental influence of an electrostatic and magnetostatic field on charged particles.

$$\vec{F} = q(\vec{E} + \vec{v} \times \vec{B}) = q\,\vec{v} \times \vec{B} \tag{3.8}$$

with the electric field $\vec{E}$, the particles velocity $\vec{v}$, and the magnetic field $\vec{B}$. The charge q of the particle equals $-e$, in case of electrons. Note the vector character of $\vec{E}$, $\vec{v}$, and $\vec{B}$. The first expression in Formula 3.8 describes an acceleration of the particle parallel to the electric field (or antiparallel depending on the sign of the charge) while the second expression is linked to the magnetic field. The result of the vector product of $q\,\vec{v} \times \vec{B}$ is a force vector perpendicular to $\vec{v}$ and to $\vec{B}$. The length of this vector equals the strength of the force. In Figure 3.15 the simple case of homogeneous magnetic field without electrostatic component is illustrated. The constant force perpendicular to the velocity vector leads to a circular movement of the electron.

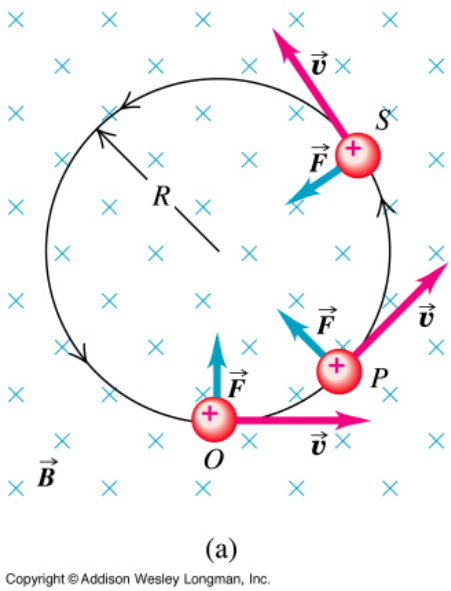

Figure 3.15: Movement of electrons in a homogeneous B-Field [32]

An additional electric component of the field parallel to the magnetic component causes a spiral movement showed in Figure 3.16

With a combination of homogeneous and inhomogeneous fields it is possible to design the electron beam in a desired way. In Chapter 3.5 and Chapter 3.6 the importance of this process becomes evident.

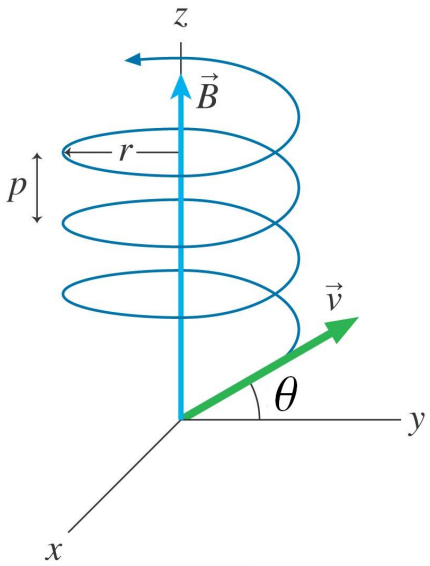

Figure 3.16: Electron track in a homogenous B-field combined with an electric field orientated in z-direction [33]

3.4 Electron guns

Basically, there are three common types of electron sources with various methods to overcome the work-function energy-barrier of a cathode material. The simplest one is a heated tungsten hairpin. The more expensive LaB_6 and field emission cathodes provide higher brightness. Figure 3.17 shows the diverse design of these three cathode types. Parameters like brightness, lifetime, energy spread, current stability and required low pressure, define the appropriate cathode for a specific application. Most of the data and principles in this chapter are taken from [12].

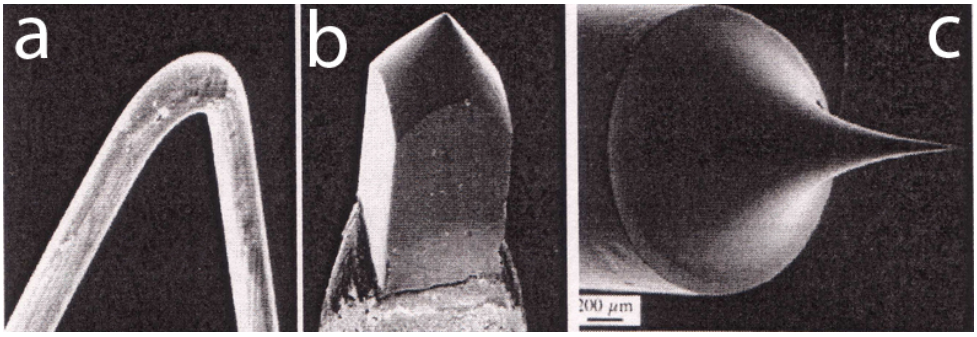

Figure 3.17: (a) Tungsten filament, (b) LaB_6 crystal, (c) Field emission cathode[34]

Table 3.18 summarizes the most important properties of common cathode types.

Source	Brightness	Lifetime	Source size	Energy spread ΔE	Beam current Stability
Tungsten hairpin	10^5 A/cm^{2}sr	40–100 h	30–100 μm	1–3 eV	1%
LaB_6	10^6	200–1000	5–50 μm	1–2	1%
Field Emission					
Cold	10^8	>1000	<5 nm	0.3	5%
Thermal	10^8	>1000	<5 nm	1	5%
Schottky	10^8	>1000	15–30 nm	0.3–1.0	2%

Figure 3.18: Table with the significant parameters of various cathode types [12](modified)

In our experimental setup a Tungsten hairpin electron sources is used. Therefore this cathode type is described more detailed.
V-shaped tungsten filaments have been used as cathodes for 60 years, and therefore they face a well-prooved method of electron beam production. As shown in Figure 3.17a tungsten wire of about 100 μm is bent in a 100 μm radius. To overcome the work-function energy-barrier the wire is heated up by the filament current (about 3 A) to about 2700 K. According to the quality of the vacuum, the cathodes' lifetime varies from 30 to 100 hours. A vacuum of at least 10^{-3} Pa must be achieved. In Figure 3.19 the schematic setup is shown: the Wehnelt cylinder is kept on -500 V relative to the filament to focus the emitted electrons, and therefore to optimize the brightness, while a high voltage of typically 30 keV accelerates the electrons towards the anode. A disadvantage of the

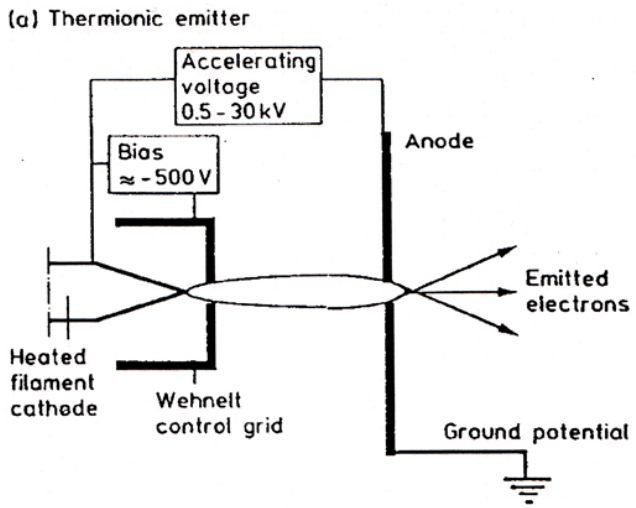

Figure 3.19: Schema of a tungsten filament setup[34]

tungsten filament cathode is the relatively large spot of the electron emission at the range of 30 to 100 μm. To achieve a small spotsize on the sample (and thus a good resolution)

additional electron optics are necessary. ΔE, the energy variation of the emitted electrons is in the order of eV, and must be considered for low voltage SEM operation.

3.5 Electron lenses

Electron lenses are primarily used to focus the electron beam. Therefore electromagnetic lenses are installed in microscopes, using the Lorentz force (Chapter 3.3) to deflect the electrons to a spiral trajectory and thus to a focal spot. Strong magnetic fields are essential to achieve acceptable focal lengths. Figure 3.20 shows a simple lens which can be compared to an optical collecting lens. For practical use often short focal lengths and therefore higher field strengths are required. A magnet design with an iron pole-piece amplifies the field strength by lowering the volume of magnetic force. Figure 3.21a shows the cross section of the lense in Figure 3.20, the dots denote the coil windings. Figure 3.21b shows the pole piece modification. The iron cover gets magnetized and therefore the magnetic field lines are bundled.

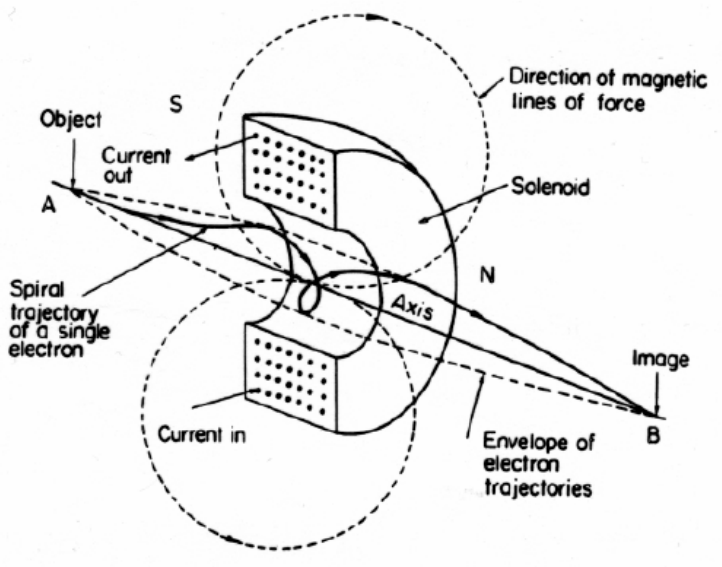

Figure 3.20: Deflection of an electron when passing a simple ring-shaped lens[35]

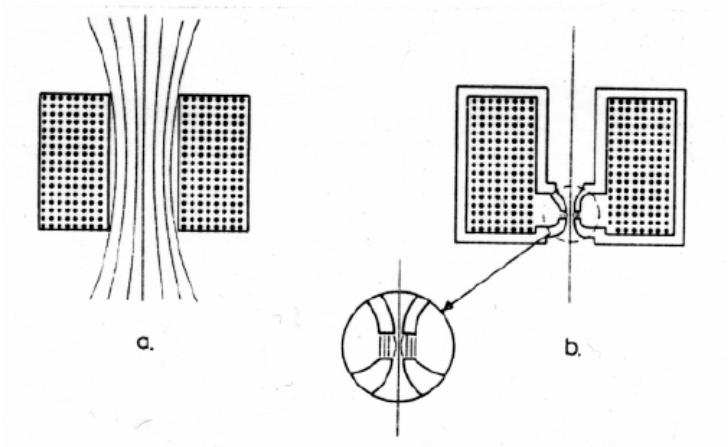

Figure 3.21: Cross section of an electron lense without (a) and with (b) pole piece[35]

Multipole lenses (in exact, quadrupole, sextupole, and oktupole lenses) are an alternative technique. A quadrupole lens is illustrated in Figure 3.22 and shows an either horizontal or vertical focusing character, while defocusing occurs in the other direction. Consequently the circular cross-section of an electron beam is transformed to an elliptical shape. To achive a small circular focal spot, at least a quadruple-triplet is necessary. Unfortunately all quadrupole lenses show lens aberration errors, well known from light optics. To correct them sextupole and octupole lenses are needed.

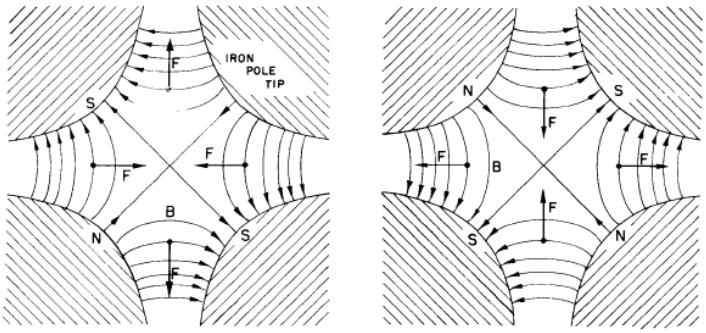

Figure 3.22: Resultig force of a charged particle in a quadrupole lense [36]

3.6 Electron detectors

Depending on the mode of electron microscope operation, there are various types of electron detectors. The most common one is the Everhart - Thornley setup, either with negative or positive bias. If only backscattered electrons should be measured also scintillator detectors or BSE-to-SE conversion detectors come into consideration. Beside these detector types, solid state diode detectors are an alternative. The principles as well as a further explanation of the previously mentioned detectors can be found in [12].

3.6.1 Everhart - Thornley (E-T) detectors

The E-T detector is a combined backscatter-secondary-electron detection device, based on the combination of faraday cage, a scintillator crystal, and a photomultiplier. The setup is shown in Figure 3.23.

In an E-T detector electrons cause photon emissions in a scintillator layer covering a fiber

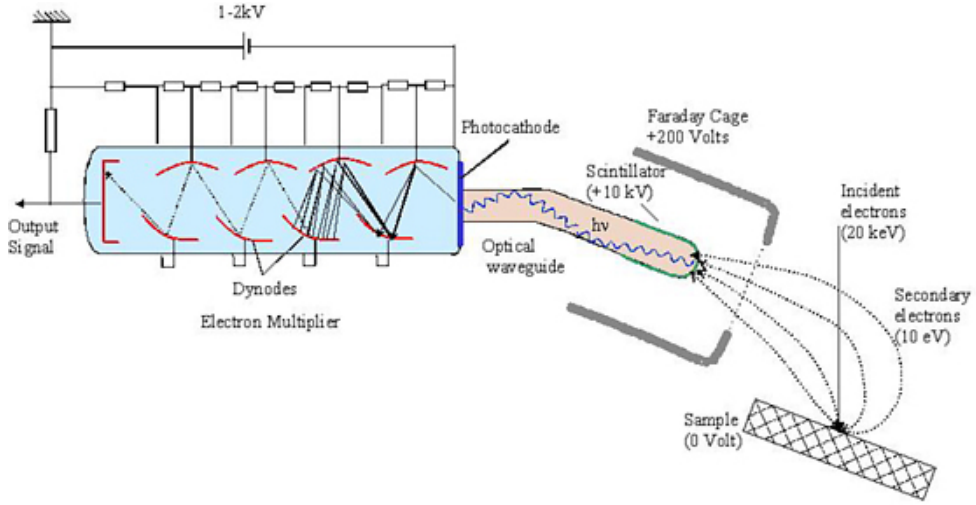

Figure 3.23: A E-T device acting as a (mostly) secondary electron detector in the positive bias mode. [37]

optic, which guides the light signal to a photocathode where the photon is re-converted to an electron by the photoelectric effect. Inside a photomultiplier the electron signal gets amplified successively resulting in a processable electron current of 10^6 to 10^7 electrons. Energies in the range of 10 keV are necessary to excite the scintillator crystal. Hence, for detection of the low energy SEs, additional acceleration has to be provided by a high voltage. To prohibit deflection of the primary electron beam, the high voltage ($10 - 20$ keV) is applied relatively to a faraday cage. The potential relative to the sample is held on $+200$ V to collect the SEs (positive bias mode). Depending on the surface structure, nearly all secondary electrons are measured. BEs with typical energies of 20 keV are not effected by the collecting voltage according to their high energy, but still some of them reach the detector directly, causing a lower but significant signal.

A pure BE detection can be archived by simply changing the $+200$ V to -50 V, then all SEs are reflected while BEs sill excite the scintillator (negative bias mode).

3.6.2 Scintillator backscatter electron detectors

The disadvantage of a E-T device in the negative bias mode is the relatively low solid angle for BE detection, and therefore a low countrate. Scintillator detectors are designed differently, providing a better BE yield.

With primary beam energies of 20 keV and more, the majority of the BEs have enough energy to excite a scintillator without additional acceleration. Without a bias SEs are not measured, and deflection of the primary electrons do not have to be considered. Hence the

detector can be placed near the beam and close to the sample. A very effective alignment of a material acting as scintillator and light-guide is shown in Figure 3.24. A detecting pipe with a hole permits beam transition to the sample covering a large solid angle. Again the photon is guided to a photomultiplier for signal conversion and amplification.

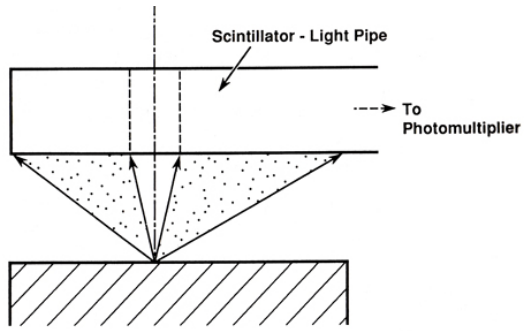

Figure 3.24: A scintillator-light-pipe acts as detector with large solid angle for BE. [12]

3.6.3 BE-to-SE conversion detectors

This type of a BE detector is illustrated in Figure 3.25. A negatively biased grid ($-50\ eV$) covering the sample blocks the SEs. High energy BEs pass the grid without significant loss of intensity and hit a converter target such as a MgO layer placed around the primary beam. SEs produced this way, together with those emitted from the chamber walls after the BE impact, are measured with an E-T detector described in chapter 3.6.1.

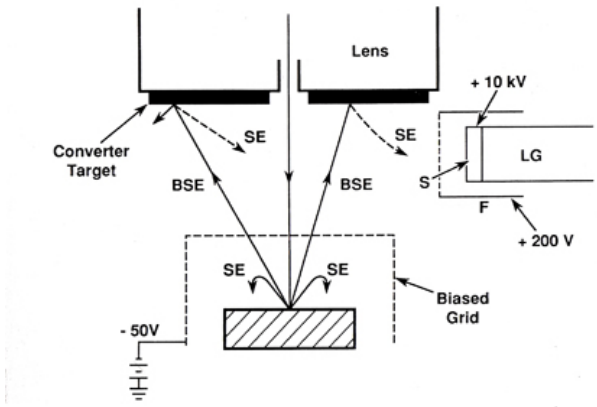

Figure 3.25: Illustration of a BE-to-SE conversion detector; the negative bias prohibits the measurement of SEs produced at the sample surface. [12]

3.6.4 Solid state diode detectors

This detector type is sensitive to BEs, but also SEs and X-rays produce a low signal. It is based on a reverse biased diode (previously described in Chapter 2.6.2). Similar to the semiconductor X-ray detectors, impinging electrons cause electron-hole pairs in the sensitive volume. The bias separates the charges resulting in a measureable current (Figure 3.26). In the case of a Si-diode (assuming 3.6 eV for electron-hole production) a single BE produces more than 3000 electron hole pairs. A thin Al layer covers the surface providing electrical conduction. Since the measured current is proportional to the electron energy, the SEs only contribute for a small part of the signal. Electron induced X-rays also produce electron-hole pairs in the diode, but again compared to the large number of high energy BEs they only lead to a minor current. Solid-state detectors are executed as thin (few mm) plates. Therefore they can be used to cover a large solid angle and are usually mounted like the BE-to-SE converter target in Figure 3.25.

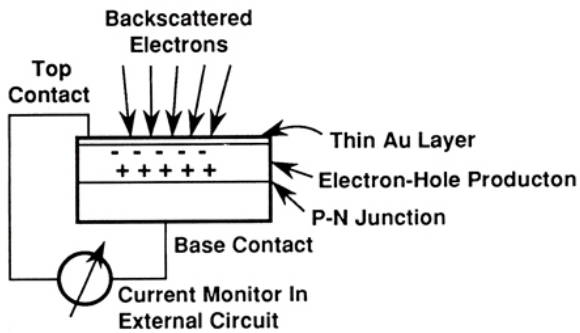

Figure 3.26: Principle of a solid state detector[12]

Chapter 4

Characteristics of Bone and Cartilage

4.1 Hierarchical structure and architecture

Bone is a complex nano composite material, consisting of brittle and stiff crystalline particles (mainly calcium-hydroxyapatite crystals $Ca_{10}(PO_4)_6(OH)_2$) and tough proteins with low stiffness. This combination accounts for unique mechanical properties such as a high fracture energy [38]. Figure 4.1 shows a stiffness - toughness diagram, illustrating the mechanical properties of various biological tissues, including pure protein, calcite and bone.

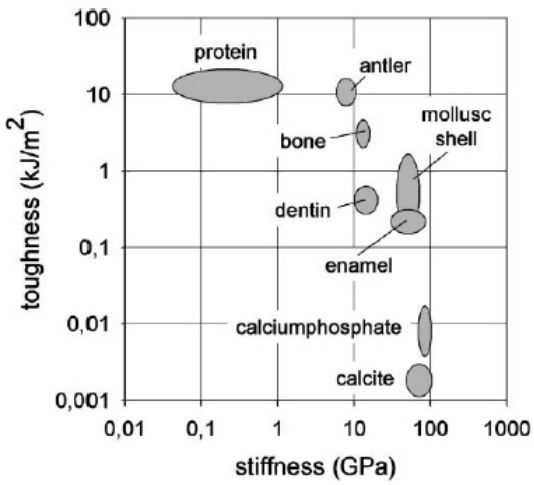

Figure 4.1: Toughness versus stiffness of various materials. Bone combines the advantageous properties of stiff calcium crystals and tough proteins. [38]

The arrangement of apatite and proteins in the submicron level is illustrated in Figure 4.2. Long collagen molecules with a thickness of $2 - 4$ nm are aligned parallelly and well-ordered.
This collagenstrings are reinforced by calcium-hydroxyapatite crystals, building a collagen - mineral compound. Adjacent strings are staggered relatively to their neighbors; the shift it is about 67 nm [38]. A bundle of these long compounds builds the collagen

fibril with approximately 100 *nm* thickness. If stress is applied in longitudinal direction, the combination of the ductile collagen molecules and the stiff calcium crystals results in beneficial (stiff and tough) mechanical properties. To resist shear forces, divalent and trivalent crosslinks are formed within adjacent collagen molecules and within fibrils to stabilize the matrix. Superior to this sub-micron structure, the inner bone architecture

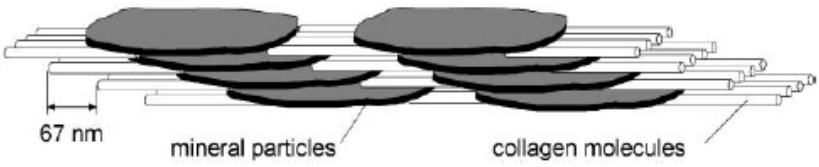

Figure 4.2: Illustration of the mineral-collagen composite, forming a fibril[38]

shows a combination of compact and of spongy matrix. Depending on the bone site, for example a femur shows at the midshaft region compact cortical bone with a porosity of only 6%, generated by chanals of the haversian system (osteons). However, at the metaphysis the bone marrow is filled with spongy bone(about 80% porosity).

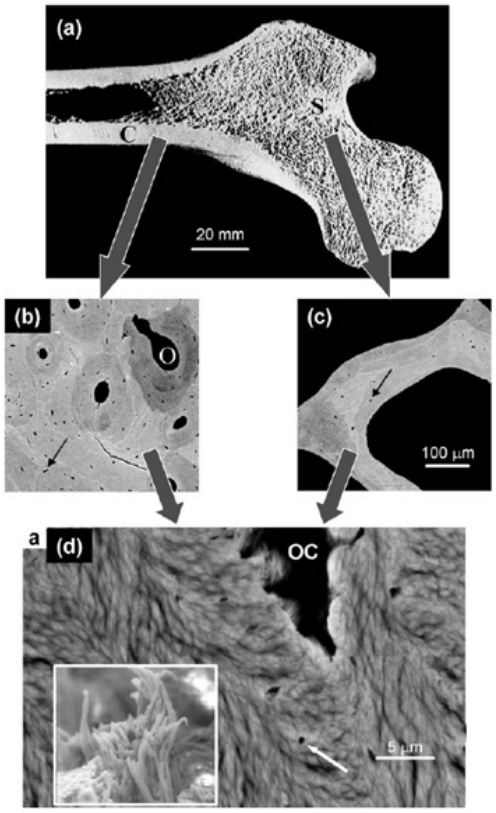

Figure 4.3: BE images of cortical (b) and spongiosa (c) of a femoral head. (d) shows the fibrillar texture near an osteocyte lacuna (OC) formed by bundles of mineralized collagen fibrils (insert). [38]

As Figure 4.3a shows, near the femoral head regions of spongy bone (called spongiosa) and regions of compact bone (corticalis) can be distinguished. The figure also clarifies the hierarchical structure. Figure 4.3b shows an enlarged cross-section of the cortical region with the Haversian canals (black cavities) with blood vessels inside. In Figure 4.3c the spongiosa with trabecular architecture can be seen. A secondary electron image of such a trabecel was shown previously in 3.10. Further magnification leads to Figure 4.3d. The OC labeled region is a osteocyte-lacuna, where the osteocyte lives. These cells are differentiated osteoblasts (final stadium), which were entraped in the matrix during bone formation.

Figure 4.3 shows BE images and thus only the high Z tissue is visible. Therefore blood vessels, cells and other non-calcified tissue are displayed black. Beside Ca, there are only high Z elements in trace element-concentration. According to the findings about the Z dependency of the BE yield in Chapter 3.2.1.1, the brightness in the BE image corresponds to the calcium content. A calibration with reference standards allows the quantification of weight percent calcium in bone, and thus leads to the concept of quantitative backscattered electron imaging (qBEI) [39].

4.2 Mechanism of bone turnover

The complexity of the bone matrix is not only related to its architecture, composition, and submicron-organization, but also to its dynamics. Since there is permanent bone remodeling, bone is a highly dynamic and adaptable tissue. Bone forming cells (osteoblasts) are opposed by the cells of bone resorption (osteoclasts). Osteoclasts act particularly randomly when dissolving collagen and calcium-hydroxyapatite, but they are also assumed to resorb damaged bone selectively [40]. After this, the resorption lacuna is cleaned up by mononuclear cells (most probably by lining cells), and a cement layer, consisting of non collagen proteins is layed down. Afterwards osteoblasts form the osteoid - a preliminary phase as fundament for the calcification process. Depending on the ratio of resorbed and newly formed bone the balance can be neutral, negative, or positve.

In [40] the five phases the bone remodeling cycle are listed:

1. **Resting**
   During the resting phase neither bone resorption nor formation takes place.
2. **Activation**
   Mechanical stress, "sensed" by the osteocytes, leads to activation of the osteoclasts and therefore to differentiation into multinucleated cells. Systemic hormones like parathyroid hormone (PTH) and vitamin D are also stimulating factors.
3. **Resorption**
   Irregulary shaped cavities (like the eroded surface in Figure 3.10) are the result of osteoclastic bone resorption (insert in Figure 3.10). They are called Howship's lacunae or resorption pits.

4. **Reversal**
   Osteoclasts suffer a programmed cell death (apotosis) leaving a thin proteoglycan layer on the surface. Later this thin interface will be called cement line.

5. **Formation**
   The osteoid - an unmineralized layer of collagen is placed in the resorbing pit by the osteoblasts. The following mineralization process happens in two phases. Primary mineralization starts about 10 days after osteoid deposition as a rapid process. Within a few days 70% of the complete Ca is accumulated. In this phase the Ca fraction in the matrix reaches about 18 weight-percent ($wt\%$) [40]. During this phase osteoblasts can be encased; they become osteocytes still connected to the surrounding tissues by a large number of nano-canals, called canaliculi. The phase of secondary mineralization can be understood as a slow maturation process of the tissue according to the growth of the calcium-hydroxyapatite crystals. Usually, the Ca concentration goes into saturation at 23 or 24 $wt\%$. Figure 4.4 illustrates the involved cells.

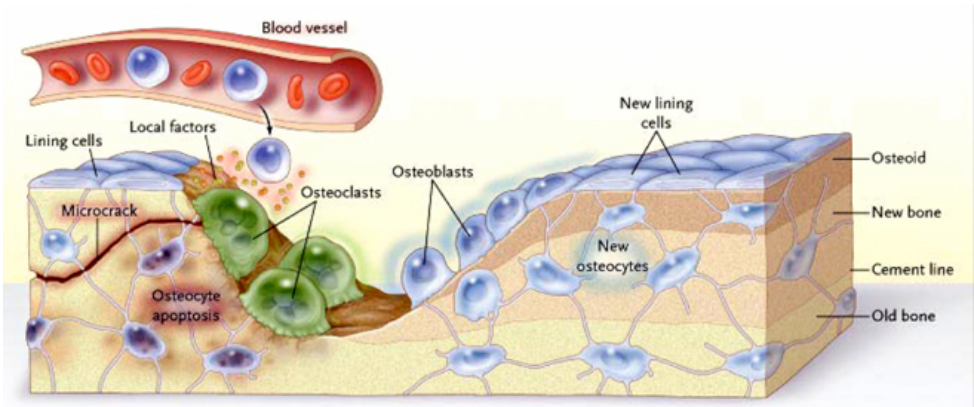

Figure 4.4: Interplay of osteoblasts and osteoclasts during bone remodeling. [41]

As a result of the gradually remodeling of the matrix, bone consists of bone packets with different age, and thus with various calcium content. They are separated by cement lines, which particularly show a raised Ca concentration.

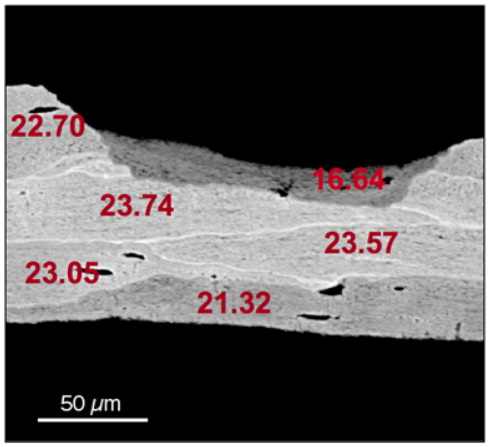

Figure 4.5: qBEI image of a spongiosa trabecel. The red values denote the calcium content in wt%. [41]

Due to the complexity of the system, bone diseases can be caused and influenced by a large number of parameters. Beside genetic factors the diet, physical activities as well as exposure to various substances or medical treatment (like cortison[42]) belong to risk factors for bone diseases. Obvious, abnormalities in the bone remodeling process cause alterations in the bone mineral density distribution (BMDD). Since qBEI is an excellent method to determine the BMDD it can be used for diagnostic purposes.

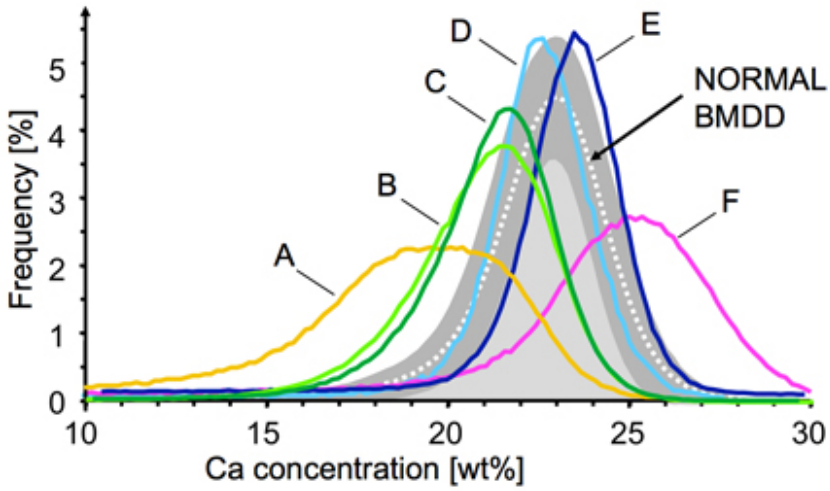

Figure 4.6: BMDD of various bone disease including two types of osteoporosis.
A: osteomalacia, B: idiopathic osteoporosis,
C: postmenopausal osteoporosis (pmpOP),
D: pmpOP after bisphosphonat treatment, E: osteogenesis imperfecta,
F: pmpOP after natriumfluorid treatment
(modified from[41])

Figure 4.6 shows BMDD histograms of various bone diseases. The Ca concentration on

the X-axis is measured by qBEI while the Y-axis represents the frequency of occurrence of a given Ca content. The postmenopausal and the idiopathic osteoporosis cause a shift to the left in the diagram. This can be interpreted as a result of increased bone turnover (more younger low-mineralized bone tissue) [43].

4.3 Characteristics of articular cartilage

Articular cartilage (in the case of our study at hip heads or patellas) can be divided into the mineralized cartilage (mCAR) and the non-mineralized (or hyaline) cartilage (nmCAR), the latter is the interface region to the joint. In contrast to bone, calcified cartilage does not show a lamellar structure and a raised calcium content and therefore a higher brightness in qBEI.
As labeled in Figure 4.7 the bone - mCAR interface is a cement line (CL), similar to those between bone packets. The mCAR - nmCAR interface is called tidemark (TM). It represents the mineralization front and is a region of important biological functions. They are able to change in response to microinjuries and advances into the uncalcified cartilage [44]. Furthermore the metabolic activity of the TM is proven by tetracycline labeling [45]. Bone tissue below the tidemark is called subchondral bone (scBONE).

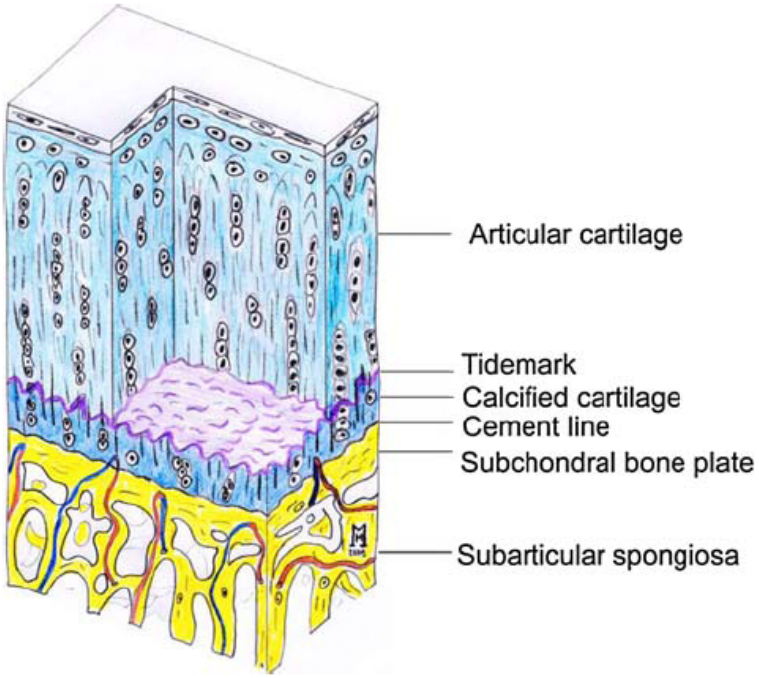

Figure 4.7: Illustration of articular cartilage and subchondral bone[44]

It is assumed that osteoarthritis causes duplication or even multiplication of the tidemark [46]. In this case one or more additional interfaces between two regions of mCAR are generated with supposable different age. They are called double or triple tidemark. However the mechanism of this tidemark multiplication is widely unknown. A previous study

showed an altered trace element concentration of Pb and Zn compared to the normal bone level [13]. Therefore, determining the spatial distribution of Pb and Zn in double tidemarks is one of the main aims of this thesis.
Figure 4.8 shows a light microscope image of a double-tidemark (DT) region.

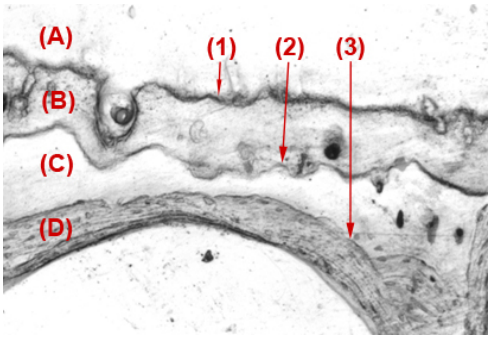

Figure 4.8: Differential interference contrast (DIC) light microscope image of a hip head, showing the transition from mineralized to non-mineralized tissue including a double tidemark and a cement line. (A): nmCAR, (B): mCAR, (C): mCAR, (D): scBONE, (1): outer tidemark, (2): inner tidemark, (3): CL

4.4 Trace elements in bone and cartilage

Human bone consists of about 20 $wt\%$ of calcium, mostly bounded in calcium-hydroxyapatite ($Ca_{10}(PO_4)_6(OH)_2$). Therefore the crystalline matrix derives to approximately 50 $wt\%$ of the calcified tissue. Beside apatite and the organic matrix, previous studies quantified the amount of trace elements (elements in concentrations in the magnitude of ppm) in various human tissues. Since Pb, Zn, and Sr are measureable with our XRF setup, the focus is on these elements.
In 1963 Becker et. al compared the concentrations of some trace elements such as Al, B, Cu, Fe, Pb, Mn, Si, Ag, Sr Sn, V, and Zn in bone of modern humans to those of human samples from the 12th century [47]. Semiquantitative arc emission spectroscopy of ashed bone showed Pb concentrations ranging from 5 to 110 ppm, Sr concentrations between 62 and 130 ppm and Zn concentrations between 60 and 85 ppm for the modern human specimens. While the Pb concentration was increased drastically compared to other groups (all samples from the 12th century showed a lead concentration lower than 5 ppm), Zn and Sr values showed no significant difference. Other trace elements were found in concentrations mostly below 100 ppm. According to ashing during sample preparation these concentrations correspond to ash-weight.
Koch et al. examined trace element concentrations (also relative to ash-weight) in various organs of humans. In this study the Pb concentration in bone varies from 30 to 930 ppm and the Zn values are about 700 ppm. The highest amounts of Zn were found in the prostate[48].

As mentioned in the introduction Pb is known for being toxic and causing damage inside of the nervous system, the renal system, the cardiovascular system, and the reproductive system. A detailed toxological profile for lead can be found in [49]. Because of the long biological half life of Pb in human bone (about 20 years), most of this element is stored in the bone (90% - 95% for adults) [13]. Furthermore, Pb is assumed to be a risk factor for osteoporosis [1][2].
The idea of Pb mobilization during phases of raised boneturnover like pregnancy or menopause leads to studies on women without direct Pb exposure [3]. By comparing Pb blood levels of various groups, these findings confirm the mechanism of bone as an endogenous lead source.

The role of zinc as an essential trace element in bone metabolism is still unknown. Recent studies verified the stimulating effect of zinc in bone formation. Atsuo et al. found a significant raise in proliferation of human osteoblastic cells and therefore a reason for enhanced bone formation after treatment with zinc-releasing calciumphosphate[50]. On the other hand it is mentioned that Zn acts as an inhibitor of hydroxyapatite-crystals growth. Hence for high Zn concentrations adverse effects on the calcification process cannot be excluded. Hyun et al. observed similar effects. Their study confirms the stimulating effect on osteoblastic proliferation [51].

The interest on Sr in bone grew during the last years according to recent osteoporosis therapies with Sr-ranelat and Sr-chloride. Several studies confirm the biologically beneficial impact. Sr acts stimulating to osteoblasts resulting in a raised bone formation. Additionally, the cell differentiation of the osteclasts is hampered. Therefore the new equilibrium of bone formation and resorption leads to a gain of bone mass[52].

Despite of these findings, there is hardly any literature about the localization of Pb, Zn, and Sr in bone. Recently Zoeger et al. used synchrotron radiation induced micro fluorescence analysis for a first examination the trace element distribution in articular cartilage[53]. A confocal setup allows element-sensitive mapping with a resolution of approximately 15 μm. He found highly significant Pb accumulation in the tidemark of articular cartilage and also a raised Zn concentration in this region as well as in the cement lines. Line profiles were taken for interpretation, but no spatial classification of various histological regions was used for data analysis.

Chapter 5

Samples and Sample Preparation

5.1 Measured samples

For the examination of cartilage and subchondreal bone, samples from the femoral head as well as from the patella were used. The study was approved by the ethics committee at the Medical University of Vienna, Austria and was done in accordance with the Helsinki Declaration. Femoral neck samples for the examination of the trace element distribution in cortical bone and in spongiosa have already been part of other studies[54]. Figure 5.1 illustrates these regions in the femur.

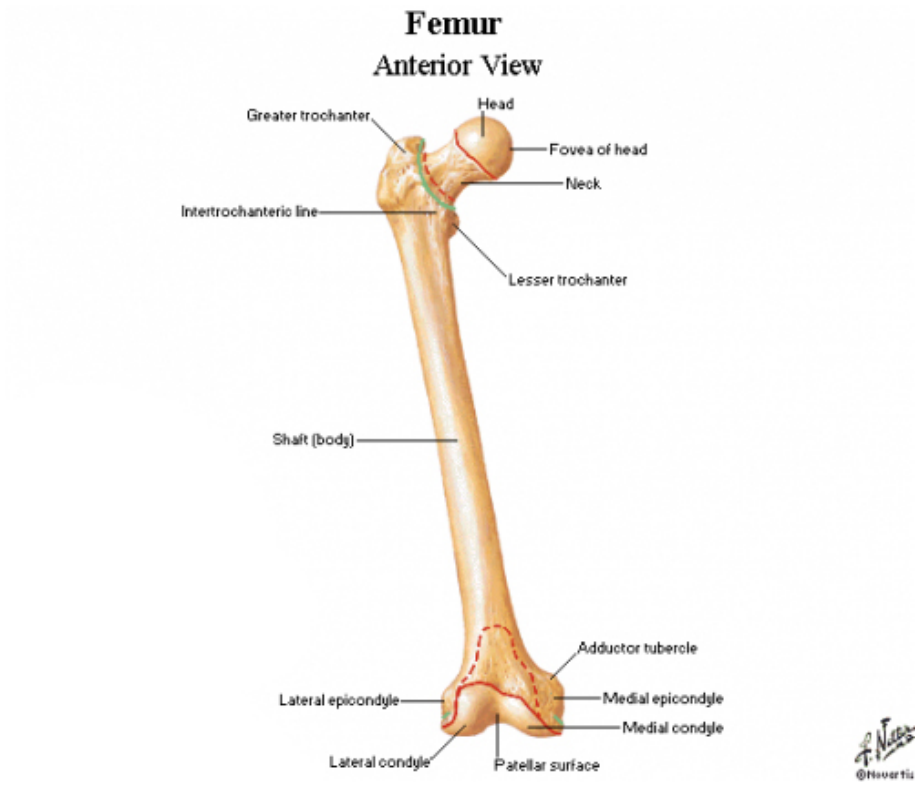

Figure 5.1: Illustration of various anatomical regions of a femur. (modified from [55])

Additionally, the analysis icludes the distribution of trace elements insinde a sclerosing osteosarcoma. This is a quite unusual tumor type, consisting of mineralized tissue; hence it shows an intense contrast in the radiograph images 7.24. Previously to the dissection of the tumor tissue the patient was treated with cisplatin.

Informed consent was obtained from all patients regarding the use of the harvested bone samples for this studies.

5.1.1 Samples for examination of the tidemark

To analyze the trace element accumulation in single tidemarks (STM) and double tidemarks (DTM) of articular cartilage, hip heads and patellas of individuals without metabolic bone disease and one osteonecrotic hip head were examined. The osteonecrotic sample (on10) was dissected from a 33 year old individual; the oa1 as well as the oa7 specimen also were also obtained fr0m surgeries. All other samples originate from forensic autopsies of individuals aged from 46 to 65 years.
Regions of DTM observation are summarized in Table 5.1,

sample	measured regions	dissected from	age	sex
x3758	a,d	patella	46	M
x3800	b,d,e,f,i	patella	54	M
a3753	c	hip head	65	W
oa7	a,b,c	hip head	72	W
on10	157, 160, 185	hip head	33	W

Table 5.1: Regions with observed DTs

Single tidemarks were found in following areas:

sample	measured regions	dissected from	age	sex
d3765	a,b	hip head	56	W
k3805	f	hip head	63	M
k3807	c,e	patella	63	M
oa1	a_a	hip head	62	M
oa7	a_b,b_a,c_a,c_b	hip head	72	W
x3758	f	patella	46	W
on10	123, 142, 162	hip head	33	W

Table 5.2: Regions with observed STs

A line scan evaluation of some of these samples is already published by Zoeger et al. in [13], [53] and [56].

5.1.2 Femoral neck samples for trace element analysis in bone

Beside the localization of trace elements in cartilage, the elemental distribution in cortical and spongious bone was also evaluated. For this purpose specimens from femoral neck of 10 postmenopausal women were dissected. To link possible alterations of the mechanial stability of bone to the elemental distribution, 5 samples of osteoporotic individuals with fragility fracturs and 5 age matched unfractured samples were measured. Biopsies of the osteopotic individuals were taken 0 - 6 days after the fracture. In every sample one region of the corticalis (region a1), and one or two regions in the spongiosa (a2, a3) were selected for measurement. Areas containing bone packets with various contrasts in the qBEI images, and therefore with various tissue age, were preferred. These specimens were used in a previous study[54].

Table 5.3 summarizes the samples.

sample	measured regions	age	group	pair number
FNX1	a1, a2, a3	89	fractured	1
FNX2	a1, a2, a3	84	control	1
FNX3	a1, a2	77	fractured	2
FNX4	a1, a2, a3	77	control	2
FNX5	a1, a2, a3	80	fractured	3
FNX6	a1, a2, a3	92	fractured	4
FNX7	a1, a2	74	fractured	5
FNX8	a1, a2	75	control	5
FNX9	a1, a2	79	control	3
FNX10	a1, a2, a3	88	control	4

Table 5.3: Properties of the femoral neck samples

Figure 5.2 shows light microscope images (circular polarized reflection interference contrast image taken with a Zeiss Axio Scope A1 microscope) of the sample FNX5, depicting the regions a1, a2 and a3. The red-framed areas show regions of approximately 570×520 μm reflecting the size of the qBEI images as well as the size of the fluorescent maps.

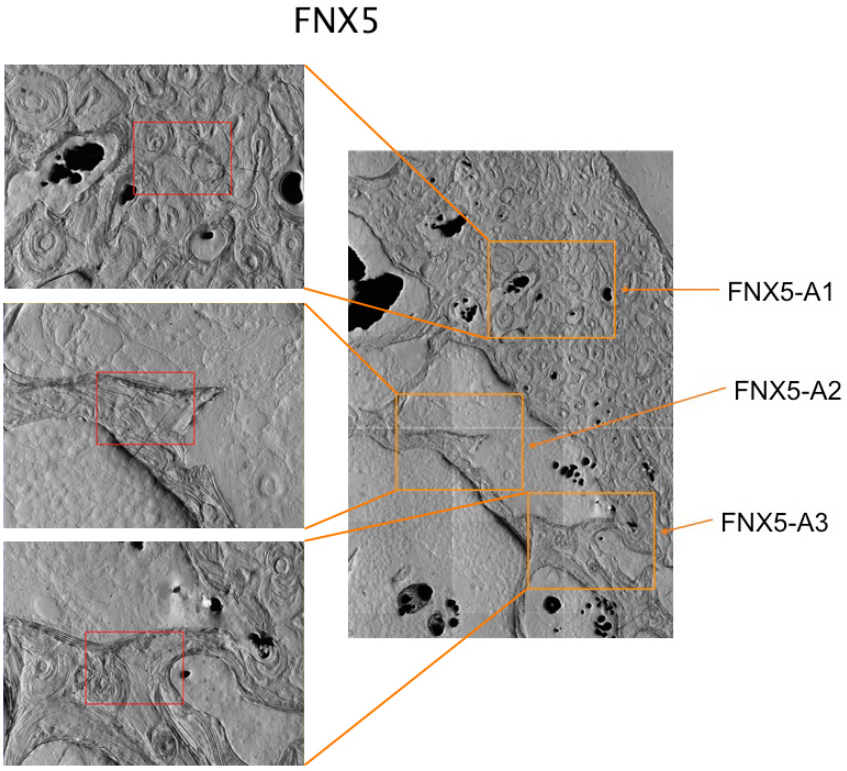

Figure 5.2: Documentation of the regions for fluorescence analysis. The red-framed areas were previously measured by qBEI.

5.1.3 Osteosarcoma

Additionally to the previously mentioned samples, the elemental distribution of an sclerosing osteosarcoma (bone tumor) was measured. It was removed from the tibia metaphysis of a 10 year old girl after a treatment with cisplatin. Figure 5.3 shows a qBEI image of an interface of healthy bone on the left and higher calcified tumor tissue on the right side. Beside other areas this region was chosen for fluorescent mapping.

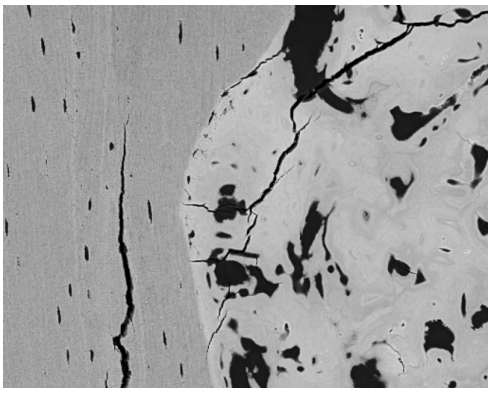

Figure 5.3: qBEI image of a bone-osteosarcoma interface. The bright bone on the right side is the tumor tissue.

5.2 Sample preparation

All samples were fixed in 70% ethanol. Dehydration was performed by a gradient series of ethanol concentrations before the specimens were embedded in polymethylmethacrylate (PMMA)[43]. The PMMA blocks were cut into about 5 mm thick sections, either perpendicular to the chondral surface or trasversal in case of femoral neck samples. The osteosarcom was dissected in longitudinal direction. The embedded bones were cut with a low speed diamond saw (Buhler, Isomet Low Speed Saw), grinded and polished with a diamond suspension (Logitech PM5, polishing device). Furthermore, the samples were carbon coated by vacuum evaporation (Ager, SEM cabon coater) to prevent charging during electron microscope operation. Because of the low thickness ($\approx 4\ nm$) and the moderate atomic weight of the carbon layer, it does not effect the fluorescent measurements. For qBEI analysis, the blocks were mounted on a specimen holder with a sticky carbon tape.

Chapter 6

Experimental Setup and Analysis

6.1 Synchrotron setup

1. Measurements at HASYLAB
   All tidemark samples except the osteonecrotic bone were measured in the scope of Norbert Zoeger's PhD thesis [13], at the beamline L of the "Hamburger Synchrotronstrahlungslabor" (HASYLAB, Hamburg, Germany). The 4.5 GeV storrage ring with max. 140 μA electron current in combination with a bending magnete provides an adequate photon flux. A detailed description of the beamline equipment can be found in [57]. A Ni/C fixed-exit double crystal monochromator system offers high photon flux, while two polycapillary focusing optics (XOS, X-Ray Optical Systems, Albany, New York) in confocal alignment provide a focal volume of $20 \times 14 \times 22$ μm (measured at an Au foil). The primary beam energy of 18 keV accounts for optimal Pb exciting. A $Si(Li)$ semiconductor-detector (Gresham Sirius 80) with 80 mm^2 cross section, 4 mm crystal thickness, and a 12 μm Be window was installed. More information about the experimental setup and the energy dependency of the polycapilarie's transmission-function can be found in [13] and [53].
   Some of the specimens were measured using a 15 μm detector-sided Al filter to reduce the dominant Ca peak and thus to get rid of unwanted artifacts. Therefore the measurements were corrected using Formula 2.15 for attenuation of X-rays in matter.

2. Measurements at ANKA
   The on10 sample as well as the femoral necks and the osteosarcoma were measured in the scope of this thesis, at the ANKA synchrotron, located at the Karlsruhe Institute of Technology (KIT, Karlsruhe, Germany). In this storage ring, electrons (max. current: 180 mA) are accelerated up to an energy of 2 GeV. Deflection devices like a wiggler, an undulator and banding magnets offer synchrotron radiation for experimental purposes.
   The FLUO beamline accounts for optimal conditions for confocal measurements. A 1.5 T bending magnet produces "white" radiation while a W/Si double multilayer monochromator offers an energy range from 1.5 keV to 33 keV. 16.7 keV were chosen for excitation. Two polycapillary half lenses provide a 17×12 μm spot with

20 μm depth resolution (measured at an Au foil). A 30 mm^2 $Si(Li)$ crystal is used as detector.
Preliminary to all measurements a depth scan was performed. The focal spot was set according to the z-position the maximum Ca signal.
More properties of the FLUO beamline are published in [58] and [59]. Figure 6.1 illustrates the beam path of the rays in a non-confocal setup. For our experiments a second capillary is mounted between sample and detector.

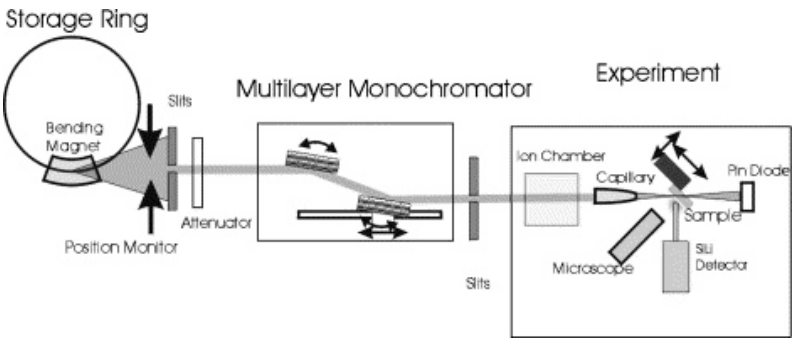

Figure 6.1: Beam path for conventional XRF at the FLUO beamline[58]

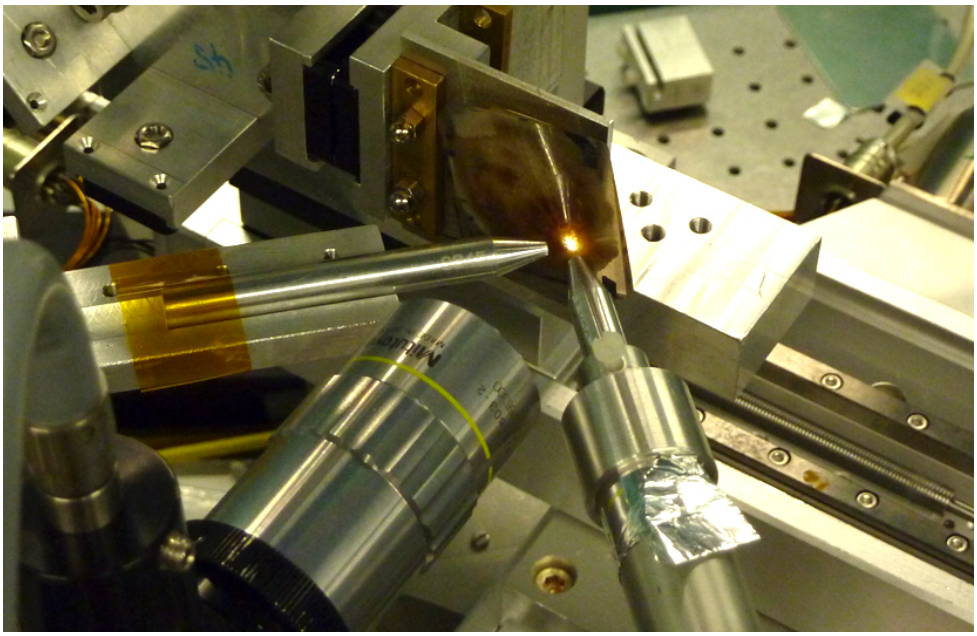

Figure 6.2: Photo of a mounted and aligned sample, the primary capillary on the left side, the detector-sided capillary on the right side, and a digital light microscope for remote control. The picture was taken at the FLUO beamline of the ANKA synchrotron.

A mounted sample, two capillaries, and a digital light microscope are shown in Figure 6.2. The alignment with 45° incidence- and reflection angle is chosen. There-

fore the angle between the beams becomes 90°. Depending on the elemental concentration the measure-time varies from 10 to 20 $s/pixel$.

6.2 Scanning electron microscope conditions

For qBEI analysis the BE signal of a SEM (DSM 962, Zeiss, Oberkochen, Germany) is used. The filament current (3.4 A) heats the tungsten hairpin cathode. The acceleration voltage is set to 20 kV and the probe current is adjusted to 110 pA. The working distance (distance between objective lens and sample) is 15 mm.
For our prurpose 200×-maginfication, resulting in a resolution of 1 $\mu m/pixel$, is approriate.

The high energy BEs were used for imaging, generating a material contrast. Hence, the BE dependency on the average atomic number of the sample is the fundament for a quantitative analysis (Chapter 3.2.1.1). For the quantification of calcium, a calibration of the BE signal is essential. Therefore C ($Z = 6$) and Al ($Z = 13$) are used as reference materials. In a qBEI image every pixel has a gray value between 1 and 256, corresponding to the backscatter electron intensity in this pixel. For calibration pure C and Al define the gray levels 25 and 225. For example a pixel of a qBEI image, which shows the same backscatter intensity like pure Al, corresponds to the gray level 225. As a result one gray level step in a qBEI image of bone is linked to change of 0.17 $wt\%$ Ca. Detailed information of the used quantification properties can be found in [39], [43], and [60]. The pressure in the vacuum chamber is kept below 10^{-5} Pa.

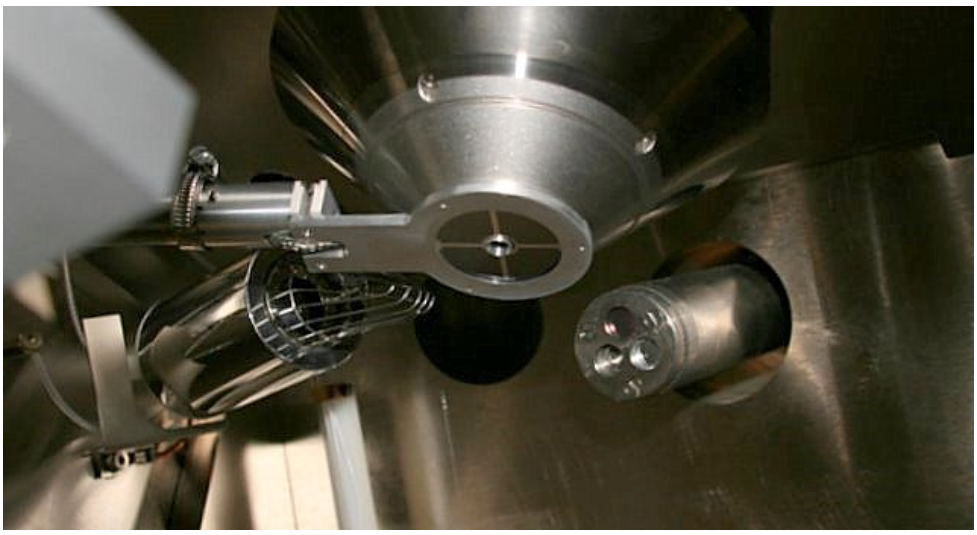

Figure 6.3: Vacuum chamber of the used SEM with a solid state detector placed around the beam entrance, the faraday cage of the ET-detector and window of the X-ray detector.

For BE measurement a solid state detector is mounted above the sample (Chapter 3.6.4). As shown in Figure 6.3 an E-T-detector is used additionally for SE measurement.

6.3 Data analysis

6.3.1 Spectrum processing

The measured spectra were processed using the AXIL - Software for Linux. This software facilitates peak-identification as well as spectrum fitting. Once a model with assumed elements and fitting parameters is created, the AXIL software fits an adequate baseline function to subtract the background from the peak areas. Therefore a linear least square fit algorithm fits a polynomial function trough the measurements. This allows separating mathematically the background signal from the peaks. After the removal of the background and considering overlapping lines, the integration over each peak results in the net peak intensities.
For all fits of femoral neck samples (FNX) the same model was used. Combined with unchanged experimental parameters, similar measurement conditions for these samples are provided.

Figure 6.4 shows a sum spectra of the FNX1 sample in logarithmic scale.

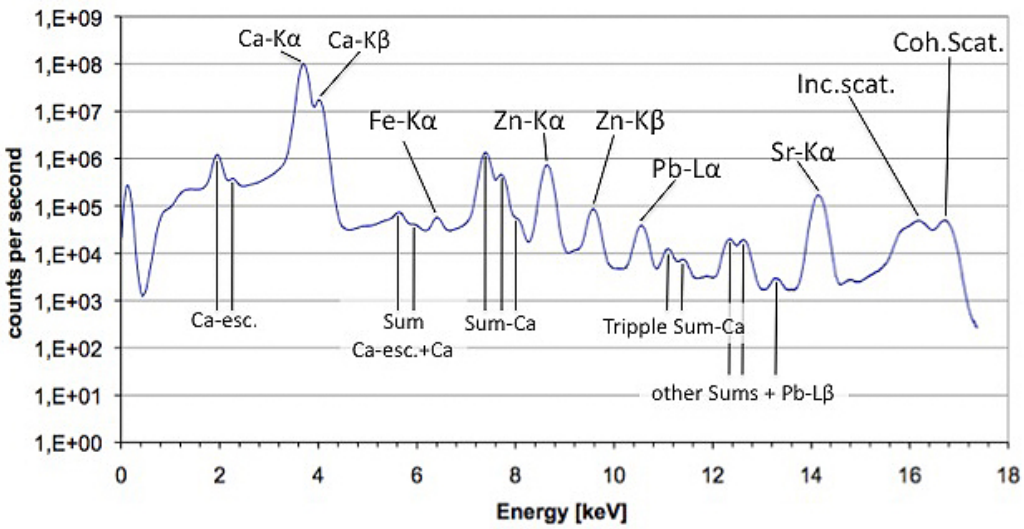

Figure 6.4: Example of an Sum-Spectra of the FNX1-a1 region with labeled peaks in logarithmic scale. The labels below the spectra denote artifacts.

For examination of the tidemark samples, the analysis parameters were changed amongst the measurements. Therefore only relative intensities within one map, or intensity rations between various maps are compared.
All maps were corrected for dead time and are normalized to 100 mA storage-ring current.

In Figure 6.5 a spectrum of a single spot at the iTM of the x3800e sample is shown in linear scale. The low background radiation facilitates peak identification.

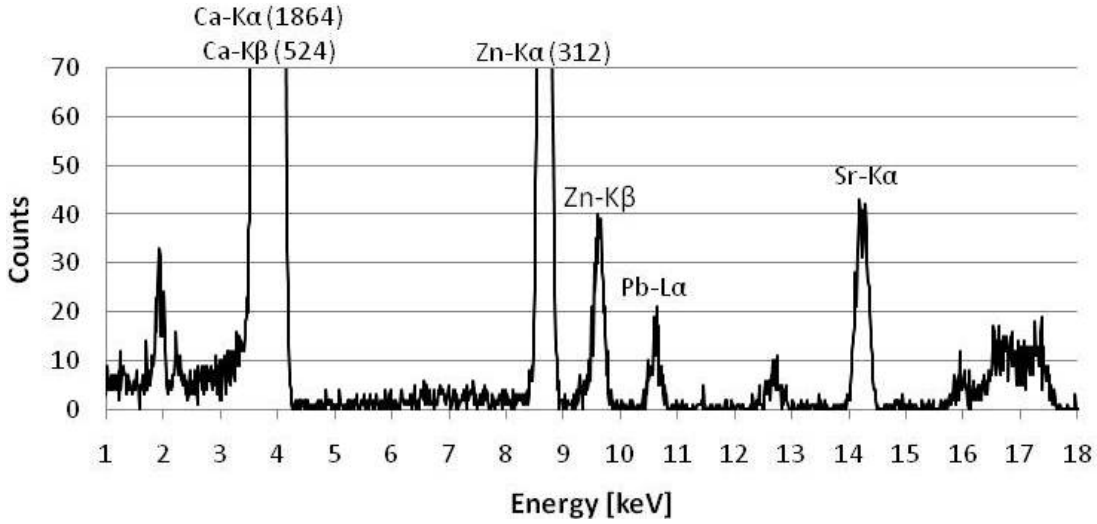

Figure 6.5: Spectrum of a single measurement spot at the iTM of the x3800e sample after 8 seconds.

6.3.2 Data analysis with ImageJ

For data analysis the ImageJ software (Version 1.44b) from the National Institutes of Health (NIH, USA) is a powerful and free possibility for two-dimensional evaluation. The combination with self-written Excel macros offers a suitable way for analysis. Statistics and diagrams were created using GraphPad Prism (version 4.0c).
ImageJ offers the ability to select regions of interest (ROIs) of an image, and to save them separately, so they can be applied to every other image with the same size. Line-drawing tools are available as well as area selections or freehand tools.

A principal problem is to directly match the elemental fluorescence maps and the qBEI images. The different resolutions (10 μm vs. 1 μm) make an exact line-up impossible, furthermore the qBEI image displays the surface of the sample (information depth about 1 μm), while despite the confocal setup, the fluorescence map still contains information about the first 20 μm below the surface. Therefore sharp contours in the qBEI image are blurred in the fluorescence maps, depending on the structure below the surface. Furthermore a cemlent line (CL) just below the surface (in exact a two-dimensional interface among two bone packets) is only visible in the fluorescent maps, but does not effect the BE signal.

In the following, outer tidemark and inner tidemark are abbreviated with oTM and iTM while mineralized cartilage and non-mineralized cartilage are denoted with $mCAR$ and $nmCAR$. Cement lines are labeled CL and $scBONE$ stands for subchrondral bone, double tidemarks and single tidemarks are labeled DTM and STM.

1. **Analysis of the articular cartilage samples.**
   To figure out the relative elemental concentration in the TM compared to other regions, the Zn-Map is used to draw the ROIs. Since the Zn signal is enhanced in the TM (Figure 6.6) and also in most of the cement lines, this helps to label homogeneous regions. In combination with the qBEI image, these regions are allocated to the histological structure. The ROIs of the iTMs, the oTMs, and the STMs (if only one tidemark is observed) are selected by a 2 px (≈ 20 μm) broad region from the Zn map. mCAR and scBONE are selected with respect to the Zn-indicated cement lines and are labeled after comparison with the qBEI image. Additionally the region of nmCAR was marked.

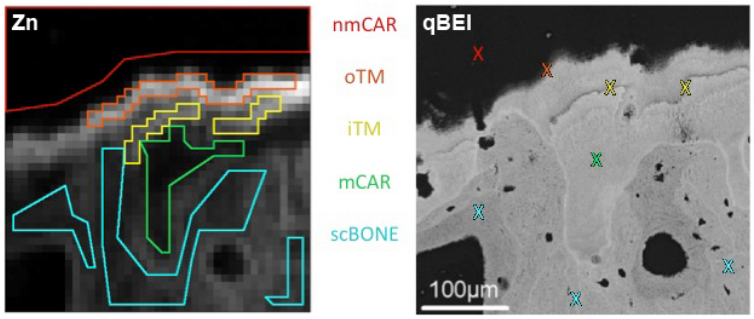

Figure 6.6: Zn map (left) an qBEI image (right) of a DTM region. Various ROIs are framed differently. In the qBEI image the related regions are marked in the corresponding colors.

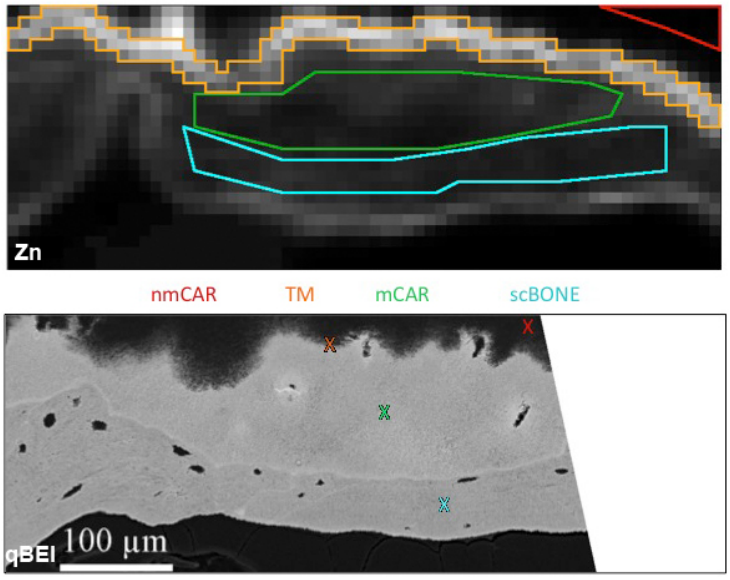

Figure 6.7: The upper image shows the Zn map of a STM-region. In the qBEI image the associated histological regions are marked.

Figure 6.6 shows the Zn distribution in a sample with a DTM and the related qBEI image. The ROIs are labeled and can be applied to other elemental fluorescent maps.
Additionally to this example of a Zn map, the Pb, Sr, and Ca maps are overlaid by the ROIs. In absence of a second tidemark (which is the usual case), the tidemark is labeled TM while the other ROIs are denoted similarly (Figure 6.7).

2. **Analysis and normalization of femoral neck-samples**
According to bone packets (BP) with distinct Ca content and to the sharp edges of bone borders (BB) and BP, it was possible to match the elemental maps and the qBEI image, even if the variation in the information depth sometimes still causes inconsistencies. Now the Ca-map can be lined up with the qBEI image, so the ROIs can be drawn directly in the qBEI image.

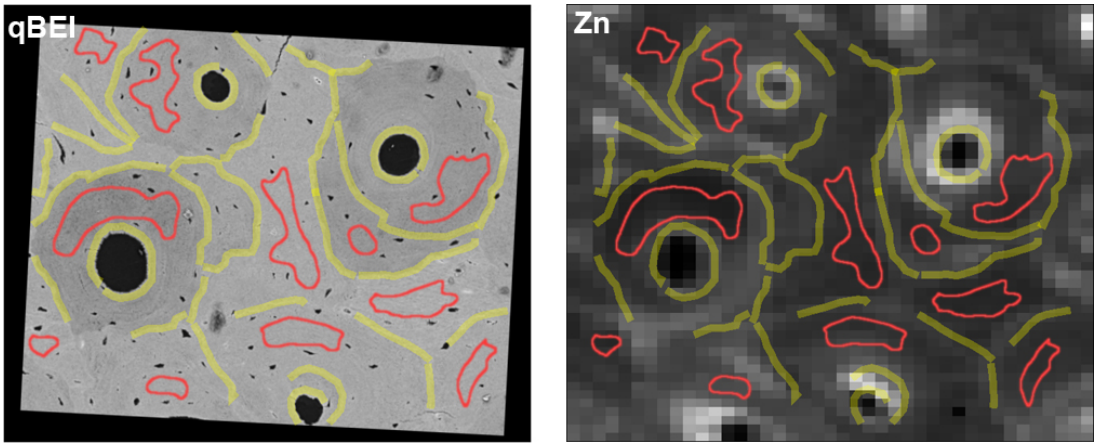

Figure 6.8: BP (red regions) mark representative ROIs of the bone packets. The yellow lines are 10 μm thick and correspond to CL and OB.

Additionally to BPs cementlines (CL), BB, and borders of osteons (OB) are also labeled, independently of their occurrence in the elemental maps. While the BP - ROIs are chosen apart from other structures, a 10 μm thick line labels the CL - ROI at the interface of two bone packets. For the evaluation of OBs and BBs a 10 μ m thick region inside the bone tissue close to the border, was selected (Figure 6.8).
Since osteons and cracks are excluded from the BP - ROIs the quantitative character of the qBEI image can be used to normalize the fluorescence maps. Therefore comparability between different maps and samples is provide, even if small variations in the measurement setup would have caused systematical errors.
A factor K is derived from averaging the qBEI / Ca-fluorescent ration of all bone packets of the map (Formula 6.1).

$$K = \frac{1}{i} \cdot \sum_{i=1}^{BP} \frac{wt\%Ca_i}{FluoInt(Ca)_i} \tag{6.1}$$

$wt\%Ca_i$ stands for the averaged Ca-concentration in the bone packet i evaluated from the qBEI image as dscribed in Chapter 6.2. $FluoInt(Ca)_i$ is the mean Ca-fluorescence-intensity (derived by AXIL data evaluation) of the bone packet i.
As K is multiplied with the elemental intensities, they get normalized relative to the qBEI image. In the following Ca-norm, Sr-norm, Zn-norm and Pb-norm correspond to this normalization. As a matter of fact the expression $Ca\text{-}norm = K \cdot FluoInt(Ca)_i$ should correlate with the real Ca concentration (Figure 6.9). Outliners indicate an inhomogenous structure below the surface and hence an altered fluorescent signal.

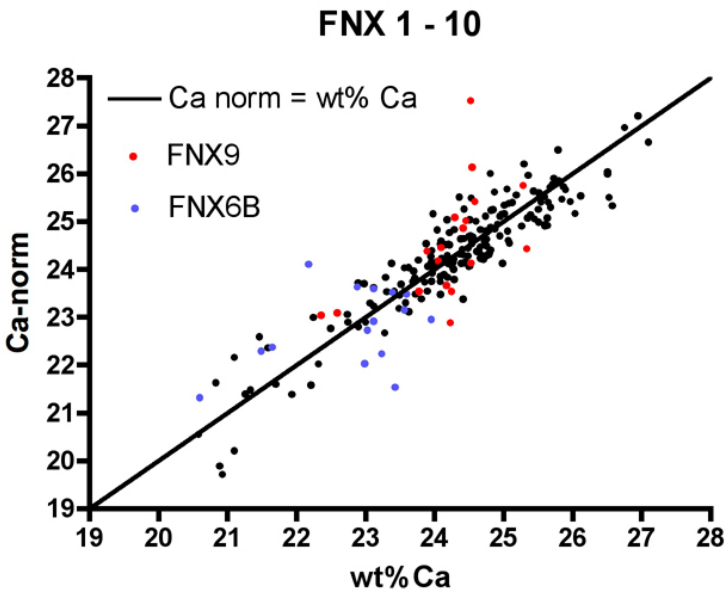

Figure 6.9: Plot of the normalized Ca values versus the qBEI concentrations. Ideally the points should fit the black line.

After the ROI-selection, ImageJ measures the ROIs and saves the mean intensity values as well as the selected areas for further calculations in Microsoft Excel.
Note that ImageJ processes the intensity in every pixel and therefore the measured count rates, not only the 256 displayed gray values.

Chapter 7

Results

7.1 Trace elements in cartilage and subchrondral bone

7.1.1 Evaluation of regions with double tidemarks

The analysis of outer tidemarks (oTM) and inner tidemarks (iTMs) shows a concentration localization of Zn and Pb in this regions. Surprisingly, there is a clear difference between the distributions of Pb and Zn.

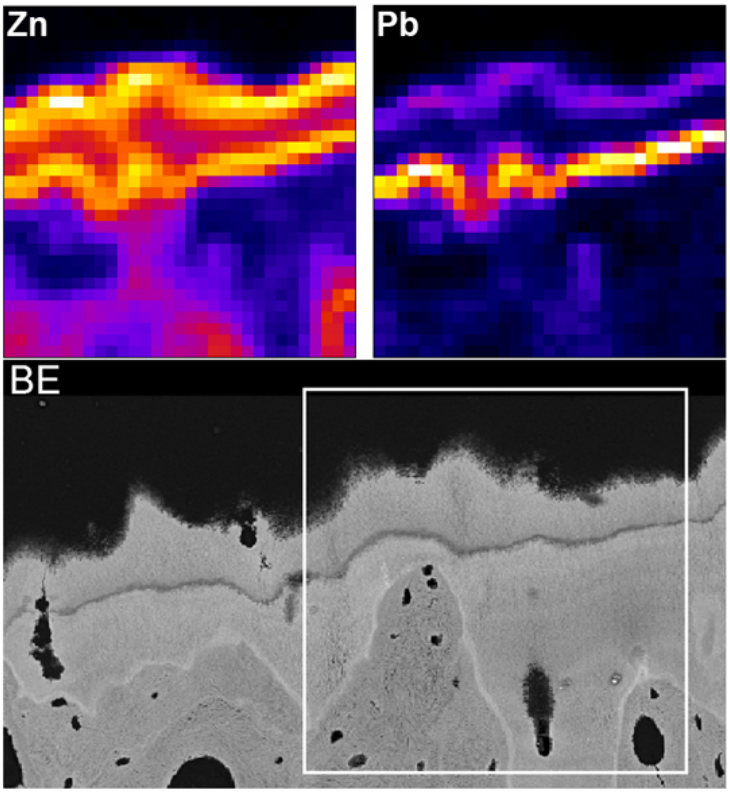

Figure 7.1: Zn map, Pb map and qBEI image of a double tidemarke in region x3800e

Figure 7.1 shows the Zn map and the Pb map color coded (heat LUT), as well as the qBEI image of the sample x3800 - region *e* as an example.
An overview of the iTM/oTM relation of all measured regions with double tidemarks (DTM) is given in Figure 7.2. The Zn intensity at the iTM of the samples x3758, a3753 and on10 is similar to the intensities in the oTMs. Therefore an equal Zn concentration in these regions is concluded. The samples x3800 and oa7_a show a slight decrease of Zn in the iTM.
The Pb distribution shows a totally different behavior. The concentration of Pb in the iTM varies from the 1.3 fold to the 3.8 fold of the oTM. The most drastic differences in the Pb signals are observed in the x3800 and the in on10 samples.

The lowered Ca concentration in the oTH compared to the iTM can be explained by the decrease of the Ca content at the border to non-mineralized tissue. This indicates that the oTM-ROI(region of interest), as marked by the Zn map, is close to the edge to non mineralized cartilage (nmCAR).
Concentrations of Sr and Ca are positivly correlated. Only the on10 sample shows a lower Sr signal in the iTM while the Ca intensity is enhanced in the iTM. The dashed line in Figure 7.2 labels equal elemental distribution.

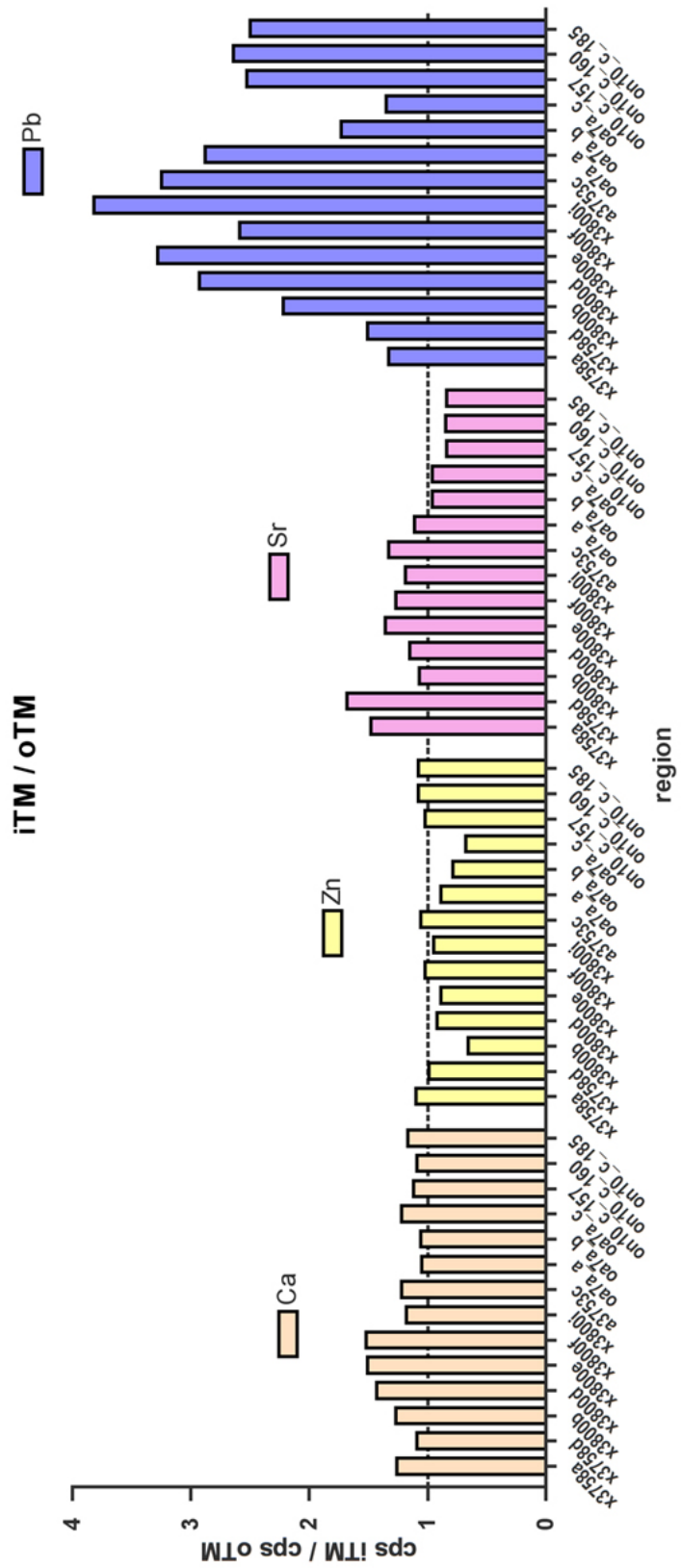

Figure 7.2: Differential Pb accumulation of the inner tidemark (iTM) and the outer (oTM). The dashed line represetns equal distribution in both tidemarks. An overview of the samples is given in Chapter 5.1.1.

Beside the characteristic trace element localization in the tidemarks (TM), Figure 7.3 also shows drastic enhancement of Pb and Zn compared to subchondral bone (scBONE). This behavior is observed in all TMs. Again the dashed line stands for equal elemental distribution. Compared to the scBONE level, the Zn concentration in the iTM is increased to the 2.5 fold up to the 7.0 fold, while the Sr distribution only shows a slight trend for enhanced accumulation in the iTM. The extreme Pb accumulation in the iTM becomes obvious in the right diagram of Figure 7.3. In comparison to the bone level, Pb is enhanced by the factors ranging from 5.4 to 53.2. The scale of the Pb diagram is changed.

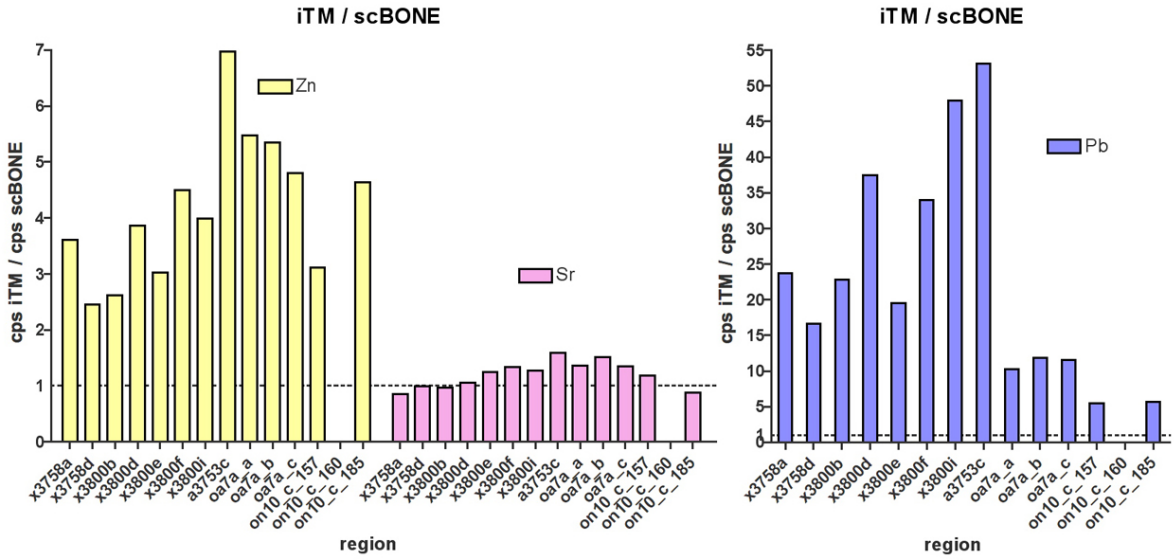

Figure 7.3: Concentration of trace elements in the inner tidemark (iTM) relative to the subchondral bone (scBONE) level.

As a result of the differential Pb accumulation in the TMs, the increase in the oTM relative to the Pb bone level is less distinct than in the iTM. The enhancement is between 2.2 and 17.8 (Figure 7.4). The Zn concentration in the oTM relative to scBONE is equal to the iTM/scBONE relation.

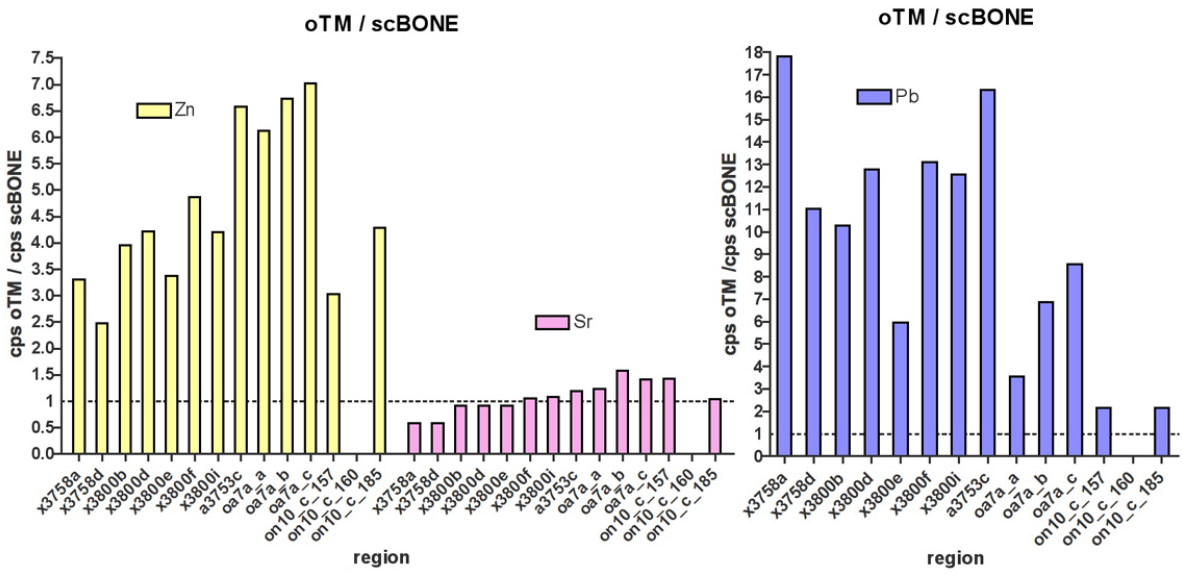

Figure 7.4: Concentration of trace elements in the outer tidemark (oTM) relative to subchondral bone (scBONE) level

Additionally to the evaluation of the relative concentrations in the TMs, the maps offer the ability to compare the elemental distributions of scBONE and mineralized cartilage (mCAR) (Figure 7.5). In non of the measured regions of the on10 sample, enough mCAR and scBONE was observed, so sample is missing in the diagram. While for the Zn and the Sr signals of these two regions no general trend is observed, the Pb concentration is significantly reduced in the scBONE. Since ROIs of mCAR are chosen with an adequate distance with regard to the iTM, this cannot be only explained by the closeness of the scBONE to Pb-rich iTM.

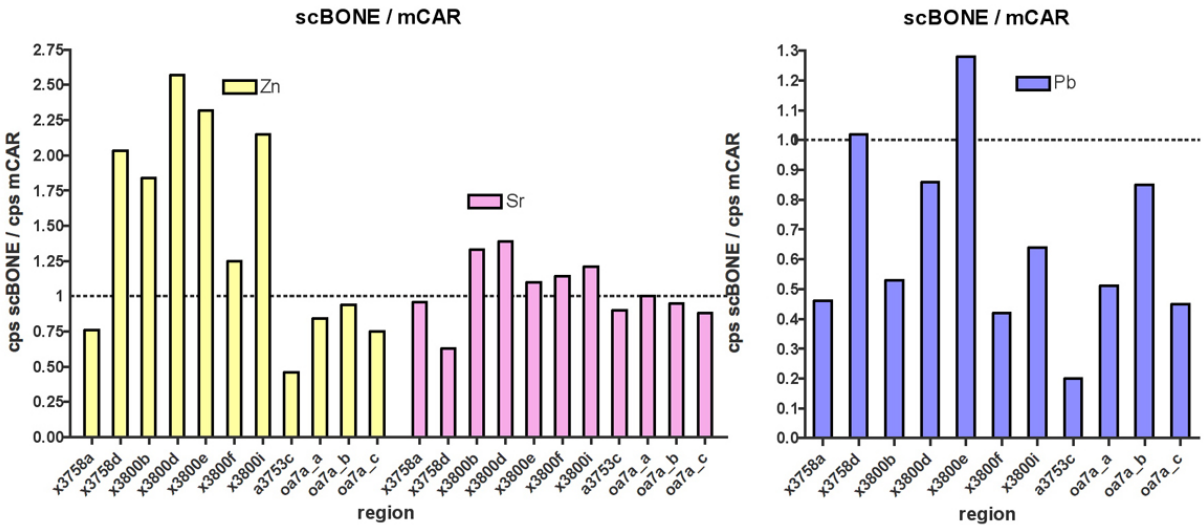

Figure 7.5: Differences in the elemental distribution between subchondral bone (scBONE) and mineralized cartilage (mCAR). The on10 sample is not displayed.

From more detailed analysis of the on10 sample, some additional information on the trace element accumulation can be gained. Maybe because of lower age of the on10 individual the Pb concentration in all ROIs of this sample is significantly lower compared to all other samples. While the Pb/Ca count rate ration in all other scBONE ROIs varies between $1.6 \cdot 10^{-4}$ and $6.6 \cdot 10^{-4}$, the on10 sample shows a Pb/Ca count rate relations between $5 \cdot 10^{-6}$ and $1 \cdot 10^{-5}$. Assuming a nearly constant Ca content and unchanged measurement conditions, the Pb concentration in scBONE of the on10 sample can be estimated to an least 10 times lower concentration compared to all other samples. The Pb/Ca count rate rations in the TMs, and in the mCAR show a similar or even more distinctly reduced PB content in the on10 sample. Surprisingly the Zn intensity is also reduced by the factor 10 or more. Despite these clearly reduced Pb and Zn contents in the on10 sample, it does not appear as outlier in the showed diagrams, which reflect the relations between various ROIs. Therefore it can be assumed that the mechanism of Pb and Zn accumulation does not depend on the absolute elemental concentration in these regions.
Note that the Pb/Ca count rate relation does not reflect the Pb/Ca concentration relation! (See Chapter 2.5)

7.1.2 Evaluation of regions with single tidemarks

The evaluation of the single tidemark (STM) data confirmed the findings about principal elemental relations between TM and scBONE. Figure 7.6 illustrates the Zn and the Pb distribution color coded (heat Look Up Table (LUT)) in comparison with the qBEI image. The TM shows an enhanced Zn and Pb intensity. Some regions in the scBONE also seem to contain high amounts of Zn.

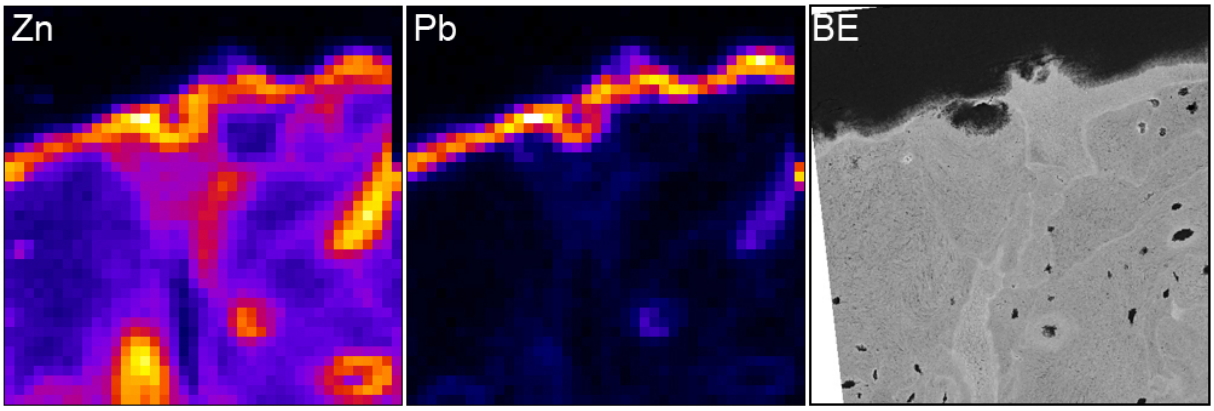

Figure 7.6: Zn map, Pb map and qBEI image of region c in sample K3807

The TM/scBONE relation reflects the results of the double tidemark (DTM) samples. While the Zn concentration in the TM is enhanced by factors between 2.2 an 6.8 compared to the scBONE, the Pb intensity in the TM is raised drastically, ranging from the 7.0 fold to the 57.7 fold of the scBONE level. Therefore it cannot clearly be determined whether the STM behaves like the iTM or the oTM of a DTM sample. Since the mean value, calculated from the TM/scBONE relations of all STM regions, is 19.2 and furthermore 23.0 for iTM and 9.5 for oTM. This indicates that a STM acts like a iTM of a DTM

sample. According to the large standard deviations this cannot be statistically confirmed. Again, despite the low Zn and Pb concentrations, the on10 sample shows a behavior comparable to the other samples and does not act as outlier.

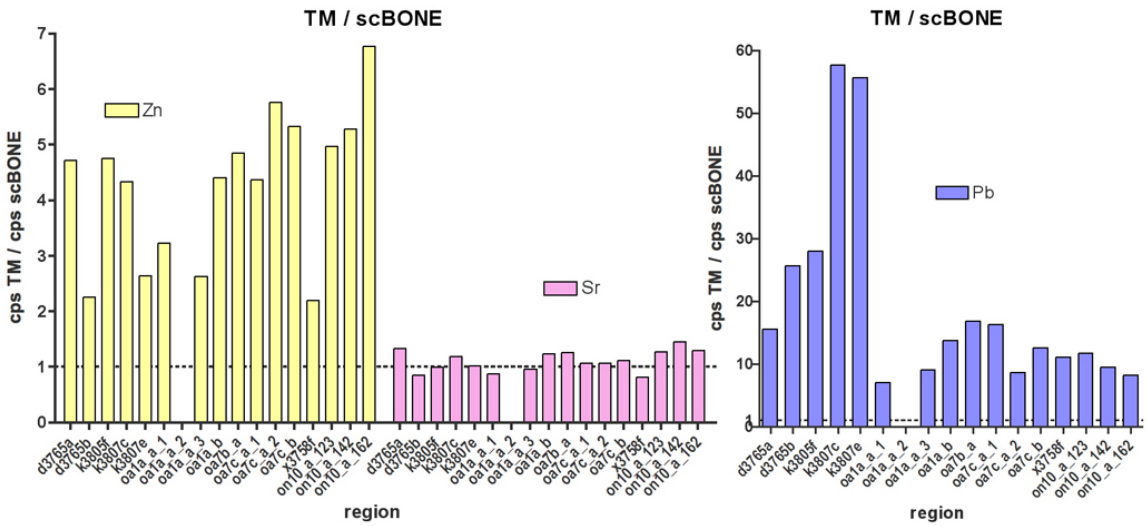

Figure 7.7: Trace element concentration in a single tidemark (TM) relative to the subchondral bone level (scBONE)

For completeness the scBONE/mCAR diagram for the STM samples is shown in Figure 7.8. The Zn and the Pb distributions confirm the findings from the DTM samples; again a significantly lower Pb concentration was found in the scBONE compared to mCAR. The Sr concentration seems to be slightly reduced in scBONE in the STM samples.

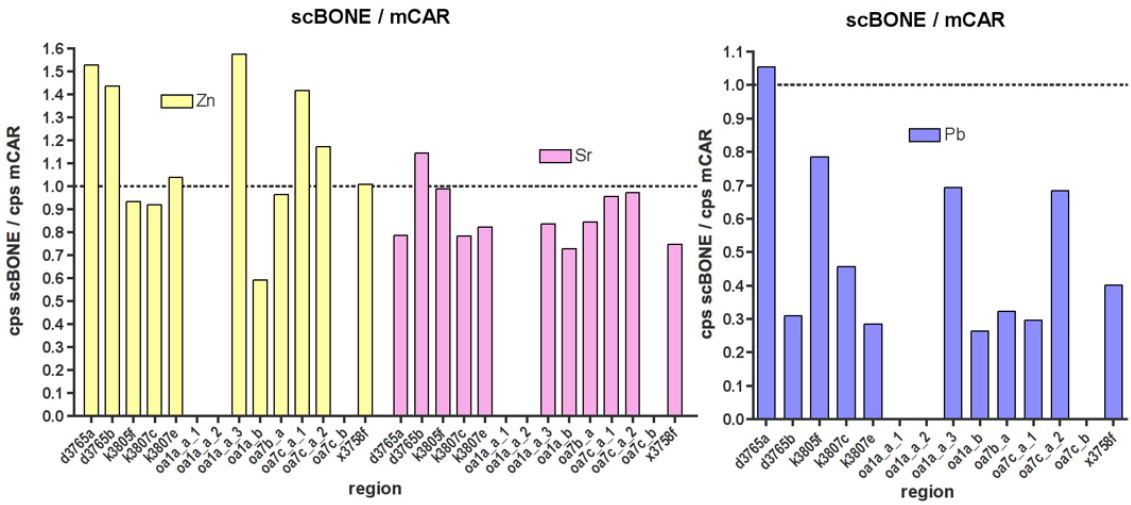

Figure 7.8: Comparison of Pb, Sr and Zn of subchondral bone (scBONE) and mineralized cartilage (mCAR). The on10 sample is not displayed, because of little mCAR tissue in the measured regions.

7.2 Localization of trace elements in femoral necks

Five femoral neck samples of postmenopausal osteoporotic women with hip fractures (FNX1, FNX3, FNX5, FNX6, FNX7) and five age matched controls (FNX2, FNX4, FNX8, FNX9, FNX10) of individuals with no signs of bone diseases are examined. A differential uptake of Pb, Sr, and Zn is observed in the elemental maps of the cortical bone as well as in the trabecular matrix. Figure 7.9 shows color coded images of a region in the corticalis in comparison to the qBEI image in the FNX1 specimen. Bright/yellow regions correspond to a high fluorescence intensity, and therefore to a high elemental content, while dark blue regions are linked to low fluorescence signals. Since the scale is changed among the maps and due to differential excitement, a direct countrate comparison of the maps is not possible.

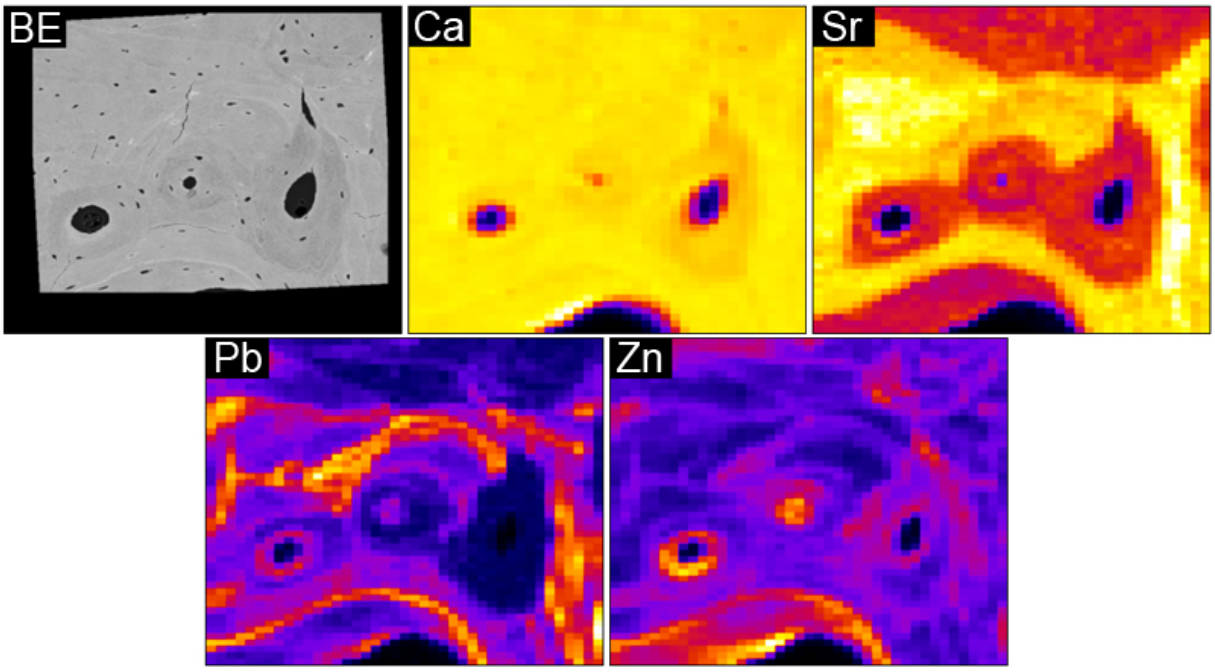

Figure 7.9: Fluorescence maps and the qBEI image of the FNX1-a1 region, as example for cortical bone of a individual with hip fracture. Bright regions correspond to intense signals.

A similar trace element localization is observed in the spongy matrix. Figure 7.10 gives an example of such a region in the FNX7 specimen. Additionally to mature, lamellar bone, so called woven bone is present close to the border of the trabecula. It represents a primary bone tissue, which usually appears during fracture healing. Actually, the FNX7 sample originates from an individual with hip fracture. Regions of woven bone as well as the bone borders (BB, the inter fasce to the bone marrow) of this sample show an enhanced Zn content compared to the bone level.

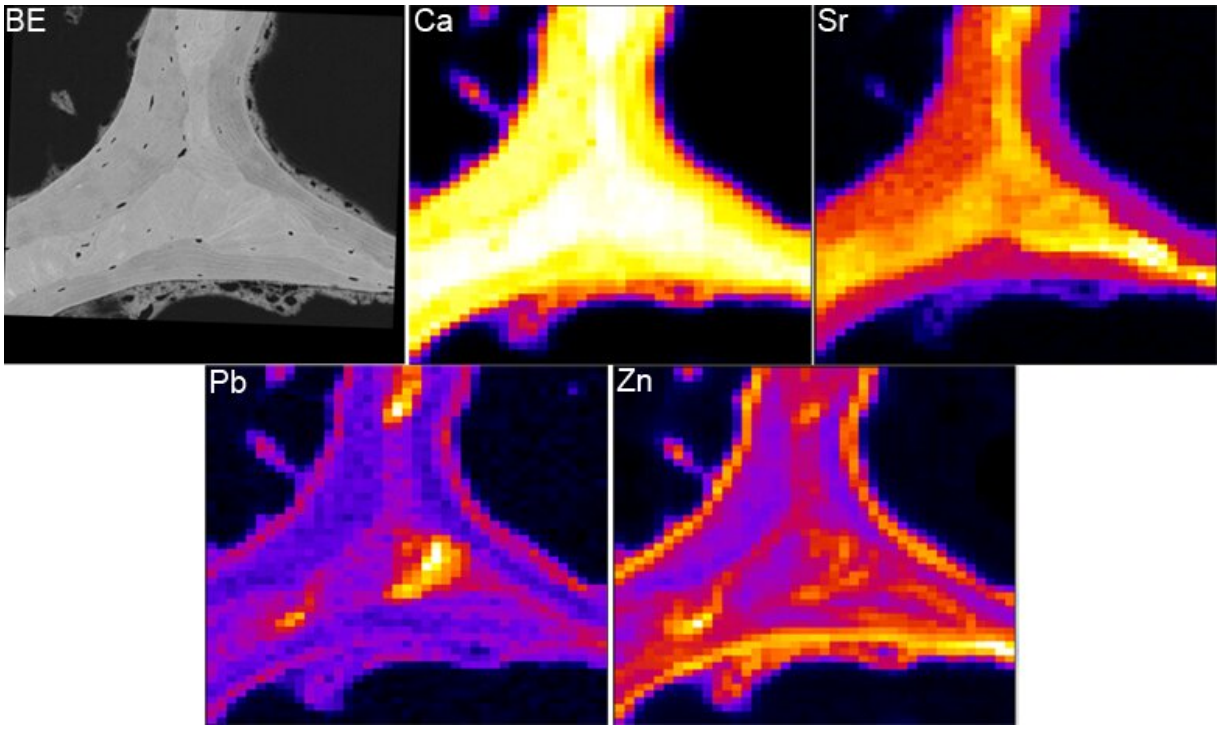

Figure 7.10: qBEI image and the corresponding elemental maps of the FNX7-a3 region.

Due to the Zn and the Pb distributions in Figure 7.9 and 7.10 an increased concentration of these elements in some of the cement lines (CL) is observed. The Zn map of the sample FNX6B (Figure 7.11) gives an impressive example for Zn incorporation. By comparison to the qBEI image, the regions of high Zn intensity at the right side of the image can be clearly linked to the CLs. CLs at the left side contain less Zn. Since there was hardly any Pb measured in this specimen, no information of Pb uptake can be gained in these CLs .

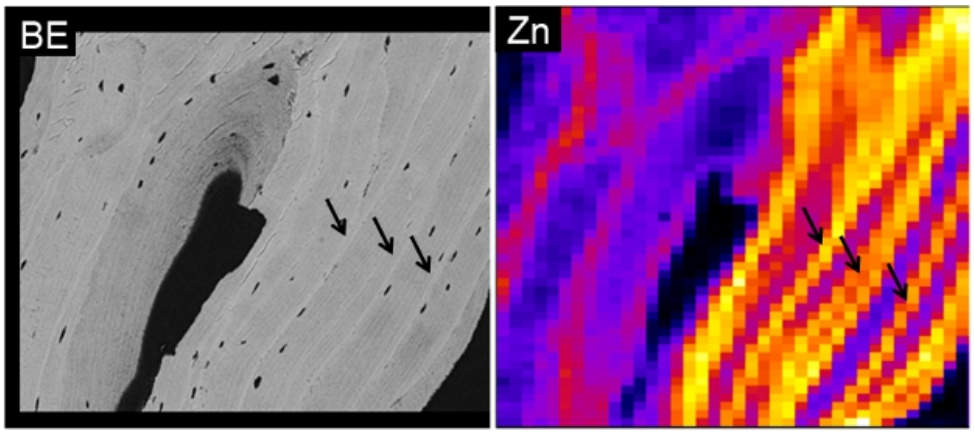

Figure 7.11: Zn map and qBEI image of the FNX6B-a1 region. The bright stripes in the map can be associated to the cement lines.

Based on the last three figures, the distributions of Zn, Pb and Sr is characterized as follows, and can be statistically confirmed.

1. In general CLs contain a higher amount of Zn compared to the bone packets (BP).
2. In the CLs the Pb distribution correlates with the Zn signal, therefore it is also enhanced in the CLs.
3. Sr is not accumulated in the CLs.
4. Young, low mineralized bone contains less Pb than matrices with high mineral content.
5. Sr is predominantly accumulated in old bone, while young bone represents a region of lower Sr content.
6. In the bone packets (BP) the average Ca content is not linked with the Zn concentration.

In the following figures the diagrams on the left correspond to fractured femoral necks of osteoporotic individuals, while the diagrams on the right represent unfractured age matched controls. The values of Ca-norm, Zn-norm, Sr-norm and Pb-norm correspond to the normalizations to the qBEI image as described in Chapter 6.3.2.

1. **Localization of Zn in CLs**
   Figure 7.12 and 7.13 show the Zn intensity, normalized to the qBEI image as described in Chapter 6.3.2. Since no Gaussian distribution of the trace elements is suggested, the nonparametric Mann-Whitney t-test is used for all statistics to check for significant elemental alterations between BP and CL. The whisker plots illustrate median, upper and lower quartile and the range.

   There are no significant intensity variations within an individual; therefore all maps of a sample are merged to one diagram.

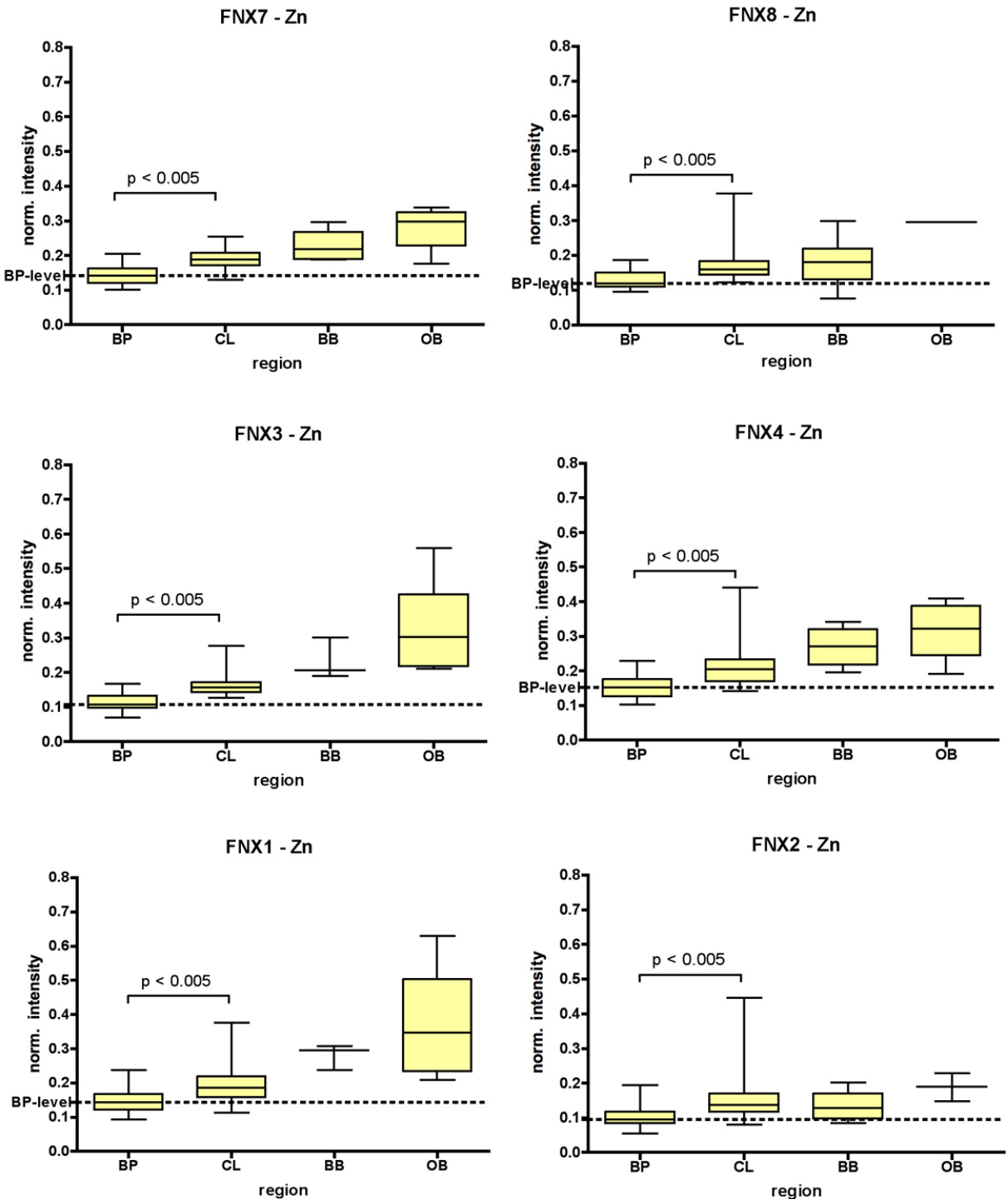

Figure 7.12: Normalized Zn intensities in bone packets (BP), cement lines (CL), bone borders (BB) and osteon borders (OB). The dashed line represents the bone level. The left column corresponds to samples with osteoporotic fractures. The age matched controls are on the right.

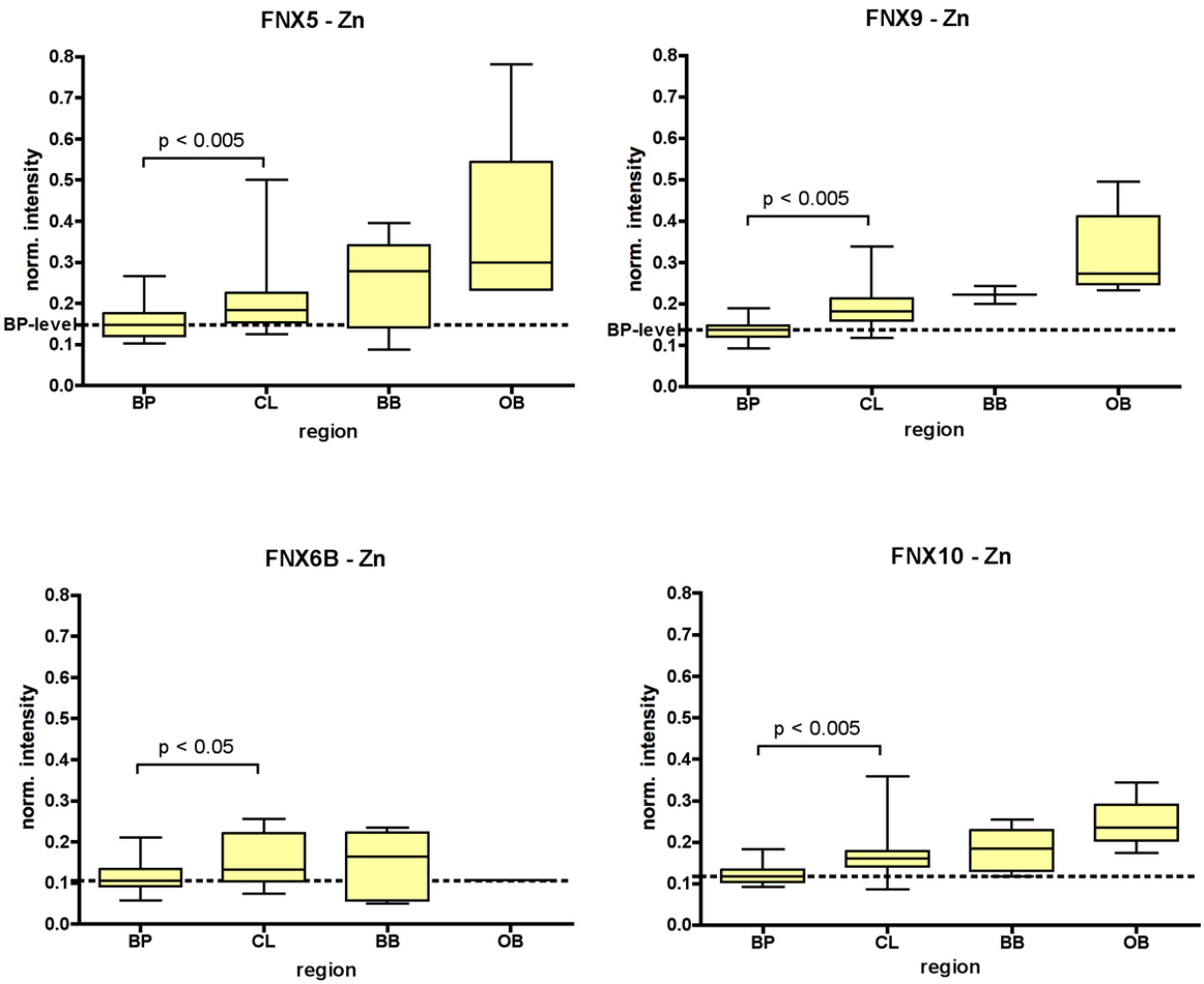

Figure 7.13: Normalized Zn intensities in bone packets (BP), cement lines (CL), bone borders (BB) and osteon borders (OB). The dashed line represents the bone level. The left column corresponds to samples with osteoporotic fractures. The age matched controls are on the right.

Fractured samples as well as controls show a significant increase of Zn in the CLs compared to the bone level (dashed line).
Due to the low number of BB and OB regions, no statistical analysis was performed for these regions, but the trend to an increased Zn signal is present in all samples. Some OBs and BBs show a high Zn content, while in others only the bone level concentration is detected. An explanation of the Zn-variations in these regions was not found.

2. **Localization of Pb in CLs**
   The evaluation of the Pb intensities leads to comparable results between all samples. All individuals (except the FNX6B sample, where extremely low amounts of Pb were detected) show a significantly enhanced Pb content in the cement lines. The Pb increase in BBs and OBs is less distinct compared to Zn.

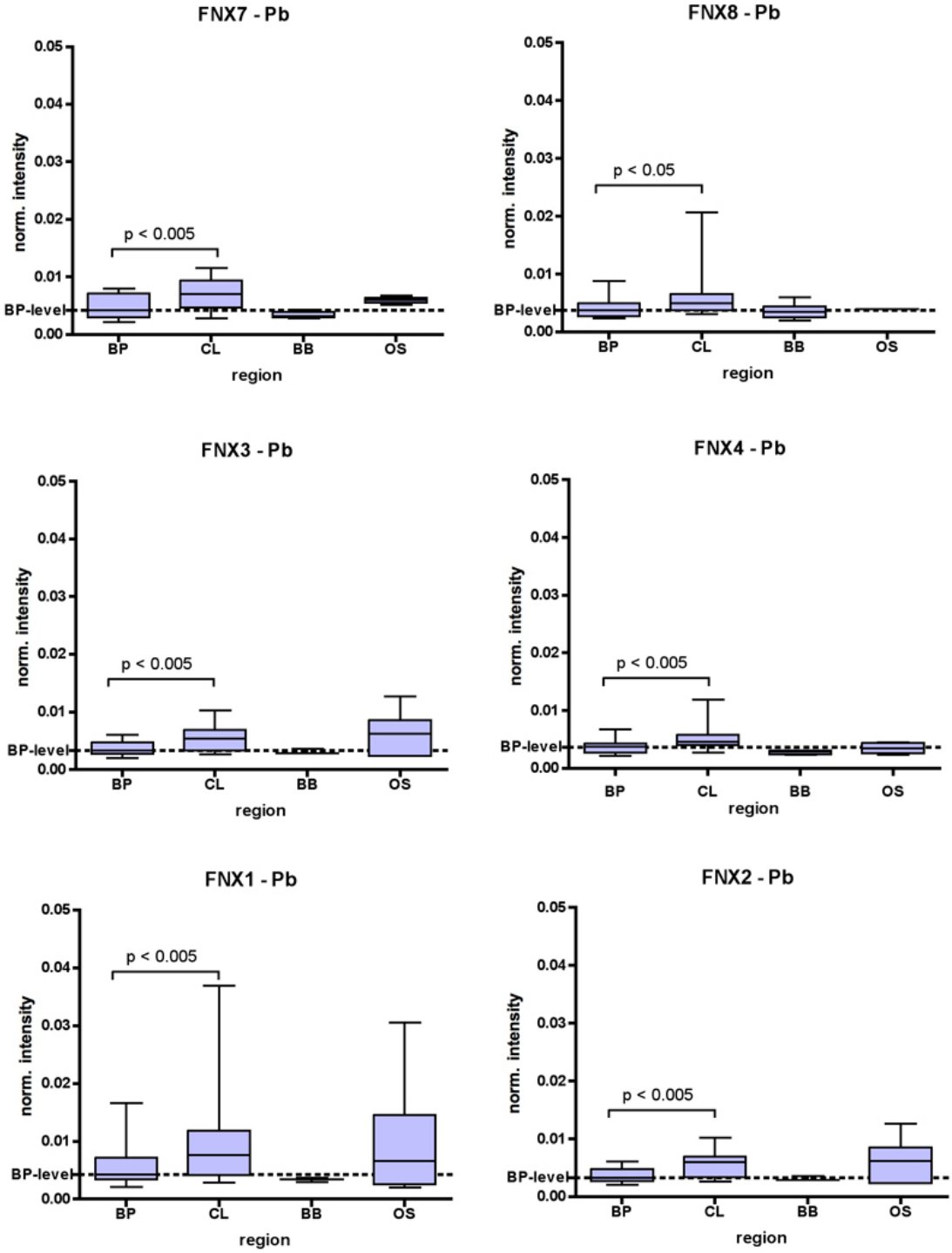

Figure 7.14: Normalized Pb intensities in bone packets (BP), cement lines (CL), bone borders (BB) and osteon borders (OB). The dashed line represents the bone level. The left column corresponds to samples with osteoporotic fractures. The age matched controls are on the right.

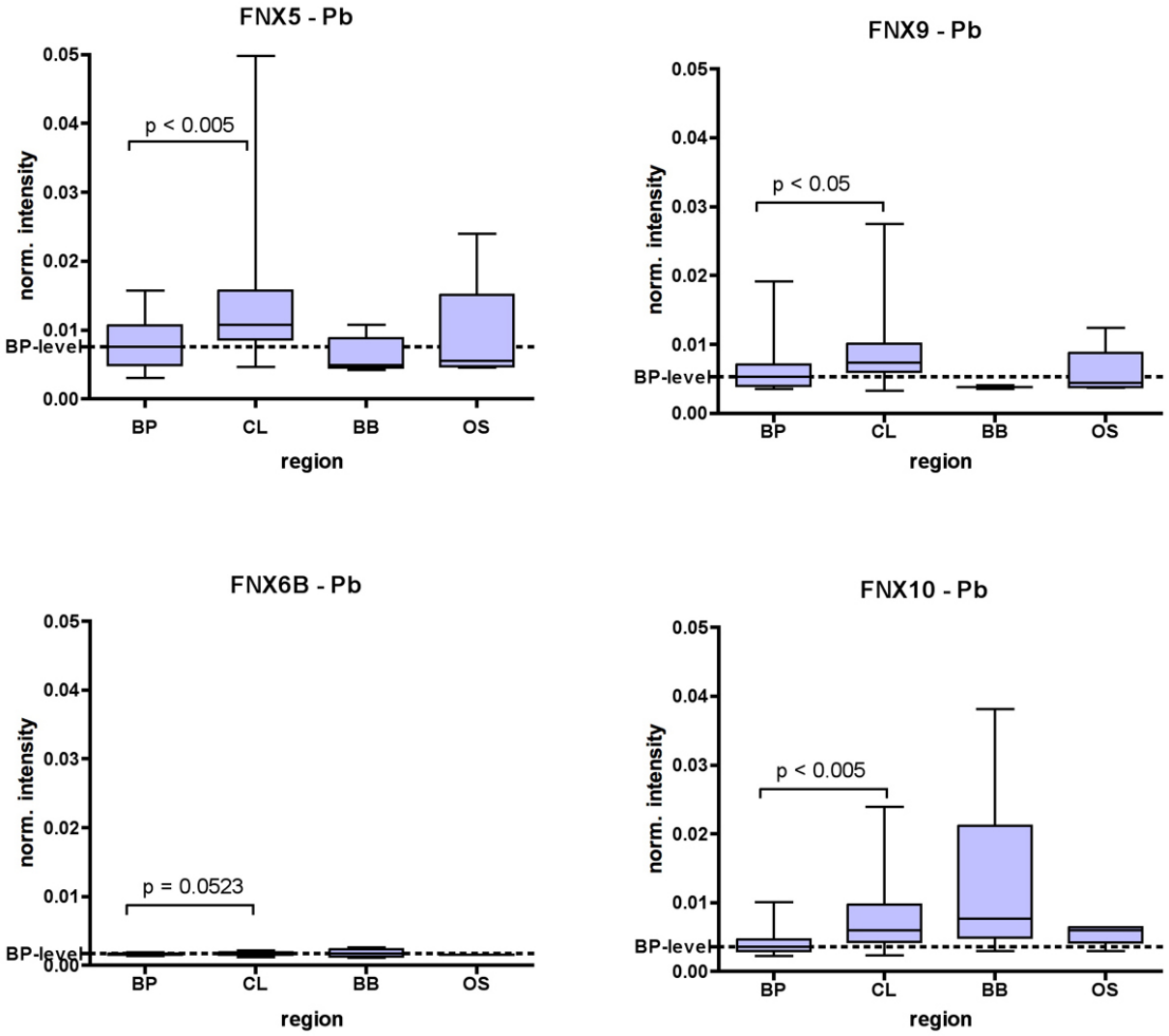

Figure 7.15: Normalized Pb intensities in bone packets (BP), cement lines (CL), bone borders (BB) and osteon borders (OB). The dashed line represents the bone level. The left column corresponds to samples with osteoporotic fractures. The age matched controls are on the right.

3. **Relative concentration of Sr in CLs**
   The observation of equal Sr concentration in CLs and BPs is consistent with Figure 7.16 and 7.17. A Sr accumulation in the CLs can be excluded. The reduced Sr intensity in BB and OB can be explained by the closeness to the embedding material in combination with the not perfect qBEI image overlay.

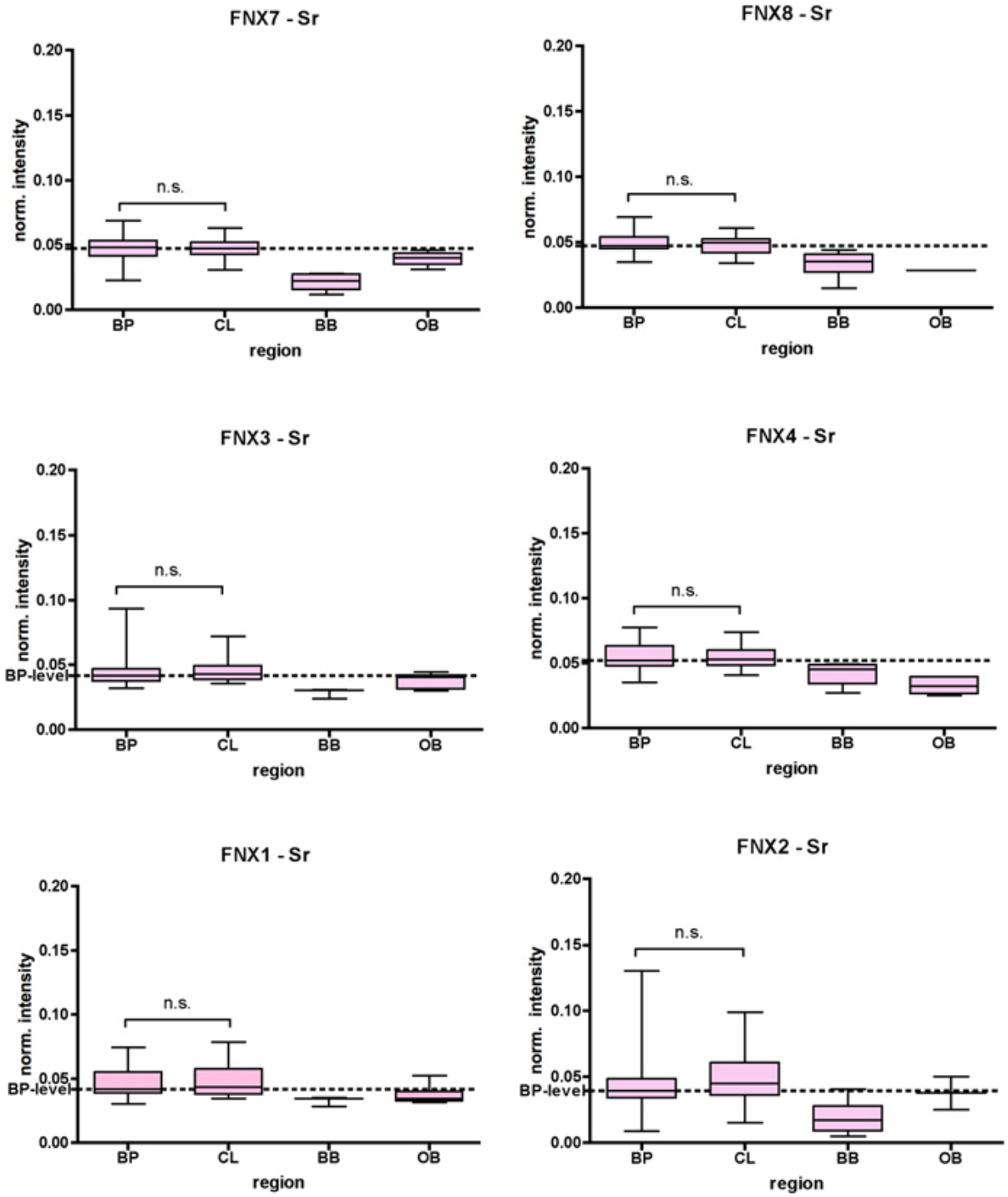

Figure 7.16: Normalized Sr intensities in bone packets (BP), cement lines (CL), bone borders (BB) and osteon borders (OB). The dashed line represents the bone level. The left column corresponds to samples with osteoporotic fractures. The age matched controls are on the right.

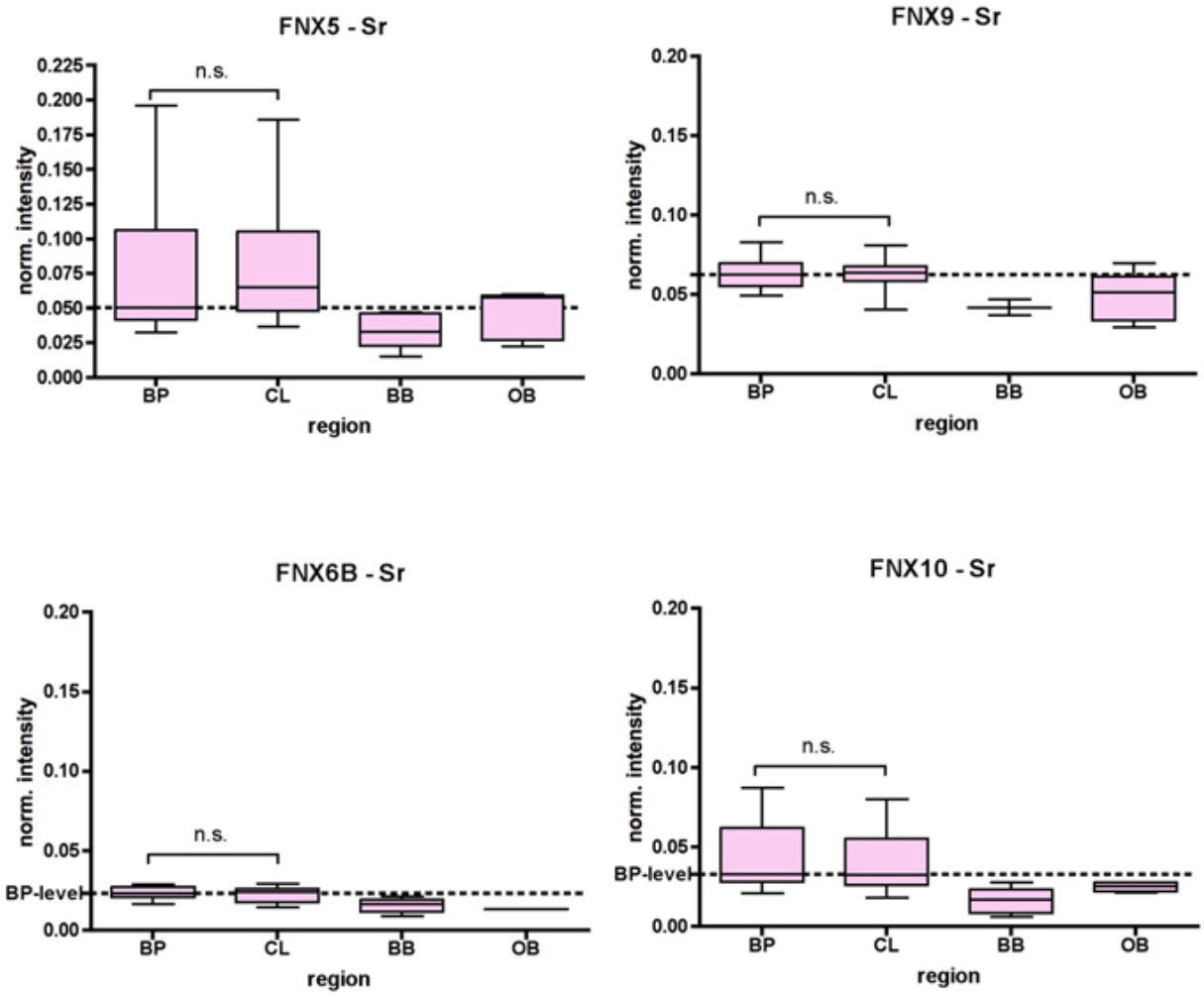

Figure 7.17: Normalized Sr intensities in bone packets (BP), cement lines (CL), bone borders (BB) and osteon borders (OB). The dashed line represents the bone level. The left column corresponds to samples with osteoporotic fractures. The age matched controls are on the right.

4. **Pb distribution in BPs**
   The Pb concentration in the BPs is plotted in Figure 7.18 and 7.19. A remarkable increase of Pb in BPs with high Ca content is present in the fractured and in the control samples. Surprisingly, the observed effect is not linear. While below about 23wt% Ca the Pb concentration is constantly low in nearly all maps, the Pb content increases with higher Ca values.
   Actually, the samples FNX1, FNX2, FNX5 and FNX10 (the samples with the highest intensities) show a rise, compareable to an exponential gain.

   Note that the Ca values in the following pictures are derived from the normalized fluorescence maps and not directly from the qBEI image.

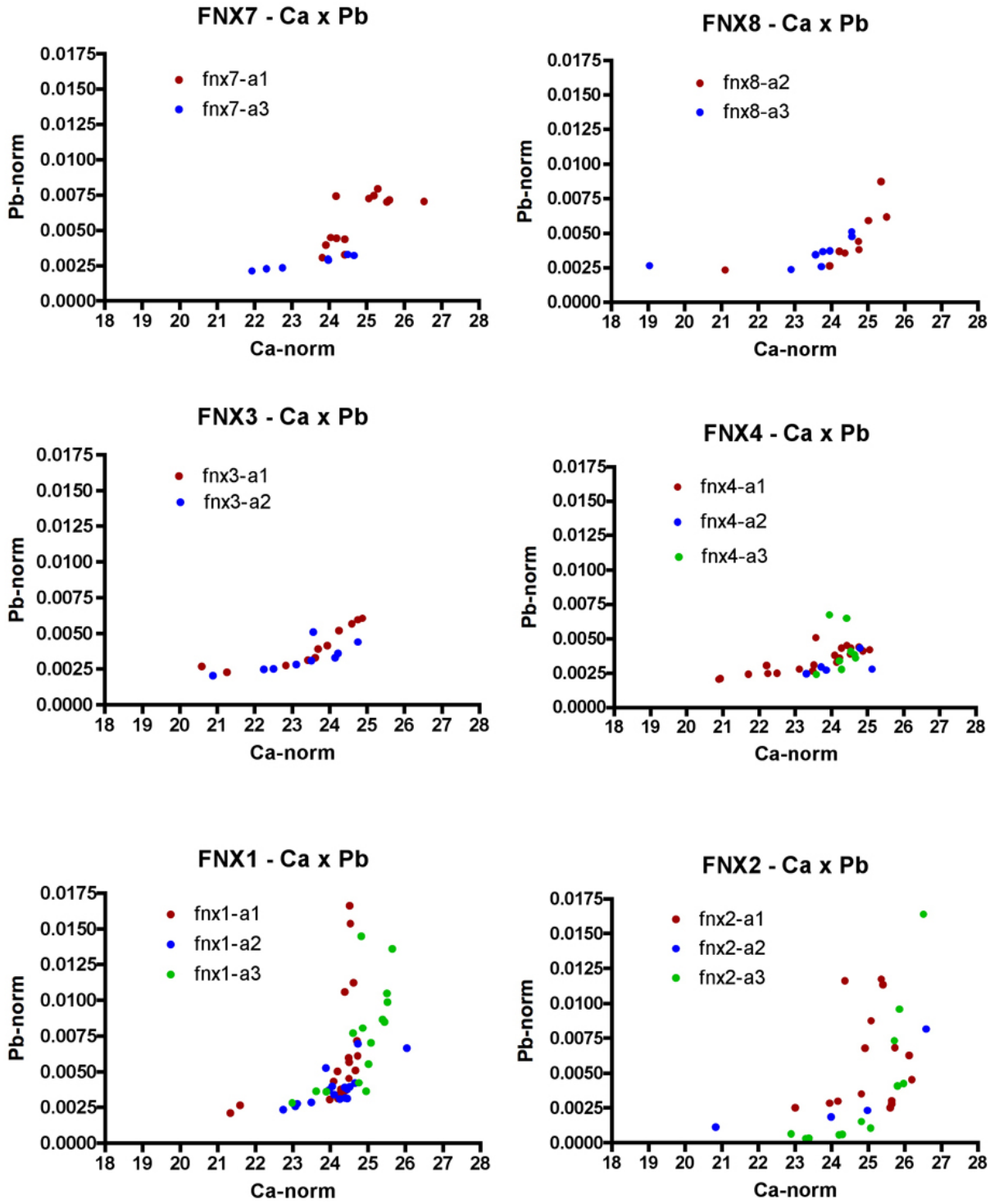

Figure 7.18: Pb versus Ca plots. The colors represent various maps of one sample. The left column corresponds to samples with osteoporotic fractures. The age matched controls are on the right.

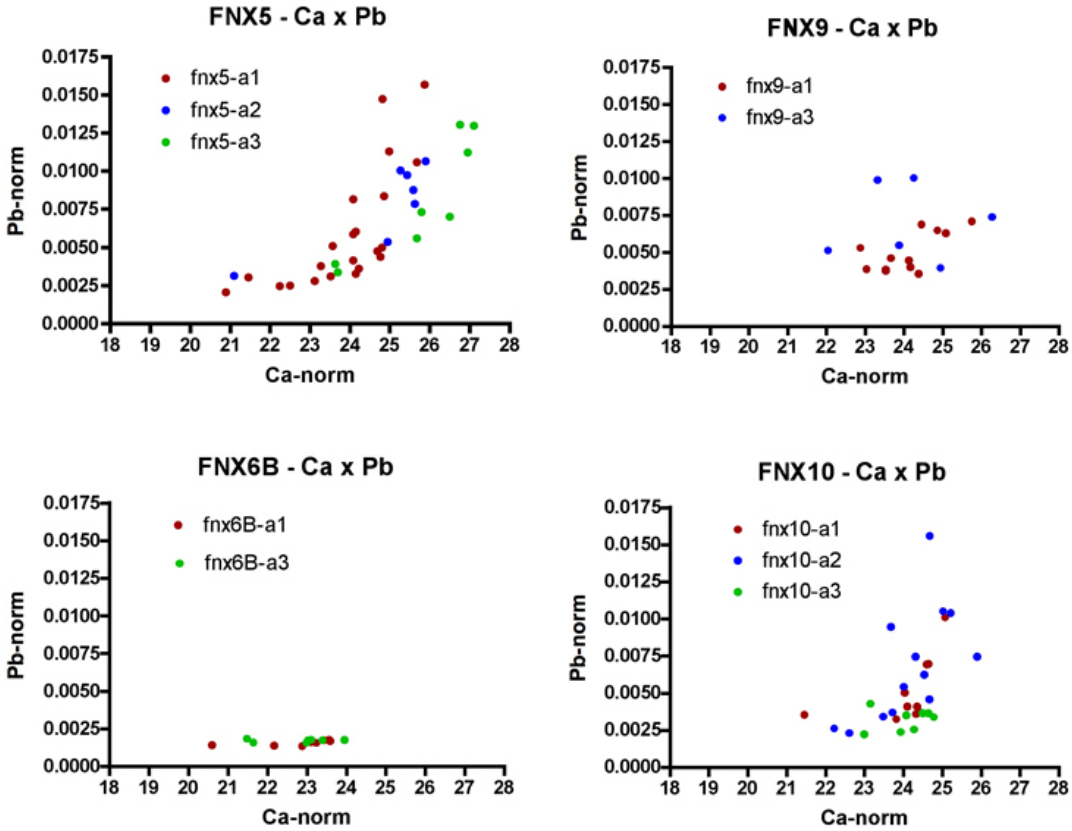

Figure 7.19: Pb versus Ca plots. The colors represent various maps of one sample. The left column corresponds to samples with osteoporotic fractures. The age matched controls are on the right.

The Pb - Ca-norm plots of the FNX6B and FNX9 show an altered distribution compared to the others. While in the FNX6B sample hardly any Pb was found, no correlation between the Pb content and the Ca concentration can be derived in the FNX9-diagram. A possible explanation for this behavior are the relatively poor normalization characteristics in these samples (Figure 6.9). Previously this figure was used to depict the quality of the normalization to the qBEI image, and beside the FNX6B specimen, the FNX9 sample shows high variations in the Ca-norm. vs. wt%Ca plot. This indicates inhomogenities below the surface. Therefore, this might cause the outlying behavior of the FNX9 sample.

5. **Sr distribution in BPs**
   The Sr distribution in the BPs is analyzed in the same way. Even if the increase of Sr in old bone packets is less distinct than in the Pb distribution, a comparable behavior is observed in most of the samples. Again, in the FNX9 a correlation of Sr and Ca-norm. is missing.The FNX6B samples contains only low amounts of Sr.
   Without giving statistical proof, it is remarkable that the amounts of Pb and Sr in the samples seem to correlate when comparing the 'Sr-norm vs. Ca-norm' plots with the 'Pb-norm vs. Ca-norm plots'. This might be an interesting aspect for further investigation.

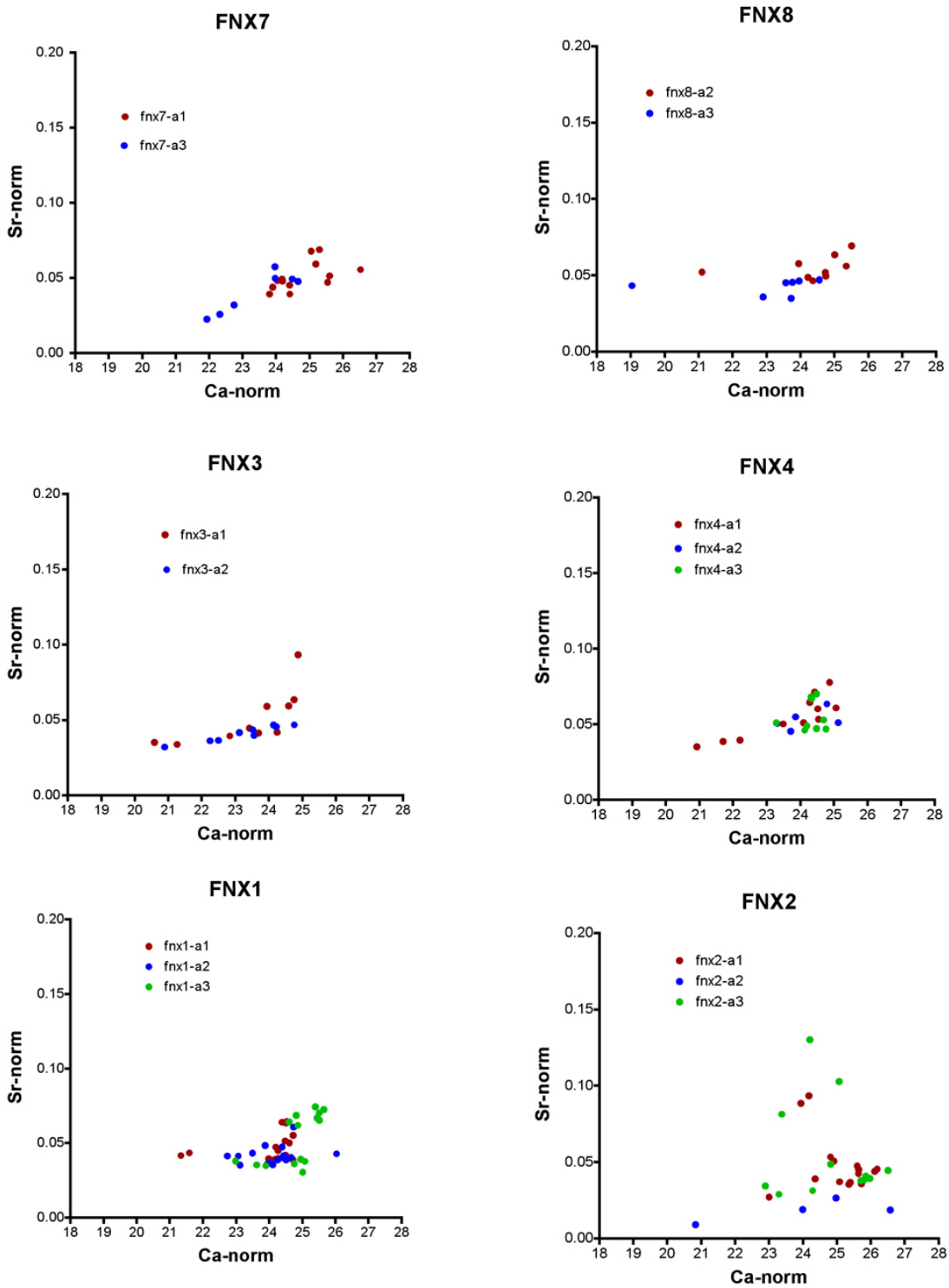

Figure 7.20: Sr versus Ca plots. The colors represent various maps of one sample. The left column corresponds to samples with osteoporotic fractures. The age matched controls are on the right.

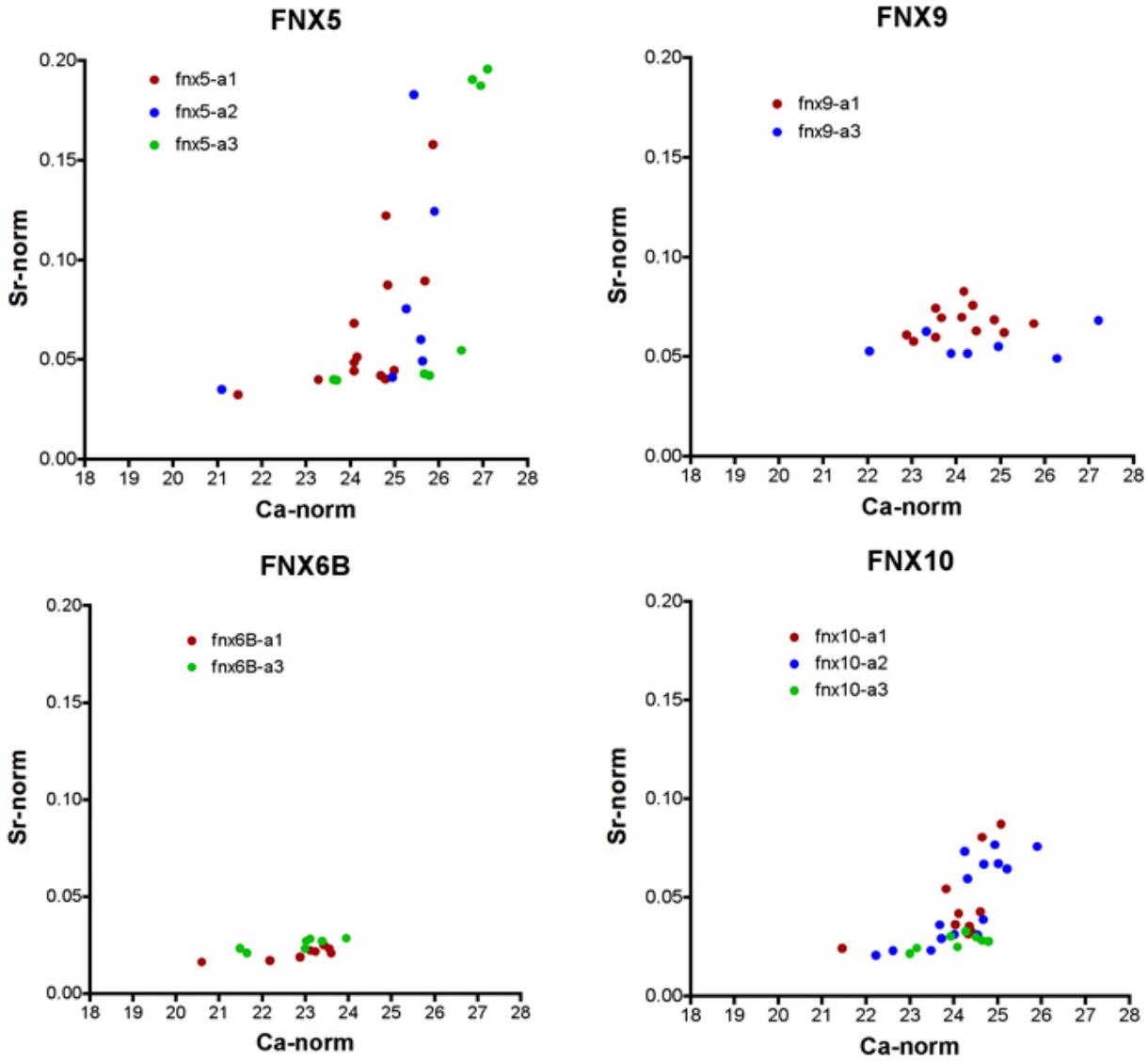

Figure 7.21: Sr versus Ca plots. The colors represent various maps of one sample. The left column corresponds to samples with osteoporotic fractures. The age matched controls are on the right.

6. **Zn distribution in BPs**
   While in the maps a positive correlation of Pb and Zn with Ca was assumed, no correlation between the Zn and the Ca content of the BPs is estimated. This behavior is in consistent with Figure 7.22 and 7.23.

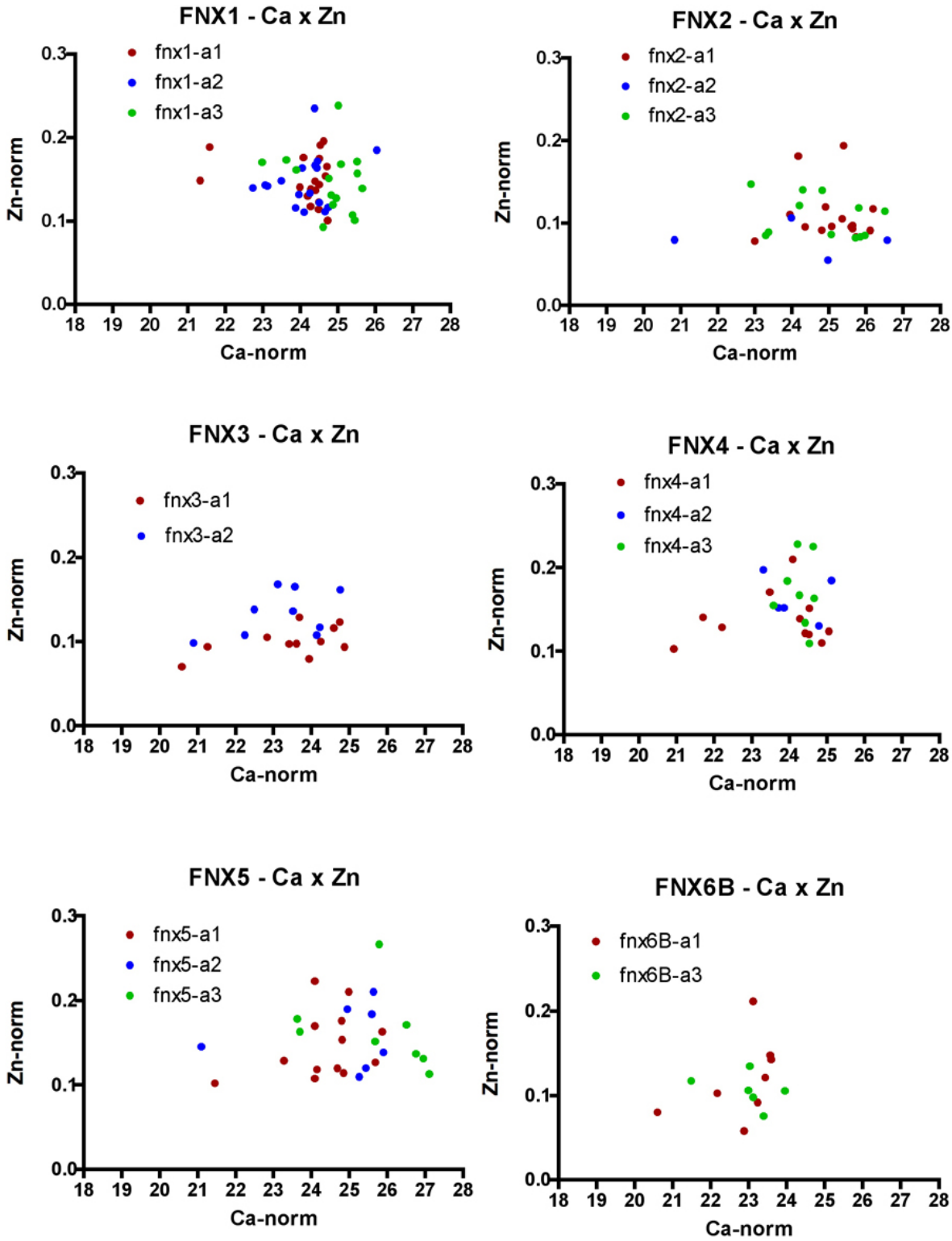

Figure 7.22: Zn versus Ca plots. The colors represent various maps of one sample. The left column corresponds to samples with osteoporotic fractures. The age matched controls are on the right.

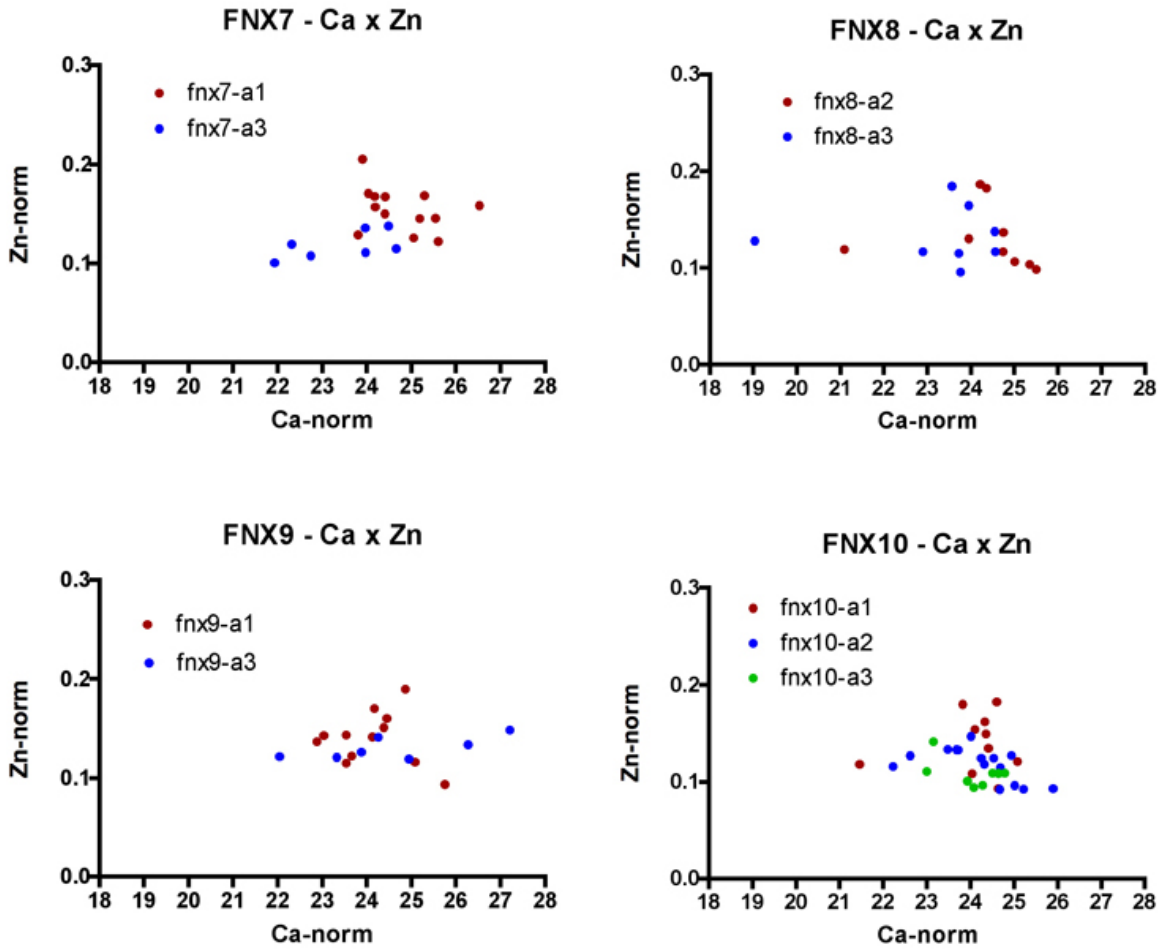

Figure 7.23: Zn versus Ca plots. The colors represent various maps of one sample. The left column corresponds to samples with osteoporotic fractures. The age matched controls are on the right.

Overall no correlation of Zn and Ca concentration is observed in the bone packets. No alterations in the trace element distribution between these two groups can be seen.

7.3 Zn distribution in an ostesarcoma

Since the tumor sample originates from a cisplatin-treated individual, the question appears if platinum (Pt) accumulates to detectable concentrations in the tumor tissue. According to 17.5 keV primary beam radiation, the Pt-L lines would be observed if the sample contained Pt. However, no Pt was found in the measured regions. Figure 7.24 shows a radiograph of the individual's knee and tibia. The sclerosing osteosarcoma appears bright due to X-ray absorption. In Figure 7.24 a qBEI image of the dissected tissue is shown. It contains a tumor-bone interface, where region of increased mineralization indicates the tumor tissue.

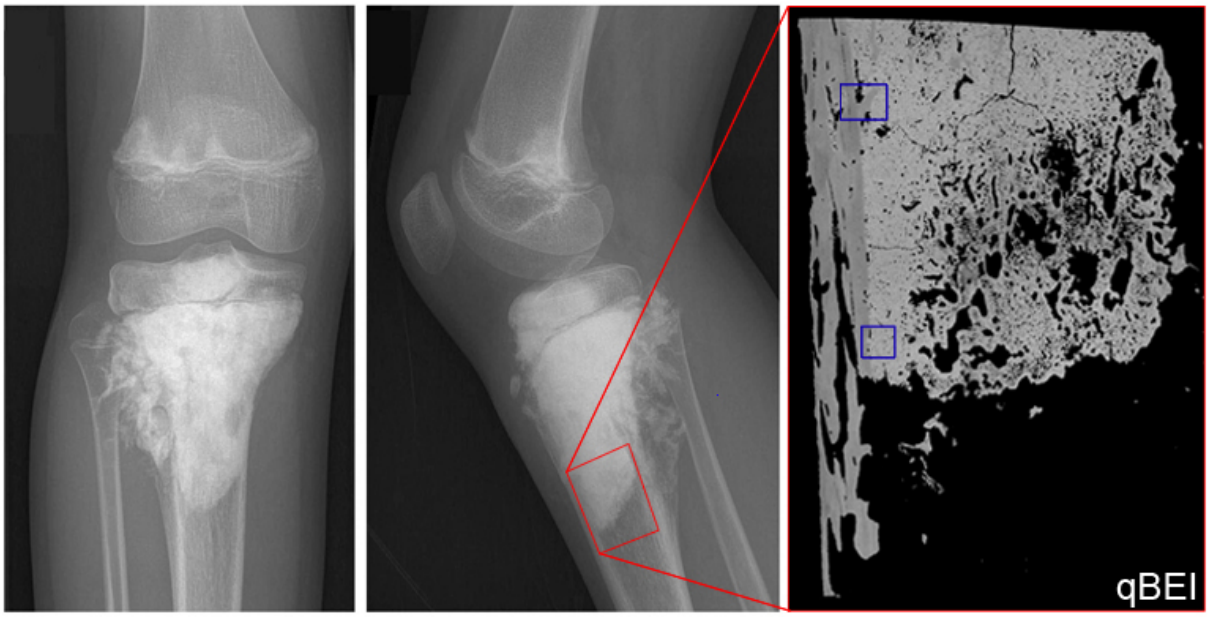

Figure 7.24: Radiographs of knee and tibia and a qBEI image of the dissected tumor tissue.

Surprisingly the Zn signal was raised in the cancer tissue. Two regions, containing tumor and health bone, were selected for fluorescence mapping. A highly raised Zn signal in the cancer tissue prooves Zn accumulation. Figure 7.25a and Figure 7.25b are linked with the blue bordered regions in Figure 7.24. Calculations lead to a 12.7 and a 13 fold Zn content in region (a) and (b) compared to the bone tissue.

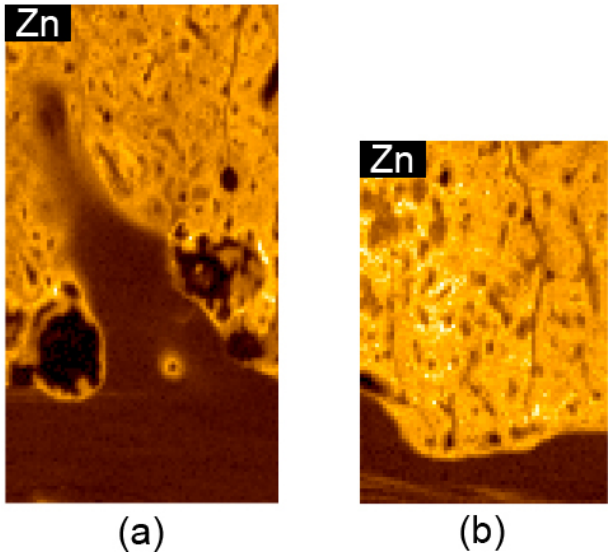

Figure 7.25: Zn maps of tumor bone interface color coded (‘fire‘ look up table); rotated by +90° relatively to the qBEI image in 7.24. The upper, bright matrix is tumor tissue while the bone contains less Zn.

Chapter 8

Discussion & Conclusion

Synchrotron radiation induced micro-XRF turns our as an excellent non-destructive method for spatially resolved multi-element analysis of calcified tissue. The confocal setup accounts for an interpretable signal when analyzing thick samples. Synchotron radiation provides a beneficial high proton flux (and therefore acceptable measurement times) as well as good background reduction. The spatial resolution of $10 \times 12 \times 19$ μm allows to distinguish between various histological structures, but thin interfaces like tidemarks (TM) and cement lines (CL) with a thickness in the range of 1 to 5 μm get blurred.
In combination with quantitative backscatter electron imaging (qBEI), either a direct or an indirect allocation of the regions of interest (ROI) is possible, although different depth resolution may cause some inconsistencies.

The trace element distribution in double tidemarks (DTM) and single tidemarks (STM) can be used to get a better understanding of the mineralization dynamics in cartilage. In regions with DTMs, the inner tidemark (iTM) and the outer tidemark (oTM) showed nearly equal amounts of Zn, therefore Zn can be seen as a marker for the TM with concentrations independently of the TM type.
In contrast, the differential Pb accumulation can be interpreted as a maturation process of the tidemark. A previous study showed that Pb has the ability to particularly substitute Ca in the calcium-hydroxyapatite crystal [61] and recent XANES measurements confirmed that Pb is bound as Pb-doped carbonated hydroxyapatite in the mineralized cartilage (mCAR) and in the TM [62]. Why Pb accumulation happens predominantly in the TMs, is still an open question. The data suggest that after the mineralization has stopped to advance into the region non mineralized cartilage (nmCAR), forming a TM (resting mineralization front), a continuous Pb accumulation starts to occur. In our model, Pb enhances in the iTM and the oTM, so the Pb content depends on the age (duration of accumulation) of the TM. Hence, regions with low Pb concentration variations between iTM and oTM represent a relatively small age difference of the TMs, while regions with distinctive differential Pb content indicate an old iTM relative to the oTM. This is in coherence with the previously reported advancement of the TM into the nmCAR as a response of microfracture in osteoarthritic individuals [44]. The evaluation of samples with single tidemarks (STM) shows trace elemental concentrations comparable to the iTM of DTM regions. This is in good agreement with our model for the DTM

dynamics.
Furthermore, this thesis confirms the findings of recent studies, which documented highly enhanced Pb and Zn concentrations in STMs [13].

The calcified tissue is known to contain about 95% of the total body burden of Pb[3]. Since the average Pb level in STM samples derives to a 19 fold of the bone level (ranging from a 7 fold to a 58 fold), the TM faces a potential internal Pb source. If osteoarthritis or other degenerative joint diseases cause a release of the TM-stored Pb, a remarkable increase of Pb in blood is thinkable. Due to the high concentration of Pb in the TMs even a clinical relevance cannot be excluded.
Additionally to the increased Pb level in the TMs, a significantly increased Pb concentration in the mCAR compared to the subchondral bine (scBONE) is documented.

The examination of 5 femoral neck samples from osteoporotic, postmenopausal women and 5 age matched controls showed no alterations in the Zn, Pb and Sr distributions and concentrations within these groups. According to the large number of risk factors for osteoporosis, this is not inconsistent with the previously reported loss of bone density because of Pb exposure [1] [2].
The enhanced Pb and concentrations in the CLs of nearly all samples could not be explained yet and needs further investigation. The intensities of Zn and Pb vary between the CLs within one measured map. Bright CLs in the qBEI image (usually CLs which separate two old bone packets), often also account for increased Zn and Pb levels. Since no classification of the CLs was performed no statistical proof can be given. Comparable fluctuations in the Zn concentration were observed at the borders to the bone marrow (BB) and osteon boders (OB).
Since, the regions of high Zn concentrations, the CLs and the TMs, are high in proteoglycan, this correlation might be an interesting point for further research.

The analysis of the trace elements Pb, Zn, and Sr in bone packets (BP) releaved remarkable results. In most samples the Pb and the Sr concentration correlates positively with the Ca concentration, while the amount of Zn in the BPs does not depend on the degree of calcification. Therefore, it is assumed that Zn is incorporated in the organic matrix, while Pb and Sr accumulate over years in bone mineral.
According to its position in the periodic table of elements, Sr^{2+} likely substitutes Ca^{2+} in the hydroxyapatite crystal [63]. It was confirmed previously, that while Sr-ranelate treatment Sr is incorporated in newly formed bone [64][65]. Furthermore, Meirer et al. prooved that Pb in bone is present in hydroxyapatite[66].
A simple incorporation of Pb into the Ca-apatite matrix, according to the apatite-crystal growth, would lead to a linear correlation in the Ca - Pb diagrams, but as apparent in Figure 7.18 and 7.19 it is not linear. Obviously, the Pb concentration is increased disproportionately high in old bone packets. A possible explanation would be a continuous substitution of Pb^{2+} for Ca^{2+} in the apatite crystal. While the Ca-concentration goes into saturation, Pb substitution still happens, resulting in an increase of the measured Pb/Ca ratios.
A comparison of the Figures 7.18, 7.19 and 7.20, 7.21 supports similar model for Sr accu-

mulation.
Beside these findings, surprisingly a correlation of Pb and Sr was observed. In general, samples with low Sr content also contain low amounts of Pb. Possible explanations might be a certain ratio of ingestion of Sr and Pb.
No differences in the elemental distribution between spongiosa and cortical bone were observed.

The examination of a sclerosing osteosarcoma after cisplatin treatment showed no Pt accumulation, but a drastically raised Zn content in the tumor tissue was detected. The role of Zn in cancer matrices has not been a focus of research yet. Although Zn accumulation was previously investigated in tumor tissue of a ductal carcinoma, also measured with microfocus at ANKA (KIT, Karlsruhe, Germany) using the FLUO beamline[67]. Up to now no osteosarcoma was analyzed with respect to the spatial Zn distribution by SR-micro-XRF. Since a sclerosing osteosarcoma is a quite unusual osteosarcoma type, the trace element analysis of further bone tumors is planed.

Limitations of these studies are first of all caused by the spatial resolution of SR-micro-XRF, which allows only a qualitative data assessment. TMs and CLs were identified from the qBEI image with a resolution about one order higher. Therefore the examination is constricted to ratios of intensities, either relative to various regions of a map or to different elemental intensities.
Furthermore, to resolve narrow interfaces like CLs, TMs, OBs, and BBs a distinctly higher resolution is necessary. Hence the exact localization of the investigated trace elements can only be estimated. The interesting question "Where do Zn and Pb accumulate? Directly at the tidemark, at the mCAR side or at the nmCAR side of the interface?" cannot be answered because of measurement restrictions. The Zn localization at the OBs and BBs would also require smaller beam spots for a detailed evaluation. For example the P06 beamline of the PETRA synchrotron in Hamburg, Germany offers highly brilliant radiation with a focal spot in the submicron range.

A principal imprecision appears when analyzing small structures like CLs with relatively rough resolution and therefore with relatively large voxels. In this case the CL only accounts for a small volume in the measured voxel, while the majority of the voxel is filled with the surrounding BP-matrix. As a result a doubled Zn intensity (compared to bone level) in the voxel or in a ROI corresponds to a concentration gain by a factor distinctly larger than 2.
An examination of bone and cartilage at so called nano-beamlines with focal spot diameters in the sub μm range would offer new possibilities and more precise measurements. High resolution absorption tomoraphy is performed at the SSRL (Stanford, USA) synchrotron with an full-field transmission X-ray microscopy (TXM). This technique might offers new possibilities for the examination of the trace ellement distribution in bone tissue and cartilage.

Bibliography

[1] Y. Sun, D. Sun, Z. Zhou, G. Zhu, H. Zhang, X. Chang, L. Lei, and T. Jin, "Osteoporosis in a chinese population due to occupational exposure to lead.," *American Journal of industrial Chemistry*, 2008.

[2] J. R. Campbell, R. N. Rosier, L. Novotny, and J. E. Puzas, "The association between environmental lead exposure and bone density in children," *Environ Health Perspect*, 2004.

[3] G. S. Berkowitz, J. M. Moline, and A. C. Todd, "Methodological issues related to studies of lead mobilization during menopause," *Salud Pública de México*, 1999.

[4] P. Wobrauschek, "Spezialverfahren der RFA." Lecture script for students, TU Vienna.

[5] the full wiki, "Electron transition in a hydrogen atom." online. http://www.thefullwiki.org/Humphreys_series - 23.01.2011.

[6] J. Aiginger and P. Wobrauschek, "Script of the lecture 'Strahlenphysik' at the TU Vienna." 2003.

[7] D. Attwood, *Soft X-Rays and Extreme Ultraviolet Radiation.* Cambridge: Cambridge University Press, 2000.

[8] Demtröder, *Experimentalphysik 3.* New York: Springer, 2nd edition ed., 2000.

[9] M. Mantler and P. Varga, "Physikalische Analytik." Lectrue script for students, TU Vienna.

[10] R. E. van Grieken and A. A. Markowicz, eds., *Handbook of X-Ray Spectrometry.* Practical spectroscopy series Volume 29, New York: Marcel Dekker Inc., 2nd edition revised and expanded ed., 2002.

[11] "Mass attenuation coefficients for lead." Figure by MIT OpenCourseWare. - http://www.flickr.com/photos/mitopencourseware/3706497749/#/ - 14.03.2011 online.

[12] J. I. Goldstein, D. E. Newbury, P. Echlin, D. C. Joy, A. D. Roming, C. E. Lyman, C.Fiori, and E. Lifshin, *Scanning Electron Microscopy and X-Ray Microanalysis.* New York: Plenum, 2nd edition ed., 1992.

[13] N. Zöger, *Micro X-ray Fluorescence Analysis and Micro-Tomography of Human Bone and Tissue.* PhD thesis, TU Vienna, 2005.

[14] B. Grossmayer, "Softwarepaket zur quantitativen röntgenfluorezenzanalyse mittels fundamentaler parameter unter verwendung von röntgenoptiken," Master's thesis, TU Vienna, 2009.

[15] B. Beckhoff, B. Kanngießer, L. Langhoff, R. Wedel, and H. Wolf, eds., *Practical X-Ray Fluorescence Analysis.* Berlin: Springer, 2006.

[16] A. dictionaries and encyclopedias, "The synchrotron." online. http://de.academic.ru/pictures/dewiki/115/schema_de_principe_du_-synchrotron.jpg online - 23.01.2011.

[17] K. Kim and D. Vaughan, "X-ray data booklet," 1986.

[18] K. W. Jones, "Synchrotron-radiation induced x-ray emission (srixe)," *Ultramicroscopy*, 1988.

[19] C. Streli, "Script of the lecture 'Strahlenphysik' at the Vienna UT." 2010.

[20] Moxtek, "X-ray transmission of polymer windows." online. http://www.moxtek.com/x-ray-windows/ap3-ultra-thin-polymer-windows.html - 23.01.2011.

[21] Unisantis, "Electron microscop image of a policapillary." online. http://www.unisantis.com/kumakhov-optics.html - 23.01.2011.

[22] J. Traupel, "Derivation of the bragg-equation." online. http://homepages.physik.uni-muenchen.de/ jana.traupel/Materie/FestkoerperOnline/Struktur/Abschnitt3.htm - 23.01.2011.

[23] P. Jeffrey, "Illustration of a multilayer crystal." online. http://xray0.princeton.edu/ phil/Facility/Guides/XrayDataCollection.html - 23.01.2011.

[24] "Schema of an electron microscope." Art. Encyclopaeia Britannica Online. ttp://www.britannica.com/EBchecked/topic-art/526571/110970/Scanning-electron-microscope-23.01.2011.

[25] P. Roschger, "Characterization of mineralized tissue in vertebrates by scanning microscopic methods for material science and medicine," 2003. Postdoctoral lecture qualification at the Montanuniversitaet Leoben.

[26] F. Arnal, P. Verdier, and P. Vinsensini, "Coefficient de rétrodiffusion dans de cas d'électrons monocinétiques arrivant sur la cible sous une incidence oblique," *Compt. rend. Acad. Sci. (Paris)*, 1969.

[27] G. Meeker, "Comparison of be image and se image of a du particle." online. http://pubs.usgs.gov/of/2001/ofr-01-0429/sem1/wtc01-36BeiSeiBi.gif - 23.01.2011.

[28] H. Seiler, "Secondary electron emission in the scanning electron microscope," *Journal of Applied Physics*, 1983.

[29] T. Koshikawa and R. Shimizu, "A monte carlo calculation of low-energy secondary electron emission from metals," *Journal of Physics D: Applied Physics*, 1974.

[30] T. Arnett, "Electron microscop image of trabecular bone." online. http://www.brsoc.org.uk/gallery/images/13lg.jpg - 23.01.2011.

[31] H. A. Kramers, "On the theory of x-ray absorption and of the continuous x-ray spectrum," *Philosophical Magazine*, 1923.

[32] "Electron track in a homogenous b-field." Addison Wesley Longmann Inc., online. http://ultracold.physics.sunysb.edu/Courses/PHY598-10.Fall/PHY598%20Fall2010%20-%20Santos.pdf - 23.01.2011.

[33] B. Jess, "Electron track in a homogenous b-field combined with an electric field." online. http://musr.physics.ubc.ca/ jess/hr/skept/E_M/img50.gif - 23.01.2011.

[34] J. Fidler, "Grundlagen der Elektronenmikroskopie." Lecture script for students, TU Vienna, 2005.

[35] D. Shotton, "Introduction to electron microscopy." Lectrue script for students, University of Oxford - 2001.

[36] R. P. Feynman, R. B. Leighton, and M. Sands, *The Feynman Lectures on Physics.* New York: Addison-Wesley, 1964.

[37] E. Chambost, "Everhart-thornley detector." online. http://commons.wikimedia.org/wiki/File:Everhart-Thornley_detector.JPG - 23.01.2011.

[38] P. Fratzl, H. S. Gupta, E. Paschalis, and P. Roschger, "Structure and mechanical quality of the collagen-mineral nano-composite in bone," *Journal of Materials Chemistry*, 2004.

[39] P. Roschger, P. Fratzl, J. Eschberger, and K. Klaushofer, "Validation of quantitative backscattered electron imaging for the measurement of mineral density distribution in human bone biopsies," *Bone*, 1998.

[40] D. Dempster, D. Felsenberg, and S. van der Geest, eds., *The Bone Quality Book.* Amsterdam: Elsevier, 2006.

[41] P. Roschger, "Slide from the lecture "Bone and connective tissue" at the Montanuniversität Leoben, austria." 2011.

[42] R. Rude, H. Gruber, and S. Oldham, "Cortisone-induced osteoporosis: effects on bone adenylate cyclase.," *Miner Electrolyte Metab.*, 1993.

[43] P. Roschger, H. Plenk Jr, K. Klaushofer, and J. Eschberger, "A new scanning electron microscopy approach to the quantification of bone mineral distribution: backscattered electron image grey-levels correlated to calcium K alpha-line intensities.," *Scanning microscopy*, 1995.

[44] H.Madry, C. Dijk, and M. Mueller-Gerbl, "The basic science of subchondral bone," *Knee Surg. Sports Traumatol. Arthrosc.*, 2010.

[45] P. A. Revell, C. Pirie, G. Amir, S. Rashad, and F. Walker, "Metabolic activity in the calcified zone of cartilage: Observations on tetracycline labelled articular cartilage in human osteoarthritic hips," *Rheumatology International*, 1990.

[46] L. Lane and P. Bullough, "Age-related changes in the thickness of the calcified zone and the number of tidemarks in adult human articular cartilage," *Journal of Bone and Joint Surgery*, 1980.

[47] R. O. Becker, J. A. Spadaro, and E. W. Berg, "The trace elements of human bone," *Journal of Bone and Joint Surgery*, 2011.

[48] H. Koch Jr, E. Smith, N. Shimp, and J. Connor, "Analysis of trace elements in human tissues. I. Normal tissues," *Cancer*, 1956.

[49] "Toxological profile for lead," 2007. U.S. department of health and human services.

[50] A. Itoa, H. Kawamurab, M. Otsukac, M. Ikeuchia, H. Ohgushia, K. Ishikawad, K. Onumaa, N. Kanzakia, Y. Sogoa, and N. Ichinosee, "Zinc-releasing calcium phosphate for stimulating bone formation," *Materials Science and Engineering*, 2002.

[51] H. J. Seo, Y. E. Cho, T. Kim, H. I. Shin, and I. S. Kwun, "Zinc may increase bone formation through stimulating cell proliferation, alkaline phosphatase activity and collagen synthesis in osteoblastic MC3T3-E1 cells," *Materials Science and Engineering*, 2010.

[52] P. J. Meunier, C. Roux, S. O. Ego Seeman, J. E. Badurski, T. D. Spector, J. Cannata, A. Balogh, E. M. Lemmel, S. Pors-Nielsen, R. Rizzoli, H. K, Genant, and J. Y. Reginster, "The effects of strontium ranelate on the risk of vertebral fracture in women with postmenopausal osteoporosis," *The new england journal of medicine*, 2004.

[53] N. Zöger, P. Wobrauschek, C. S. G. Pepponi, P. Roschger, G. Falkenberg, and W. Osterode, "Distribution of pb and zn in slices of human bone by synchrotron micro-xrf," *X-ray spectrometry*, 2005.

[54] N. Fratzl-Zelman, P. Roschger, A. Gourrier, M. Weber, B. Misof, N. Loveridge, J. Reeve, K. Klaushofer, and P. Fratzl, "Combination of Nanoindentation and Quantitative Backscattered Electron Imaging Revealed Altered Bone Material Properties Associated with Femoral Neck Fragility," *Calcified tissue international*, 2009.

[55] "Illustration of a femur - Copyright by Novartis," 2008. http://theinnerdoor.files.wordpress.com/2008/03/femur_anterior.png?w=500- 5.2.2011.

[56] N. Zöger, P. Wobrauschek, C. Streli, G. Pepponi, P. Roschger, G. Falkenberg, and W. Osterode, "Distribution of Pb and Zn in slices of human bone by synchrotron μ-XRF," *X-Ray Spectrometry*, 2005.

[57] G. Falkenberg, O. Clauss, and T. Tschentscher, "Hasylab annual report," 2001.

[58] R. Simon, G. Buth, and M. Hagelstein, "The X-ray-fluorescence facility at ANKA, Karlsruhe: Minimum detection limits and micro probe capabilities," *Nuclear Instruments and Methods in Physics Research Section B: Beam Interactions with Materials and Atoms*, 2003.

[59] "Characteristics of the FLUO beamline." KIT - Karlsrhue Institute of Technology, ANKA Website - http://ankaweb.fzk.de/website.php?page=instrumentation_beam&id=3 - 7.02.2011 online.

[60] P. Roschger, E. P. Paschalis, P. Fratzl, and K. Klaushofer, "Bone mineralization density distribution in health and disease," *Bone*, 2004.

[61] D. Ellis, J. Terra, O. Warschkow, M. Jiang, G. González, J. Okasinski, M. Bedzyk, A. Rossi, and J. Eon, "A theoretical and experimental study of lead substitution in calcium hydroxyapatite," *Physical Chemistry Chemical Physics*, 2006.

[62] F. Meirer, B. Pemmer, G. Pepponi, N. Zöger, P. Wobrauschek, S. Sprio, A. Tampieri, J. Göttlicher, R. Steininger, S. Mangold, *et al.*, "Assessment of chemical species of lead accumulated in tidemarks of human articular cartilage by X-ray absorption near-edge structure analysis," *Journal of Synchrotron Radiation*, 2011.

[63] J. Christoffersen, M. Christoffersen, N. Kolthoff, and O. Bärenholdt, "Effects of strontium ions on growth and dissolution of hydroxyapatite and on bone mineral detection," *Bone*, 1997.

[64] P. Roschger, I. Manjubala, N. Zoeger, F. Meirer, R. Simon, C. Li, N. Fratzl-Zelman, B. Misof, E. Paschalis, C. Streli, *et al.*, "Bone material quality in transiliac bone biopsies of postmenopausal osteoporotic women after 3 years of strontium ranelate treatment," *Journal of Bone and Mineral Research*, 2010.

[65] C. Li, O. Paris, S. Siegel, P. Roschger, E. Paschalis, K. Klaushofer, and P. Fratzl, "Strontium is incorporated into mineral crystals only in newly formed bone during strontium ranelate treatment," *Journal of Bone and Mineral Research*, 2010.

[66] F. Meirer, B. Pemmer, G. Pepponi, N. Zoeger, P. Wobrauschek, S. Sprio, A. Tampieri, J. Goettlicher, R. Steininger, S. Mangold, *et al.*, "Assessment of chemical species of lead accumulated in tidemarks of human articular cartilage by X-ray absorption near-edge structure analysis," *Journal of Synchrotron Radiation*, 2011.

[67] M. Farquharson, A. Al-Ebraheem, K. Geraki, R. Leek, A. Jubb, and A. Harris, "Zinc presence in invasive ductal carcinoma of the breast and its correlation with oestrogen receptor status," *Physics in Medicine and Biology*, 2009.